PREPRINT OF MANUSCRIPT ACCEPTED AT ELEMENTA: SCIENCE OF THE ANTHROPOCENE "The MOSAiC Distributed Network: observing the coupled Arctic system with multidisciplinary, coordinated platforms"

Benjamin Rabe[1], Christopher J Cox[1,2,3,4,5,6,7,8,9,10,11,12,13,14,15], Ying-Chih Fang[16,17], Helge Goessling[1], Mats A Granskog[18], Mario Hoppmann[18], Jennifer K Hutchings[18], Thomas Krumpen[18], Ivan Kuznetsov[18], Ruibo Lei[18], Tao Li[18], Wieslaw Maslowski[18], Marcel Nicolaus[18], Don Perovich[18], Ola Persson[18], Julia Regnery[18], Ignatius Rigor[18], Matthew D Shupe[18], Vladimir Sokolov[18], Gunnar Spreen[18], Tim Stanton[18], Daniel M Watkins[18], Ed Blockley[18], H Jakob Buenger[18], Sylvia Cole[18], Allison Fong[18], Jari Haapala[18], Céline Heuzé[18], Clara J M Hoppe[18], Markus Janout[18], Arttu Jutila[18], Christian Katlein[18], Richard Krishfield[18], Long Lin[18], Valentin Ludwig[18], Anne Morgenstern[18], Jeff O'brien[18], Alejandra Quintanilla Zurita[18], Thomas Rackow[18], Kathrin Riemann-Campe[18], Jan Rohde[18], William Shaw[18], Vasily Smolyanitsky[18], Amy Solomon[18], Anneke Sperling[18], Ran Tao[18], John Toole[18], Michel Tsamados[18], Jialiang Zhu[18], and Guangyu Zuo[18]

[1]Alfred-Wegener-Institut Helmholtz Zentrum für Polar-und Meeresforschung
[2]NOAA Physical Sciences Laboratory (PSL)
[3]Norwegian Polar Institute, Fram Centre
[4]Oregon State University
[5]College of Oceanic and Atmospheric Sciences, Polar Research Institute of China
[6]Ocean University of China
[7]Alfred-Wegener-Institut Helmholtz Zentrum für Polar-und Meeresforschung, National Laboratory for Marine Science and Technology
[8]Thayer School of Engineering, Dartmouth College
[9]Physical Sciences Laboratory, Cooperative Institute for Research in Environmental Sciences, University of Colorado, National Oceanic and Atmospheric Administration
[10]University of Washington
[11]Arctic and Antarctic Research Institute
[12]Institute of Environmental Physics, University of Bremen
[13]Naval Postgraduate School and Moss Landing Marine Laboratories
[14]Brown University
[15]Met Office Hadley Centre, Oregon State University
[16]Department of Oceanography, College of Marine Sciences, Alfred-Wegener-Institut Helmholtz Zentrum für Polar-und Meeresforschung
[17]National Sun Yat-sen University
[18]Affiliation not available

March 14, 2024

PREPRINT of manuscript accepted by
Elementa Science of the Anthropocene, Feb 19, 2023.

The final publication will appear at
https://online.ucpress.edu/elementa .

The MOSAiC Distributed Network: observing the coupled Arctic system with multidisciplinary, coordinated platforms

Benjamin Rabe[1*], Christopher J. Cox[2], Ying-Chih Fang[3], Helge Goessling[4], Mats A. Granskog[5], Mario Hoppmann[6], Jennifer K Hutchings[7], Thomas Krumpen[8], Ivan Kuznetsov[9], Ruibo Lei[10], Tao Li[11], Wieslaw Maslowski[12], Marcel Nicolaus[13], Don Perovich[14], Ola Persson[15], Julia Regnery[16], Ignatius Rigor[17], Matthew D. Shupe[18*], Vladimir Sokolov[19], Gunnar Spreen[20], Tim Stanton[21], Daniel M. Watkins[22], Ed Blockley[23], H. Jakob Buenger[24], Sylvia Cole[25], Allison Fong[26], Jari Haapala[27], Céline Heuzé[28], Clara J.M. Hoppe[29], Markus Janout[30], Arttu Jutila[31], Christian Katlein[32], Richard Krishfield[33], Long Lin[34], Valentin Ludwig[35], Anne Morgenstern[36], Jeff O'Brien[37], Alejandra Quintanilla Zurita[38], Thomas Rackow[39], Kathrin Riemann-Campe[40], Jan Rohde[41], William Shaw[42], Vasily Smolyanitsky[43], Amy Solomon[44], Anneke Sperling[45], Ran Tao[46], John Toole[47], Michel Tsamados[48], Jialiang Zhu[49], Guangyu Zuo[50]

[1] Alfred-Wegener-Institut Helmholtz Zentrum für Polar-und Meeresforschung, Bremerhaven, Germany

[2] NOAA Physical Sciences Laboratory (PSL), Boulder, USA

[3] Alfred-Wegener-Institut Helmholtz Zentrum für Polar-und Meeresforschung, Bremerhaven, Germany; Department of Oceanography, College of Marine Sciences, National Sun Yat-sen University, Kaohsiung, Taiwan

[4] Alfred-Wegener-Institut Helmholtz Zentrum für Polar-und Meeresforschung, Bremerhaven, Germany

[5] Norwegian Polar Institute, Fram Centre, Tromsø, Norway
[6] Alfred-Wegener-Institut Helmholtz Zentrum für Polar-und Meeresforschung, Bremerhaven, Germany
[7] Oregon State University, Corvallis, Oregon, USA
[8] Alfred-Wegener-Institut Helmholtz Zentrum für Polar-und Meeresforschung, Bremerhaven, Germany
[9] Alfred-Wegener-Institut Helmholtz Zentrum für Polar-und Meeresforschung, Bremerhaven, Germany
[10] Polar Research Institute of China, China
[11] College of Oceanic and Atmospheric Sciences, Ocean University of China, Qingdao, China; Pilot National Laboratory for Marine Science and Technology, Qingdao, China
[12] Alfred-Wegener-Institut Helmholtz Zentrum für Polar-und Meeresforschung, Bremerhaven, Germany
[13] Alfred-Wegener-Institut Helmholtz Zentrum für Polar-und Meeresforschung, Bremerhaven, Germany
[14] Thayer School of Engineering, Dartmouth College, Dartmouth, USA
[15] Cooperative Institute for Research in Environmental Sciences, University of Colorado; Physical Sciences Laboratory, National Oceanic and Atmospheric Administration, Boulder, USA
[16] Alfred-Wegener-Institut Helmholtz Zentrum für Polar-und Meeresforschung, Bremerhaven, Germany
[17] University of Washington, Seattle, USA
[18] Cooperative Institute for Research in Environmental Sciences, University of Colorado; Physical Sciences Laboratory, National Oceanic and Atmospheric Administration, Boulder, USA
[19] Arctic and Antarctic Research Institute, St. Petersburg, Russia
[20] University of Bremen, Institute of Environmental Physics, Bremen, Germany
[21] Naval Postgraduate School and Moss Landing Marine Laboratories, Monterey, USA
[22] Brown University, Providence, RI, USA; Oregon State University, Corvallis, OR, USA
[23] Met Office Hadley Centre, FitzRoy Road, Exeter, UK

[24]Alfred-Wegener-Institut Helmholtz Zentrum für Polar-und Meeresforschung, Bremerhaven, Germany
[25]Woods Hole Oceanographic Institution, Woods Hole, USA
[26]Alfred-Wegener-Institut Helmholtz Zentrum für Polar-und Meeresforschung, Bremerhaven, Germany
[27]Finnish Meteorological Institute, Helsinki, Finland
[28]Department of Earth Sciences, University of Gothenburg, Gothenburg, Sweden
[29]Alfred-Wegener-Institut Helmholtz Zentrum für Polar-und Meeresforschung, Bremerhaven, Germany
[30]Alfred-Wegener-Institut Helmholtz Zentrum für Polar-und Meeresforschung, Bremerhaven, Germany
[31]Alfred-Wegener-Institut Helmholtz Zentrum für Polar-und Meeresforschung, Bremerhaven, Germany; Finnish Meteorological Institute, Helsinki, Finland
[32]Alfred-Wegener-Institut Helmholtz Zentrum für Polar-und Meeresforschung, Bremerhaven, Germany
[33]Woods Hole Oceanographic Institution, Woods Hole, USA
[34]Polar Research Institute of China, China
[35]Alfred-Wegener-Institut Helmholtz Zentrum für Polar-und Meeresforschung, Bremerhaven, Germany
[36]Alfred-Wegener-Institut Helmholtz Zentrum für Polar-und Meeresforschung, Bremerhaven, Germany
[37]Woods Hole Oceanographic Institution, Woods Hole, USA
[38]Alfred-Wegener-Institut Helmholtz Zentrum für Polar-und Meeresforschung, Bremerhaven, Germany
[39]European Centre for Medium-Range Weather Forecasts (ECMWF), Bonn, Germany
[40]Alfred-Wegener-Institut Helmholtz Zentrum für Polar-und Meeresforschung, Bremerhaven, Germany
[41]Alfred-Wegener-Institut Helmholtz Zentrum für Polar-und Meeresforschung, Bremerhaven, Germany
[42]Naval Postgraduate School and Moss Landing Marine Laboratories, Monterrey, USA
[43]Arctic and Antarctic Research Institute, St. Petersburg, Russia

[44]Cooperative Institute for Research in Environmental Sciences, University of Colorado; Physical Sciences Laboratory, National Oceanic and Atmospheric Administration; Boulder, USA
[45]Alfred-Wegener-Institut Helmholtz Zentrum für Polar-und Meeresforschung, Bremerhaven, Germany
[46]Alfred-Wegener-Institut Helmholtz Zentrum für Polar-und Meeresforschung, Bremerhaven, Germany
[47]Woods Hole Oceanographic Institution, Woods Hole, USA, Woods Hole, USA
[48]Centre for Polar Observation and Modelling, Earth Sciences, UCL, London, UK
[49]College of Oceanic and Atmospheric Sciences, Ocean University of China
[50]College of Electrical and Power Engineering, Taiyuan University of Technology, Taiwan

*corresponding authors: benjamin.rabe@awi.de, matthew.shupe@noaa.gov

Abstract

Central Arctic properties and processes are important to the regional and global coupled climate system. The Multidisciplinary drifting Observatory for the Study of Arctic Climate (MOSAiC) Distributed Network (DN) of autonomous ice-tethered systems aimed to bridge gaps in our understanding of temporal and spatial scales, in particular with respect to the resolution of Earth system models. By characterizing variability around local measurements made at a Central Observatory the DN covers both the coupled system interactions involving the ocean-ice-atmosphere interfaces as well as three-dimensional processes in the ocean, sea ice, and atmosphere. The more than 200 autonomous instruments ("buoys") were of varying complexity and set up at different sites mostly within 50 km of the Central Observatory. During an exemplary midwinter month, the DN observations captured the spatial variability of atmospheric processes on sub-monthly time scales, but less so for monthly means. They show significant variability in snow depth and ice thickness, and provide a temporally and spatially resolved characterization of ice motion and deformation, showing coherency at the DN scale but less at smaller spatial scales. Ocean data show the background gradient across the DN as well as spatially dependent time variability due to local mixed layer sub-mesoscale and mesoscale processes, influenced by a variable ice cover. The second case (May–June 2020) illustrates the utility of the DN during the absence of manually obtained data by providing continuity of physical and biological observations during this key transitional period. We show examples of synergies between the extensive MOSAiC remote sensing observations and numerical modelling, such as estimating the skill of ice drift forecasts and evaluating coupled system modelling. The MOSAiC DN has been proven to enable analysis of local to mesoscale processes in the coupled atmosphere-ice-ocean system and has the potential to improve model parameterizations of important, unresolved processes in the future.

1. INTRODUCTION

a. Arctic processes, global climate models and MOSAiC

The Arctic is a region of prime importance for ongoing global change, showing significant sea ice retreat (Lindsay and Schweiger, 2015; Meredith et al., 2019; Intergovernmental Panel on Climate change, 2022), near-surface air temperature rising at more than twice the global rate (e.g., Rantanen et al., 2022), and "Atlantification" in the Eurasian part of the Arctic Ocean (e.g., Polyakov et al., 2017; Ingvaldsen et al., 2021). The largely enclosed nature of the basin and the extensive continental shelves make the Arctic Ocean much smaller in both area and volume than the Indian, Atlantic and Pacific oceans, yet it receives on the order of 10% of the world's continental runoff (Haine et al., 2015; GRDC, 2023). Moreover, the Arctic Ocean is closely linked to the adjacent oceans and seas, where it can have potentially profound impact on regional or global ocean circulation (e.g., Häkkinen, 1999; Haak et al., 2003) and atmospheric temperatures (e.g., Wu et al., 2013) at lower latitudes, and, ultimately, global climate (e.g., Koenigk et al., 2007; Rennermalm et al., 2007).

Basin-wide budgets and circulation patterns are determined not only by basin-scale forcing but also by many processes that play out from mesoscales (von Appen et al., 2022, and references therein) to small-scale turbulence (Rippeth and Fine, 2022, and references therein) and further to the (diffusive) molecular scale (Rudels et al., 2009; Shibley et al., 2017). The regionally varying seasonal and perennial sea ice cover and surface snow add challenges to understanding the regional coupled climate system. Feedbacks among the atmosphere, sea ice and snow, and liquid ocean are complex, varying in all three dimensions and in time. The vertical column is particularly important, as it allows radiation and turbulence to directly transport energy, mass, and other constituents across different layers in the coupled system (e.g., Sirevaag et al., 2011; Tjernström et al., 2014). Lateral processes, including long-range atmospheric transport, sea ice melt and freeze, as well as frontal dynamical processes and eddies in the ocean and atmosphere, boundary layer turbulence, and cloud macrophysical and microphysical properties (e.g., Timmermans et al., 2012; Jonassen et al., 2020; George et al., 2021), lead not only to lateral but also to vertical fluxes. This combination of lateral and vertical fluxes has been shown to strongly link atmosphere-ice-ocean features such as cloud liquid water content and ice growth rates at the ice-ocean interface (Persson et al., 2017). Both local small-scale processes as well as mesoscale features are highly heterogeneous in space and time, across the disciplines of physics, chemistry and biology (e.g., d'Ovidio, 2010; Levy and Martin, 2013; Mahadevan, 2016). Hence, how well any single point in space and time may represent the conditions across a larger domain, such as an ocean basin or a climate model grid box, is not clear. Even a time series at one point in space or a quasi-synoptic survey along a single line may not capture all of the important variability. A spatial network of sensors measuring key variables at high temporal resolution is needed.

The Multidisciplinary drifting Observatory for the Study of Arctic Climate (MOSAiC) set out to measure a multitude of variables at a variety of spatial scales in the coupled atmosphere-ice-ocean system along the transpolar drift throughout a whole annual cycle, with the ultimate aim to enhance our understanding of regional and local processes and improve coupled climate modeling. From October 2019 to July 2020 the German icebreaker RV *Polarstern* (Alfred-Wegener-Institut Helmholtz-Zentrum für Polar- und Meeresforschung, 2017) served as the base of operations and was moored to an ice floe, drifting across the Eurasian basin from north of the Laptev Sea to Fram Strait. The vessel was then relocated to a different ice floe in the central Arctic during the final phase of the experiment in August and September 2020, capturing the autumn freeze-up. The Central Observatory of the experiment consisted of many fixed installations on RV *Polarstern* itself, as well as a wide array of sampling and measurement activities on the main ice floe within about 2 km of the vessel. Further details on the disciplinary work can be found in overviews by the scientific teams, covering the atmosphere (Shupe et al., 2022), physical oceanography (Rabe et al., 2022), sea ice and snow (Nicolaus et al., 2022), the ecosystem (Fong et al., n.d.), and biogeochemistry (overview publication expected in this special feature, led by E Damm). These works also contain details on the scientific conceptual design, logistics and legs of the expedition that we do not detail here.

b. Gaps in knowledge and community needs

Despite numerous efforts to observe and model the Arctic coupled atmosphere-ice-ocean system there are significant gaps in our knowledge of the relevant processes (Meredith et al., 2019). Prior to MOSAiC, much observational data was lacking for the atmosphere (Bourassa et al., 2013; Shupe et al., 2022), the sea ice and snow (Nicolaus et al., 2022), and the ocean (Rabe et al., 2022; Weingartner et al., 2022). The horizontal grid resolution in current global climate or Earth system models used for multi-decadal simulations ranges from 8–250 km, typically 8–100 km in the ocean and coarser in the atmosphere, 25–250 km (Haarsma et al., 2016; Roberts et al., 2019). Numerical Weather Prediction and regional climate and ocean-ice models reach resolutions with a spacing of less than 10 km (Rackow et al., 2019), with some approaching 1 km, in both the atmosphere (Wedi et al., 2020), the sea ice and the ocean (Wang et al., 2020). Increasingly, such models are resolving variability at scales that are finer than the typical grid boxes of multi-decadal global climate model simulations outlined above, and hence require process-level observations at fine scales. Key variabilities include mesoscale ocean eddies (e.g., Wang et al., 2020) on scales of around 5–10 km (e.g., Nurser and Bacon, 2014; Sein et al., 2017); sea ice thickness, deformation, and roughness (e.g., Bouchat et al., 2022; Hutter et al., 2022a); snow depth, mesoscale variability of cloud structure and associated dynamics, and mesoscale wind variations; and variability of surface energy and momentum fluxes. These fluxes are dependent on the variability of clouds and snow/ice surface characteristics. An improved representation of these, often multidisciplinary, processes, either through increased model resolution or advanced parameterizations, is critical for reducing uncertainty in models and their predictions of Arctic climate change (Maslowski et al., 2012; Jin et al., 2018; Roberts et al., 2019; Clement Kinney et al., 2022; Jung et al., 2022; Heuzé et al., 2023).

Autonomous observations have gained importance in the Arctic Ocean in recent decades and bring the potential to fill many of the observational needs. The development of technologically advanced ice-tethered systems, capable of measuring and sending data while drifting with sea ice, has closed significant gaps in seasonal and regional observing. Examples of these kinds of instrument systems are the JAMSTEC Compact Arctic Drifter (J-CAD; Hatakeyama et al., 2001), Metocean Polar Ocean Profiling System (POPS; Kikuchi et al., 2007), Woods Hole Oceanographic Institution Ice-tethered Profiler (WHOI-ITP; Toole et al., 2011; Krishfield et al., 2008), Naval Postgraduate School Autonomous Ocean Flux Buoys (AOFB; Stanton et al., 2012), Ice-Atmosphere Arctic Ocean platforms (IAOOS; Koenig et al., 2016; Athanase et al., 2019), several kinds of sea ice mass balance buoys (Richter-Menge et al., 2006; Jackson et al., 2013; Planck et al., 2019; Lei et al., 2022a), and snow buoys (hereafter "Snow Buoys"; Nicolaus et al., 2021a). An overarching coordinating effort, the International Arctic Buoy Programme (IABP; Rigor et al., 2002; IABP, 2023; Ermold and Rigor, 2023), has been supporting the basin-wide deployment of autonomous ice-tethered instruments across the whole Arctic Ocean region, which also includes regionally focused efforts.

c. The MOSAiC Distributed Network (DN)

One of the unique ideas laid out in the MOSAiC Science and Implementation plans (MOSAiC Consortium, 2016; 2018) was to observe a drifting 'unit' of sea ice, approximately the size of a typical model grid box, to quantify the "sub-grid scale" variability and the representativeness of individual measurements throughout the atmosphere-ice-ocean column. This concept specifically motivated the design of the MOSAiC DN, where numerous autonomous measurement systems were installed within a radius of a few tens of kilometers of RV *Polarstern* to obtain continuous observations of key variables that were also observed at the Central Observatory (Shupe et al., 2022; Nicolaus et al., 2022; Rabe et al., 2022). This DN has enabled observations to:

- examine heterogeneity and spatial variability at scales smaller than global climate model grid boxes to assess the representativeness of local measurements for regional processes and provide essential perspectives on upscaling of key measurements and process understanding;
- link processes across key interfaces of the coupled system;
- explore the influences of large-scale forcing on local processes, including the basin-scale variability in atmospheric forcing, sea ice-thickness distribution, ocean-mixed layer depth, and more, by measuring local spatial gradients of properties and capturing floe-scale ice and snow variability; and
- study two-dimensional and three-dimensional processes and their evolution in time.

These overarching concepts lend themselves to addressing a number of specific scientific questions. For example, what role do transient processes play in ocean vertical mixing, how do ice dynamics contribute to the temporal evolution of the ice thickness distribution and the heat flux between ocean and atmosphere, or how is surface momentum transfer shaped by mesoscale atmospheric divergence? In addition to focusing on local and regional processes around the drifting MOSAiC setup, the DN autonomous observing systems also helped to link the MOSAiC observations to a pan-Arctic network of autonomous buoy observations coordinated by the International Arctic Buoy Programme.

This work gives a descriptive account of the performance of the MOSAiC DN and shows the added value by examples of specific scientific cases, in particular with respect to the spatial variability in the observations. In Section 2, we summarize the approach and implementation of the DN, also in the context of prior work. We detail its performance and show exemplary results and analysis in Section 3. Section 4 provides a summary and discussion of the results in Section 3, further highlighting synergies with remote sensing measurements and numerical modelling studies. We conclude with an overall assessment of the MOSAiC-DN approach and its resultant implications for scaling in observations and numerical models.

2. METHODS: Observational approach and instrumentation

In this section, we give a detailed overview of the MOSAiC DN of autonomous instrument platforms (“buoys”), from the initial concept and planning, through the description of the different instruments and platforms, to the final implementation. While the general approach covers all implementations of this DN, we mainly describe the initial setup that occurred from October 2019 into July 2020. A second, less extensive network was implemented after relocation of the observatory to the central Arctic in August 2020.

A. Overall concept of the DN: scales and layout

The MOSAiC DN covered different scales of variability inherent to the individual sub-systems of the Arctic Ocean:

- In the atmosphere, mesoscale variability occurs at scales from approximately 2 km up to several 100 km, representing spatial variability in storm structure, wind patterns, cloud formation/structure, precipitation regimes, and other related processes.
- Sea ice and snow properties and processes can vary on similar scales as the atmosphere, but also have key modes of inter-floe versus intra-floe variability that can manifest on scales much smaller than 5 km.
- Ocean mesoscale variability is expected to be around 5–10 km, the size of the local first-mode baroclinic Rossby radius. Submesoscale variability is expected to be on the order of 1 km.

Importantly, the DN design needed to support observations that would link across these various scales in the different subsystems to enable the study of coupled processes. The optimal observation of isotropic anomalies uses a radially outward-oriented network of nodes (Chan et al., 1996). During the installation phase at the beginning of the MOSAiC field experiment, we implemented several of those nodes (hereafter referred to as “sites”) arranged in horizontal circles at different radii from the Central Observatory. To resolve the above-mentioned scales, we initially established 3 large (L) sites, 9 medium (M/LM) sites, and 86 single buoy geographic position (P) sites in the DN. These sites were planned to track cascading scales of 2 km, 5 km, 10 km and 15 km away from the Central Observatory, with a few additional units at even larger scales to link with the International Arctic Buoy Programme network (“Extended Network” in Figure 1); details are given in the supplemental material (Text S1 and Figures S1 and S2). However, the ice conditions and deployment opportunities required a much more flexible and diverse layout (Figure 1), where several sites were placed at greater distance due to the lack of ice floes sufficiently thick and close to the Central Observatory. The observations of the ocean and atmosphere from ice-tethered platforms, however, allowed coverage of scales beyond the spacing of sites and instruments due to measuring quasi-steady spatial variability while drifting with the sea ice. The final layout was influenced by additional constraints, such as not deploying too many buoys in a "logistics" corridor used for approaching supply vessels (see Text S1 and Figure S1), and the number of buoys the consortium was able to provide for deployment. Several fully autonomous instruments were also deployed at the Central Observatory along with all of the attended instrumentation at that site, making the Central Observatory one of the buoy sites within the DN, and allowing direct comparisons between DN instrumentation and Central Observatory instruments not otherwise deployed in the DN.

This DN had to be dismantled as it approached the ice edge in Fram Strait at the end of July 2020, with a few buoys still working until 2022. In August 2020, a new buoy array was established in and around a new Central Observatory in the central Arctic near 87°N, though it was less extensive and featured only a small subset of the instrumentation of the first DN. The second, "mini" DN (hereafter termed "mDN") is briefly described in Text S2 which also provides references for further details. Here, we focus on the first DN (simply referred to as "DN").

Figure 1. Actual layout of the Distributed Network after completing all initial deployments on October 22, 2019.

b. Platforms and Instrumentation in the DN

The measurement concept of the DN is based on more than 30 different types of autonomous buoy platforms, as summarized in Table 1. Each type is unique with respect to technical specifications, measured variables, vertical and temporal resolution and data concept (formats, transmission, storage and data flow). In total, 234 buoys were deployed on, in, and under the sea ice during MOSAiC (Figure 2). Here we briefly describe the general characteristics of the different platform types. The list is sorted by the main sensors on each platform associated with atmospheric, snow and sea ice, and oceanographic measurements.

Atmospheric conditions were monitored with Atmospheric Surface Flux Stations (ASFS; Cox et al., 2023a; Figure 2a), measuring all components of the surface energy and momentum budgets, including up/down shortwave and longwave radiation, eddy-covariance based turbulent-sensible and latent-heat fluxes and momentum flux, and the snow-ice conductive heat flux derived from flux plates. These stations also measured near-surface air pressure, temperature, relative humidity, winds, radiometrically derived surface skin temperature, localized relative surface height (used to derive snow depth), and geographic position and heading. As the most complex surface stations, they were maintained whenever possible during their drift. The Central Observatory meteorological installation included a 3-level meteorological tower that measured a set of variables similar to the Atmospheric Surface Flux Stations (Shupe et al., 2022; Cox et al., 2023a). Wind measurements from the array of three L sites and the Central Observatory have been used to estimate low-level (approximately 3.8 m height) atmospheric divergence on an approximate 25 km scale. In addition, several other buoy types measured air temperature, radiative fluxes, and barometric pressure, but without any maintenance (e.g., Figure 2b, d and i).

Snow and sea ice mass balance were measured with different kinds of ice mass balance buoys (IMBs, Figure 2b, d, e, p and r), including thermistor strings providing profiles of temperature and thermal conductivity with a resolution of 0.02 m (Jackson et al., 2013), seasonal IMBs (Planck et al., 2019), and Snow Buoys that measure relative changes in snow depth (Nicolaus et al., 2021a; Figure 2c). Measurements of solar irradiance above and below the sea ice, including derivations of albedo and transmittance, were performed with different radiation stations (Figure 2b and q). Some radiation stations and IMBs also included measurements of additional bio-physical variables of the uppermost ocean. Sea ice drift and deformation was recorded by various types of geographic position-tracking buoys, including ice-Surface Velocity Profilers (iSVP; Figure 2o), ice trackers and the geographic position data provided by most other buoys. Some of these units reported barometric pressure and surface temperature. In addition, most of the units floated, which increased their chances of surviving ice deformation and complete melt out. Most position-tracking buoy and Snow Buoy data were transmitted to the Global Telecommunication System (GTS) by the World Meteorological Organization (WMO) and thus were available for near-real time analysis and inclusion in numerical weather forecasting. Surface photography was obtained by digital cameras on various units.

The backbone of oceanographic observations are measurements of conductivity, temperature, and pressure (Conductivity Temperature Depth, hereafter referred to as “CTD”) at various vertical levels and in different configurations, with salinity and depth derived directly from those variables. Woods Hole Ice-tethered profilers (Krishfield et al., 2008; Toole et al., 2011; 2016; Cole et al., 2015; Figure 2j), installed at the L sites, were among the most complex systems. Some of these profilers provided not only temperature and salinity, but also three-dimensional velocity, dissolved oxygen and bio-optical variables of the water column from 760 m to 7 m depth at a vertical resolution of about 1 m (1 dbar) at time intervals of a few hours to 1.5 days. The bio-optical variables included optical backscatter and fluorescence at different wavelengths related to the concentration of chlorophyll *a* and chromophoric dissolved organic matter (CDOM). Similar systems, the Drift-Towing Ocean Profiler (DTOP; e.g., Li et al., 2021a; Ocean Univeristy of China, 2024), covered most of these variables from under the ice to about 120 m depth. Other systems carried CTD sensors at fixed depths (e.g., Figure 2l and h) measuring at time intervals of a few minutes (Hoppmann et al., 2022a). A few of those systems also carried sensors for bio-optical variables, similar to those on the Woods Hole Ice-tethered Profilers, measuring close to the ice bottom. Eddy-correlation flux systems as part of the Autonomous Ocean Flux Buoys (e.g., Shaw et al., 2008; Stanton et al., 2012, Lee et al., 2022; Rabe et al., 2022; Figure 2m) directly observed the vertical fluxes of momentum, heat and salt in the ocean just underneath the ice, with Autonomous Ocean Flux Buoys making concurrent high-resolution profiles of horizontal current velocity in the upper 60 m. These profiles included the ocean mixed layer and the upper halocline (pycnocline) during much of the expedition, as well as dissipation-based thermal diffusivity and heat flux measurements at 50 m depth within the pycnocline. The combined, distributed deployment of these systems covered a depth range from just underneath the ice down to about 760 m as well as temporal scales of a few seconds to days.

The Unmanned (uncrewed) Ice Station combined measurements from all realms: the atmosphere, sea ice and snow, and the ocean (Lei et al., 2022a; Figure 2d). Compared with the traditional sea ice mass balance buoy, the special design of this buoy is to increase the observations of multi-spectral shortwave radiation of five layers within the ice to obtain the light attenuation coefficients of sea ice with different textures and to extend the measurements downward, focusing on the oceanic mixed layer, obtaining temperature and salinity at six layers with depths of 5–40 m.

c. Sites: Distribution of instruments within the DN

The three L sites contained the most comprehensive measurements of the atmosphere-ice-ocean system in the DN, including biological and biogeochemical variables in both water and sea ice (Table 1, Figure 2 and Table S1). They provided measurements in different local conditions (e.g., ice thickness, floe size and shape) and put the observations at the Central Observatory into context with the remainder of the region covered by the DN. The installation of Atmospheric Surface Flux Stations together with Autonomous Ocean Flux Buoys, Woods Hole Ice-tethered Profilers and IMBs enables a full characterization of the energy and momentum transfer across the coupled atmosphere-ice-ocean system. Deploying Atmospheric Surface Flux Stations in the DN afforded the opportunity to collect data suitable for examining the spatial variability in surface energy transfer related, for example, to differences in sea ice or snow thickness. At L3, the Unmanned (uncrewed) Ice Station was deployed, featuring various ice, ocean and air measurements (for details see above). Several IMBs of various types (SIMB3, SIMBA, IMBflex and IMB combined with radiation stations; see Table 1) and Snow Buoys were deployed to monitor the seasonal changes of ice thickness, snow depth and vertical temperature profile through the snow-covered ice layer across a range of initial ice thicknesses. Some of these buoys also measured biooptical and biogeochemical variables. The different buoy types were distributed within individual sites according to the scales detailed in Section 2a. For example, while one ocean profiler and one Atmospheric Surface Flux Station were sufficient to capture the conditions above and below the ice at an individual site, that site often had multiple IMBs to represent intra-floe variability in snow and sea ice.

The 9 M sites aimed to observe ocean mesoscale variability in the upper approximate 100 m, as well as snow and ice thickness, temperature, and basic local meteorological conditions. A few systems also recorded biological and biogeochemical variables. The main platforms at the M sites were a Snow Buoys and a variety of IMBs, and Salinity Ice Tether buoys measuring ocean properties with CTD sensors at selected depths (Table 1, Figure 2). Several M sites additionally had Drift-Towing Ocean Profilers. The scales covered by the M sites are suitable to validate the ice growth rate derived from satellite altimeter observations (e.g., Koo et al., 2021) and climate or sea ice forecast models (e.g., Pithan et al., 2023). The LM site was equipped differently than the other 8 M sites and the 3 L sites, featuring upper-ocean CTD measurements only close to the ice and additional instrumentation for radiation, more complex biophysical measurements and a sediment trap, in addition to IMB and Snow Buoys, as well as various non-telemetered devices. This site was accessible from the Central Observatory most of the time and was visited frequently for manual measurements and sampling, such as coring first-year and second-year ice. The LM site is counted as an M site throughout this paper.

The 86 P sites of the DN were distributed to capture ice deformation across the region around the Central Observatory. The priorities for placing P sites were to: (i) ensure that horizontal sea ice deformation was monitored in the 5 km surrounding the Central Observatory and L sites; (ii) capture deformation on 10, 20 and 40 km scales around the Central Observatory; and (iii) monitor deformation around the M sites. In addition, a few P site buoys were deployed along the icebreaker transits, several hundreds of kilometers away from the Central Observatory, to capture large-scale characteristics of sea ice kinematics and to obtain additional barometric pressure data. The platforms on the P sites consisted of different kinds of position-tracking buoys, and four IMBs (SIMBA, Table 1; Figure 2).

Figure 2. Photographs of selected autonomous platforms (buoys) deployed in the two implementations of the Distributed Network.

Table 1. Types of autonomous buoy systems used during MOSAiC.

d. Implementation of the main Distributed Network

The initial setup of the DN was accomplished in 12 days (October 5–16, 2019) from the Russian ice breaker *Akademik Fedorov*, which accompanied RV *Polarstern* during the initial MOSAiC setup phase. Details of this operation can be found in the cruise report by Krumpen and Sokolov (2020). During this time all 3 heavy equipment L sites, 8 of the 9 M sites and various geographic position tracking P sites were installed. The L sites required local icebreaker support for deployment and were revisited using a helicopter during the drift. Revisits allowed instrument maintenance and additional contextual measurements and sampling. The M sites were mostly deployed with helicopter support, and the P sites only by helicopter. These installations were a significant logistical challenge because of the very thin first year ice conditions, the limited space onboard the vessel, the short time window to complete deployment before loss of daylight and increasing sea ice formation. This task was achieved by having concurrent science teams prepare L site instrumentation in the large forward hold of *Akademik Fedorov*, while the rear of the ship was used to stage the M site and position-tracking buoy systems. A separate science team located the best available ice floes using high-resolution satellite-borne Synthetic Aperture Radar (SAR) imagery and helicopter surveys integrated with the M and P site instrument deployments. In addition, the availability of predictive model results (Krumpen et al., 2020) was of great benefit. Installations on the ice were performed by instrumentation groups, including early-career researchers from the onboard MOSAiC school and journalists who actively assisted in the deployments. This strategy allowed each L site (and parts of the M and P sites) to be surveyed and instrumented in less than 1.5 days. Parts of the deployment operations are sketched as digital drawings in Krueger and Rackow (2020). Concurrent to L site operations next to the ship, one of the two contracted MI-8 helicopters on *Akademik Fedorov* was employed to deploy instruments at the M and P sites.

In addition to the buoy installations, visual ice observations were carried out from the bridge by a group of three specially trained ice observers onboard *Akademik Fedorov*. Detailed descriptions of the methodology and protocols applied are provided in Alekseeva et al. (2019) and AARI (2011), all congruent with the WMO Sea Ice Nomenclature (2017). At each L site, a full floe survey was initiated by the science team and early-career researchers from the MOSAiC school. This survey included snow thickness measurements and ground-based electromagnetic induction surveys of ice thickness. In addition to the three L sites, extensive ice and snow thickness surveys were performed at M4 and M7 located within approximately 20 km of the Central Observatory. Details about the initial ice thickness and snow depth at the individual L sites are given in Krumpen and Sokolov (2020, their Chapter 2.1) and in Krumpen et al. (2021).

The deployent and conditions during the setup resulted in different scales covered by the DN, as shown in the map shortly after deployment (Figure 1). The L sites were at a distance similar to that planned and represent a compromise between logistically maintainable buoy sites (regular helicopter visits every few weeks), sufficient distance from the Central Observatory to measure a variety of local conditions, and the ability to capture mesoscale variability in the atmosphere. Due to lack of sufficiently thick ice floes close to the Central Observatory, the M sites ended up almost an order of magnitude farther away from the Central Observatory than planned. Section 4a includes a brief discussion of the consequences of observable scales.

During spring, helicopter deployment of additional buoys filled in gaps that had appeared in the DN and added another 15 km-diameter ring of position-tracking buoys around the Central Observatory. One position-tracking buoy was also placed about 80 km to the east of the Central Observatory, allowing synoptic scale drift and deformation monitoring. While RV *Polarstern* was away from the Central Observatory between mid-May and mid-June 2020 to facilitate a personnel rotation, the L2 Atmospheric Surface Flux Station (#30) operated from the Central Observatory to collect measurements in place of the temporarily decommissioned atmospheric installations there (at “Met City”; see Shupe et al., 2022; Cox et al., 2023a). In late April, Atmospheric Surface Flux Station #50 (originally from L3) was installed at the Central Observatory and operated there for much of the time until the end of July.

Although ice dynamics damaged several buoys during the drift, requiring additional maintenance where possible (e.g., Figure 3a), the majority of the DN was recovered in August 2020. The three L sites (L1–L3), LM, M1 and M3 were recovered by RV *Polarstern* between August 1 and August 7. In addition, M4, M5, and M6 were recovered by *Akademik Tryoshnikov*, which supported the rotation of personnel and equipment during much of August. The recovery included dismantling both broken units and still-active devices. All ice-tethered units were close to the end of their functionality in the broken and melting ice pack in Fram Strait; for example, a Woods hole Ice-tethered Profiler and a Snow Buoy shown in Figure 3b and c, respectively. Some floating systems (mostly position-tracking buoys) continued measurements and transmitted data from the North Atlantic Ocean into summer 2022. All buoy deployments with sites, dates and labels are given in Table S2.

Figure 3. Photographs of conditions during recovery of the Distributed Network platforms in 2020.

e. Methodological comparison to prior drift efforts

Spatially distributed autonomous measurements have been made as part of particular regional and temporally limited field campaigns, including, e.g., the Surface Heat Budget of the Arctic (SHEBA; Perovich et al., 1999; Andreas et al., 1999; 2010b; Perovich and Elder, 2002; Uttal et al., 2002; Shaw et al., 2009), the Tara drift (Gascard et al., 2008), AIDJEX (Untersteiner et al., 2009) and the 2015 Norwegian young sea ICE (N-ICE2015; Itkin et al., 2017; Granskog et al., 2018). Further efforts, such as the Marginal Ice Zone program in the Canada Basin (Lee et al., 2017) or the “Switchyard” in the central Arctic (SWITCHYARD, 2023; see also Falkner et al., 2005), had a strong focus on specific processes in selected regions. The MOSAiC approach differs methodologically from previous efforts insofar as its DN included not only more comprehensive observing systems but also covered spatial scales designed to resolve the mesoscale in the ocean and the lower end of the mesoscale in the atmosphere. In addition, the network spanned a greater variety of ice thicknesses and operated during a full year. During SHEBA, comprehensive autonomous observing systems were distributed within about 3 km distance from a Central Observatory, consisting of stations for atmospheric variables and fluxes as well as ice and snow mass balance (Perovich et al., 1999; Andreas et al., 1999; 2010a; 2010b; Perovich and Moritz, 2002); comprehensive ocean observations were only carried out at the Central Observatory. Another example is N-ICE2015, where 42 autonomous systems were located within 5–100 km from the ship, but the majority were ice mass balance and ice position-tracking buoys (Itkin et al., 2017), without any distributed ocean observations. The Marginal Ice Zone Project (https://apl.uw.edu/project/project.php?id=miz) distributed different atmosphere-ice-ocean observing systems across several hundred kilometers in the central Canada Basin, synoptically covering a larger area with measurements but with lower effective spatial resolution than the MOSAiC DN. Thus, the MOSAiC DN combined the scales covered with the multitude of instrumentation in an unprecedented way, with the largest deployment of ice-tethered position-tracking buoys to date, over scales capturing individual active leads up to the kinematic response to synoptic weather patterns (see Watkins et al., 2023).

3. Results

We illustrate the results that can be obtained from the DN, first briefly outlining the performance and drift tracks of the whole network for the full duration of MOSAiC. We then show examples of the coupled-system observations during a period in winter and a period in early summer; the former represents a little-observed season in the central Arctic, while the latter covers the period when the ship and all personnel had left the MOSAiC domain leaving only autonomous observations. Aspects of the full seasonal cycle of specific variables have been analyzed elsewhere (e.g., Lei et al., 2022a; Nicolaus et al., 2022; Rabe et al., 2022; Bliss et al., 2023; Itkin et al., 2023), and a detailed description is beyond the scope of this overview paper. We do not detail the results of the mDN in this work either and refer, instead, to the analyses already published or expected to be submitted (e.g., Katlein et al., 2020; Flores et al., 2023). All times/dates are given in UTC.

a. Operation and drift tracks of the DN

Figure 4 shows that all DN sites generally followed the drift of the Central Observatory (see Shupe et al., 2020, their Figure 2). Text S3 and Table S3 detail the source of each position track defining the individual DN sites. The life cycle of each buoy is detailed in Figure S6. Figure 5 shows that the DN drifted with the transpolar drift, crossed Fram Strait and drifted into the Greenland Sea. The transpolar drift was faster than expected, generally faster than the previous 15 years, including the N-ICE2015 drift (see Section 2e); only one year had faster drift speeds in Fram Strait (Krumpen et al., 2021; Dethloff et al., 2022). After the buoys came close to the edge of the marginal ice zone in the Greenland Sea in August, 2020, those buoys that were not recovered continued to drift, some circulating through the sea ice over the Greenland shelf and some exiting the marginal ice zone into open water (Watkins et al., 2023).

Figure 4. Drift tracks of the main sites of the Distributed Network.

During the DN drift (Figure 5), the original relative distribution remained approximately intact for the entire winter drift across the central Arctic, even though deformation on various scales within the DN (see Section 3c) led to damage of some of the instrumentation (e.g., Figure 3a). Several snapshots of L3 during mid-winter (Figure 6) show that significant deformation took place during January and February. In particular, a large crack crossed the site and subsequently developed into a pressure ridge that destroyed several of the nearby buoy systems (see Figure 6). L1 suffered deformation during late November/early December and late February, whereas L2 was more stable. Further, ice surface roughness increased overall through April and May 2020 (von Albedyll et al., 2022), and significant melting ensued after late May. As the DN approached the northern end of Fram Strait in early May, the DN site distribution began to strain along a south-southwest to north-northeast line, which became more distinct as it passed through Fram Strait in June and July. The overall timing of the drift has been analyzed in Dethloff et al. (2022) and is discussed further in Section 4a.

Figure 5. Evolution of the Distributed Network from mid-October 2019 to late July 2020.

Figure 6. Surface elevation maps of site L3 in mid-winter from airborne laser scanner observations.

To illustrate DN observations during the Arctic winter, in Sections 3b to 3d, we show data from various buoys, descriptively identifying vertical coupling and three-dimensional spatial features associated with different physical processes. We focus on a 30-day period from December 20, 2019, to January 19, 2020, when the DN drifted primarily from southeast to northwest, with deviations from the almost-straight track near the beginning and the end (Figure 7).

Figure 7. Geographic position of sites within the Distributed Network from late December to late January.

b. Wintertime variability in the atmosphere and feedback with sea ice, snow and ocean

Some meteorological processes are associated with transient atmospheric forcing, such as clouds or synoptic/mesoscale variability, occurring on scales that are set by the Rossby radius of deformation, which is close to the scale of the DN measurements. Other processes are associated with heterogeneity of the sea ice, which has smaller spatial length scales (see Section 3c).

Figure 8 shows the atmospheric conditions at the 4 sites in the DN that featured detailed, temporally high-resolution atmospheric observations during this 30-day mid-winter period, when the distances from each site to the Central Observatory did not vary in time by more than 1 km.

The near-surface air temperature (T_a; Figure 8a) varied with time, ranging from –37.6°C (December 29) to –16.1°C (December 22), a range of values that is similar to that observed during winter in the Beaufort Sea (Persson et al., 2002), while larger wintertime variability has been observed over sea ice closer to the North Atlantic (Cohen et al., 2017). The spatial differences (Figure 8a) were smaller than the temporal range, being no more than 5°C, and generally transient. Figure 8b shows the large temporal variation of the downwelling longwave radiation (LW_d), which is the primary forcing of T_a (Figure 8a) during winter, similar to that shown in the western Arctic winter by Persson et al. (2002). The spatial variability was usually much lower than the temporal variability (up to 80 W m^{-2}), but could briefly approach similar values during transition periods. In the dark of winter, the net atmospheric energy flux to the surface is given by $F_{atm} = LW_d - LW_u - Hs - H_l$, where LW_u is the upwelling longwave radiation, and H_s (H_l) is the turbulent sensible (latent) heat flux. During the winter period, the spatial variability (range across sites) of the mean LW_d, T_a, and F_{atm} were 1.8 W m^{-2}, 0.3°C, and 2.4 W m^{-2}, respectively (Table 2). The variability for LW_d was less than the accuracy of the pyrgeometers used (Cox et al., 2023a) and, therefore, does not indicate a measurable spatial difference in the mean LW_d. That the atmospheric forcing supplied by LW_d was uniform on average across the DN is not surprising due to the spatial extensiveness and predominance of stratiform clouds, as observed during SHEBA (Stramler et al., 2011; Persson et al., 2017; see also Section 2e). The spatial variability of the other two variables was slightly larger than their expected accuracies; while the differences were still small, these may reflect spatial differences in the means caused by sensitivity of T_a and F_{atm} to differences in the snow depth and/or ice thickness between the sites. This sensitivity is briefly discussed in Section 3d.

Figure 8. Time series of 10-minute means for meteorological measurements from late December to late January.

Table 2. Mean values of downwelling longwave radiation (LW_d), near-surface air temperature (T_a), and net surface energy flux (F_{atm}) measured at the 4 atmospheric sites in the Distributed Network December 20, 2019–January 19, 2020.

During the selected winter period, no strong storms passed over the DN and winds remained less than 10 m s^{-1} at the observed heights. However, there were several time periods of large changes in wind direction, with two of them associated with high pressure (December 20–22; January 9), one during the extended period of lower pressure (December 31–January 1) and another long one with the passage of a low-pressure center (January 16–19). Significant spatial variability in wind direction occurred during some of these transition times, though the wind speed was often weak. The atmospheric divergence calculated from the wind measurements at the L sites is one measure of spatial variability in low-level winds (Figure 8f), and during this relatively quiet period divergence mostly remained less than 10^{-4} s^{-1}. One longer period of atmospheric convergence occurred for 48 h during January 1–2 when the easterly wind speed was modest (7–10 m s^{-1}) and varied across the DN, with the wind at the southwestern side of the DN (L1) being the weakest. The wind direction also varied slightly across the DN, producing this extended period of low-level convergence. The DN was at this time affected by the outer fringes of a strong low-pressure center (968 hPa) located in the Kara Sea far to the south (see NCEP reanalysis at NOAA; Kalnay et al.,1996), though with no obvious frontal passage within the DN effecting a shift in wind direction.

Figure 8 suggests that there were timing differences in the large temporal changes in T_a and LW_d between the L sites, producing short periods of significant spatial variability. To illustrate the ability of the atmospheric measurements within the DN to capture the spatial variability of lower atmospheric processes, in this case the effects of clouds, Figure 9 shows a detailed time series of LW_d, T_a, and F_{atm} at the three L sites and the Central Observatory over a 12 h time period. This time interval exhibited spatial variability of 50–80 W m^{-2} in LW_d, up to 5°C in T_a, and up to 50 W m^{-2} in F_{atm}, with significant temporal variability in this spatial variability. This variability was caused by the transient passage of areas of variable cloud cover over horizontal scales less than the extent of the DN (see also Kay et al., 2016) that are discussed briefly in Section 4a.

Figure 9. Time series of atmospheric variables between 17:00 December 26 and 06:00 December 27 in 2019.

c. Wintertime ice dynamics and feedback with atmosphere and ocean

Buoys measuring geographic position at 47 sites were active during this 30-day winter period, enabling characterization of motion and deformation at a range of scales. The ensemble mean drift speed followed the wind speed in time (Figure 10a). While the correlation between the wind speed and ice drift time series is high (Pearsons's correlation coefficient equal to 0.9), the ice was not in free drift and experienced forces other than the local wind drag, including internal ice stresses and ocean drag. There were clearly quiescent intervals in the DN drift variance (Figure

10b), indicating times when the whole array was moving as one (notably December 25–29 and January 3–5). As most of the buoys were separated by small to moderate distances, the ensemble standard deviation responds more strongly to deformation at scales similar to the distance across the L site triangle, and most events with high ensemble standard deviation coincided with high shear or divergence in the L site array. Turning angles (difference between the ice drift direction and wind direction) were generally about 27 degrees to the right during these 30 days (Figure 10d) with intermittently strong variability. Though the mean ice drift to wind speed ratio (drift speed ratio) was 0.02, it was not constant throughout the time series (Figure 11e), with time periods when the ice moved more in response to the wind (e.g., December 31–January 3; January 16–18; high drift speed ratio) and others when the ice was converging and the apparent wind factor reduced (January 6–8; January 18–19; low drift speed ratio). The latter indicates times when ice internal stresses were dissipating wind momentum transferred to the ice. During periods of large ice drift speed ratios, momentum transfer to the ice and the ocean was enhanced. Of the 11 large-scale shearing events (Figure 10g), only four (December 31, and January 8, 18 and 19) coincided with large local shifts in wind direction. These events are associated with small drift speed ratios (a higher fraction of wind momentum being transferred to internal ice stress) and large turning angles. Under convergent conditions, the ice pressure that leads to local ridging may have been produced by wind shifts at a distance well beyond the L sites, rather than locally. Both the drift ratios and the turning angles exhibited spatial variability between the sites that was generally much smaller than the temporal variability, though a few brief periods had more pronounced spatial variability (e.g., the drift speed ratio at L1 is much larger for part of January 1).

As sea ice deformation and shear occur heterogeneously at different scales (Marsan et al., 2004; Hutchings et al., 2012; Itkin et al., 2017), we analyze the hourly divergence and shear (Figure 11f and g) at two scales: from the ring of buoys on the DN perimeter, representing the larger scale of the full DN, to a smaller scale from the triangle linking the three L sites. The difference between deformation of the triangle formed by the L sites and the perimeter of the DN (Figure 10f) demonstrates how local deformation can vary from the larger-scale aggregate motion. Figure 11f and g show that the local shearing event on January 13 occurred within the L site triangle, which opened and sheared, and is associated with ridging (convergence and decrease in area) across the full DN, while only moderate shear was observed at the large scale. Conversely, on January 6, strong convergence and shear occurred on the large scale, with very weak convergence and little shear occurring on the small scale.

Sea ice divergence and shear occur along quasi-linear active leads and ridges which arrange into shear zones (Kwok, 2001; Spreen et al., 2017). These shear zones can extend hundreds of kilometers, and during December 20–January 19 we observed 11 distinct large-scale shearing events that extended across the DN and produced a shear signature on the large scale (Figure 10g). These events are apparent in the drift trajectories and are marked by large-scale shear above 1 x 10^6 s^{-1}. Shear events happen across a continuum and thus the number of events depends on the threshold used. Most of these events occurred between December 30–January 2. Interestingly, few large-scale shearing events coincided with shear events calculated from the L sites, indicating that most large-scale events did not split the L site triangle, as evidenced by the stable distances between sites (see also Section 3b). Furthermore, the times of many of these large-scale shearing events did not coincide with the shifts in local wind direction and speed seen in Figure 11a and c, suggesting the remote wind forcing discussed earlier. Local deformation and spatial variability in deformation can be related to the physical response of the ice to the local wind forcing and sub-diurnal changes in ocean currents. Those large-scale shearing events that split the DN into two pieces can often be identified both from the differential motion of buoys (Watkins et al., 2023b) and/or an increase in variance of the buoy speeds during the events (Figure 10b). Both large drift speeds and large variances are associated with six large-scale ice dynamics events between December 30–January 18. The first five of these coincided with shear that extended across the full DN. During January 16–17, ice drift variance increased without shearing, which only first occurred at the end of this period near the beginning of January 18 and into January 19. This time period is associated with a transition from the predominantly high atmospheric pressure conditions driving ice convergence during most of the 30 days to lower pressure with more variable divergence across the DN (see Figures 8e and 12f).

Figure 10. Time series of ice drift and deformation from late December to late January.

We see a semi-diurnal fluctuation in mean ice drift with an amplitude of approximately 0.01 m s^{-1} (Figure 10), indicative of ocean forcing from tides and/or inertial motion in the upper ocean (e.g., Hinkins, 1967; McPhee, 1978; Gimbert et al., 2012). At individual L sites this semi-diurnal variation was more prominent during periods of strong wind (Figure 10a). These fluctuations illustrate the coupling between the ice and the ocean (see also Section 3e), while the atmosphere shows no semi-diurnal cycles. These cycles are also not apparent in the ice divergence and shear, indicating that, during the majority of the period, the response was coherent at the scale of the DN, as expected for inertial motions, and had a loss of coherence on smaller spatial scales. The mechanical dissipation in the ice was episodic, and during convergence we do not see the semi-diurnal upper ocean currents modulating the deformation. The ocean response is discussed further in Section 3e.

d. Wintertime ice thermodynamics and feedback with the atmosphere and ocean

Distributed measurements of snow and ice were made throughout the DN to sample variability in ice and snow thermodynamics and mass balance. The snow depth between different sites and within individual sites was variable. During the winter period, the observations from 13 IMB buoys (SIMBA, see Table 1) deployed over the DN, the Central Observatory, and the L and M sites, were available for the analysis of sea ice thermodynamic mass balance processes and their feedback to the atmospheric forcing (Lei et al., 2022a). The 30-day average snow depth ranged from 0.14–0.33 m (Figure 11a), with both the largest and the smallest snow depths observed at the Central Observatory (approximately 2 km from the ship) and the LM site, respectively. These results indicate that, at the DN scale, there was no significant difference in snow depth on level ice among the sites. However, at the scale of an individual floe, the ice surface topography around the location of individual buoys and snow redistribution processes affected the spatial distribution of snow depth. This effect has been confirmed in the transect measurements of snow depth at the Central Observatory (Itkin et al., 2023), where the regions near ice ridges preferentially accumulated snow. On average, there was no significant accumulation of snow based on the 13 IMBs during the 30 days. The variability in snow depth at various sites indicates snow redistribution and local effects.

At the beginning of the winter period, the ice thickness range was 0.80–1.80 m across the sites (Figure 11b). The ice bottom at all sites had entered the growth stage, with a 30-day mean ice growth rate ranging from 0.003–0.008 m d^{-1}. Therefore, the sea ice thickened by 0.10–0.24 m over 30 days. The differences in ice growth rates were regulated mainly by sea ice thickness (Stefan, 1891; Maykut and Untersteiner, 1971; Maykut, 1978). The ice thickness can explain 44% of the ice growth rate at these 13 sites ($P < 0.05$); that is, thin ice has a higher growth rate due to the higher conductive heat flux through the ice layer.

The ice temperature was regulated mainly by the net atmospheric energy flux (F_{atm} in Section 3b, Figure 8), which includes both radiative and turbulent atmospheric fluxes, and the conductive fluxes modulated by snow and sea ice thickness (Figure 11). From December 20 to January 2, the ice layer was generally in a gradually cooling state (Figure 11c). The bulk-average ice temperature through the ice layer decreased from –7.0°C to –8.7°C during this period, which can be attributed mainly to the overall negative values of F_{atm} and contributed to the weakly negative trend in T_a (Figure 8a). Subsequently, the bulk-average ice temperature remained relatively stable, and even increased slightly by the end of these 30 days (Figure 11c), as the air temperature was relatively steady and the thickness of sea ice gradually increased (Figure 11b). The conductive heat flux at the top ice layer (0–0.10 m) is often balanced by the heat released from the snow-covered ice layer to the near-surface atmosphere (F_{atm}), assuming that the conductive heat flux at the snow-sea ice interface is continuous. We have not directly calculated the conductive heat flux through the snow layer, as the texture of the snow layer at various measurement sites showed significant differences, which increases the uncertainty of the calculation. Instead, we use the conductive heat flux at the top of the ice layer to illustrate the contribution of the snow-covered ice layer to the surface heat balance. This heat flux reveals strong spatial differences, with the 30-day averages in the range of 32–118 W m^{-2}. The lowest heat flux was obtained from the Central Observatory because of the largest snow depth; the highest heat flux was at L3 because of the relatively small snow depth (0.17 m) and ice thickness (1.09 m). The observed heat flux does not show a clear temporal trend, with the multiple-site average in the range of 41–75 W m^{-2}. The changes in near-surface air temperature can explain 55% of the temporal variability of this heat flux ($P < 0.001$).

e. Vertical forcing in the upper ocean and mesoscale horizontal variability

During the 30-day case study, the drifting DN spanned a spatial gradient in absolute salinity in the upper-ocean mixed layer with generally higher values in the southwest and lower values in the northeast of the area surveyed, as seen in the absolute salinity at the M sites (Figure 12). This DN-scale gradient is embedded in the large-scale gradient in near-surface salinity and freshwater content between the Eurasian and Amerasian basins (e.g., Steele et al., 1998; Rabe et al., 2011). Note that the instantaneous distance across all sites was approximately 50 km, and their relative distances were stable to within 1–2 km (see also Figure 7). We observed interspersed mesoscale and smaller-scale features, represented by variations in absolute salinity over a few kilometers or less. These features are noticeable even at depths of 75–100 m (Figure 13).

Figure 11. Snow and sea ice mass balance data from late December to late January.

Figure 12. Horizontal distribution of absolute salinity at 10 m depth from late December to late January.

Figure 13. Absolute salinity at discrete depths across the Distributed Network from late December to late January.

The upper-ocean mixed layer, based on profiles of density (derived from pressure, conservative temperature and absolute salinity) at the L sites, exhibited variability on weekly to sub-daily time scales (Figure 14). In particular, the observations at L3 captured short-term variability due to rapid sampling, with profiles every 3 hours. Overall, a thickening mixed layer was observed, though the trend was much smaller than the short-term variability. The changes at the different sites were 0.17–0.30 m day^{-1}, equivalent to a thickening of 4–9 m from December 20 to January 19 (Figure 14). This compares to a thickening between October to March of around 30 m (Rabe et al., 2022, their Figure 9) and seasonal ranges in the eastern Arctic generally 50 m or higher, though based on observations largely near the continental slopes (Peralta Ferriz and Woodgate, 2015). Note that the short-term variability observed at L3 shows stronger peaks as the mesoscale and smaller-scale processes were better sampled, unlike L1 and L2 where the signal from these processes is aliased. The overall thickening of the mixed layer was likely forced primarily by the continuous surface cooling (negative net atmospheric energy flux; Section 3b, Table 2, Figure 10d) and ice growth (Section 3c, Figure 11) adding brine and, hence, leading to haline convection in the upper water column (see, e.g., Foster, 1969; Smith and Morison, 1998; Backhaus and Kaempf, 1999). The depth was also limited by the central Arctic end-of-melting-season stratification, different to less stratified regions (e.g., as much as 100 m north of Svalbard in winter; Koenig et al., 2016; Meyer et al, 2017). Intermittently, however, the depth of the mixed layer was strongly governed by the interplay of surface-forced momentum flux and changing stratification, as outlined below.

Figure 14. Time series of mixed layer depth at sites L1–3 from late December to early January.

We hereafter focus on the ocean velocity magnitude response and upper ocean stratification at sites L1 and L3 from measurements by the Autonomous Ocean Flux Buoys; the eddy correlation turbulence measurements and resulting heat, salt and momentum fluxes are analyzed elsewhere (B Shaw and T Stanton, personal communication). The two sites were located approximately 35 km apart and illustrate important similarities and differences seen at this scale, in particular the ocean response to atmosphere-ice forcing. Differences between the wind speed and ice speed (Figure 16a and d) reflect a combination of ice mobility, deformation and lead formation, discussed in Section 3c, and potentially differing atmosphere-ice and ice-ocean drag coefficients through the time series (see also Cole et al., 2017). The time series of current speed profiles (Figures 16b and e) show the formation of shallow wind-forced turbulent layers (see also Shaw et al., 2008; Cole et al., 2014) extending down from the ice-ocean interface during each of the stronger wind events. This effect is most clearly seen in wind events during December 29 to January 4 and January 9–18. The strong, transient forcing of these winds resulted in significant levels of inertial ringing in the water column (and ice), revealed as near-diurnal vertical stripes in current magnitude superimposed on the lower frequency mean response. The penetration depth of these ice-ocean shear-forced Ekman layers was strongly dependent on the water column stratification. Even small vertical density gradients in the water column rapidly diminished local turbulent mixing as turbulent kinetic energy was expended while entraining less buoyant fluid from below.

Surprisingly high levels of stratification were observed shallower than the strong winter halocline (pycnocline) depth at about 35 m during this period. The high levels of mesoscale density structure in the mixed layer (Figure 16c and f) profoundly affected upper ocean mixing and momentum transfer from the ice into the ocean (B Shaw and T Stanton, personal communication). The strong salt-stratified density gradients at the top of the halocline, or bottom of the mixed layer, were also observed as transitions in vertical current structure reflecting high shear levels at this interface. The sloped vertical stripes in Figure 15b and e within the strongly stratified pycnocline indicate inertial motions propagating into the deeper ocean. Examples of the reduction of turbulent mixing depth by these weak vertical density gradients can be seen by comparing the full mixed layer depth (35 m; Figure 14) Ekman layer at L1 (Figure 15b and c) formed during the strong January 13 winds with the much shallower penetration of the enhanced current layer at L3 (Figure 15e and f). There, near-surface vertical density gradients as shallow as 15 m depth (Figure 15f) shoaled between January 13 and 15. As this wind event continued January 14–17, L3 drifted over part of a strong halocline eddy feature seen clearly in enhanced currents at the top of the domed pycnocline that shoaled as shallow as 25 m depth. Currents arising from this eddy were largely isolated from the mixed layer above by the strong halocline density gradient, and thus did not affect the ice speed.

Figure 15. Wind, ice and ocean speed, and ocean density, from late December to late January .

Figure 16. Wind speed, upper ocean currents and ice inertial band motion, late December to late January.

Significant differences in vertical and horizontal density structure between L1 and L3 (Figure 15) within the mixed layer emphasize the small scale of the upper-ocean mesoscale features. Although the feature centered on December 24 was clearly observed in the profiling Woods Hole Ice-tethered Profiler at both L sites and the 10-minute records of conservative temperature and absolute salinity at M4 (Figure 13a), the following feature at L1, centered on December 30, was encountered 1–2 days later at L3, M1 and M6 as more diffuse features (Figures 13b and 15f). The mesoscale features are associated with strong changes in density profile structure, varying over distances comparable to the 1st-mode baroclinic Rossby radius and have been identified at different times during the operation of the DN (e.g., Hoppmann et al., 2022a). They can reach downward well into the upper halocline and even touch the lower halocline, here around 60–100 m (see, e.g., Rabe et al., 2022, their Figure 10). Smaller-scale differences between sites as well as synoptic variability are visible at all depths, evident in particular at 75 m throughout the time period (Figure 13).

Time series of surface winds, upper ocean current magnitude, inertial-band energy, and ice inertial band motion for L1, L3 and the Central Observatory (Figure 16) show accelerations of the upper mixed layer currents concurrent with the onset of high levels of inertial motion in the ocean-ice coupled layer, in response to a strong transient wind event starting on December 29. This inertial ringing of the ice coupled into the ocean mixed layer is seen widely in the Arctic (e.g., Brenner et al., 2023), but usually in conditions of lower ice coverage and high ice mobility in late summer and fall. The ocean inertial currents at each of the three sites (Figure 17c) show some spatial variability compared with the more coherent spatial response of the ice (Figure 16d), largely because of differences in the mixing layer depth through which the inertial momentum is distributed at each site. The actively mixing layer did not always extend to the bottom of the mixed layer (e.g., Schulz et al., 2022, their Figure 4) that had been homogenized previously. Overall, this strong inertial response in mid-winter is indicative of the relatively weak and mobile ice pack encountered during the MOSAiC drift. Differences in the magnitude of the ice inertial oscillations between the three DN observation stations (Figure 16d) are likely indicative of the local mobility of the ice pack.

f. DN observations during the temporal gap in Central Observatory measurements

The two main benefits of the autonomous DN instrumentation are the spatially distributed nature of the observations and their ability to fill temporal gaps in the manual measurements at the Central Observatory. Even when the latter had to be suspended from May 16 to June 18, 2020, due to RV *Polarstern* leaving for a personnel exchange, the DN continued to obtain data from 83.4°N to about 82.4°N (dashed-line box in Figure 4). We can clearly see the near-freezing T_a after melt onset (Light et al., 2022) on May 25 (Figure 17d), indicative of a melting ice and snow surface (Figure 17) from excess surface energy flux (Persson et al., 2012) and eventually leading to increasing radiation into the upper ocean after about June 4 (Figure 18c).

Figure 17. Late-spring snow and sea ice mass balance and conductive heat flux at the ice surface.

As shown in Figure 17a–c the cold interior of the sea ice warmed gradually (see also Lei et al., 2022a; Salganik et al., 2023) from May to June 2020, through warming from both above and below. The increased sea ice temperature suggests that the volume fraction of brine was gradually increasing and gradually enhanced its permeability (Golden et al., 1998). Intermittent surface cooling (e.g., June 2–12), however, led to superimposed ice in June, that can be identified in data from IMB (SIMBA, Table 1) heat cycles at L2 and L3 and that is not visible in the temperature data alone (Lei et al., 2022a). The snow cover had completely melted away at L1 and L2 by June 8 and 16, 2020, respectively (Figure 17a and b). At the L3 IMB (SIMBA, Table 1) the snow cover thinned to 0.10 m by June 18 and melted completely by June 24. Similarly, snow melt continued until June 29 when all the snow had melted and surface ice melt began, as observed by another L2 IMB (SIMB3, Table 1; Perovich et al., 2023). These observations indicate the spatial heterogeneity of surface snow melting, mainly due to initial snow depth and surface topography, that was documented thoroughly by the IMB observations and the manual surveys during the early setup of the DN.

The conductive heat flux at the surface 0.1 m layer of ice cover was affected mainly by near-surface air temperature, with the daily near-surface air temperature explaining 25% ($P < 0.01$) of the conductive heat flux (Figure 17). After the relatively warm period May 25–30, 2020, the snow began to melt faster and exhibited greater spatial differences, which gradually increased the spatial differences in conductive heat flux at the sea ice surface. Overall, the conductive heat flux on the sea ice surface remained negative (downward), except for the temporary positive heat conduction (upward) caused by relatively low air temperatures on May 17. The dominant heat flux indicates that during this period May 16–June 18, the sea ice layer mainly acquired heat from the atmosphere, which is the main source of energy that warmed and melted the ice. Especially during the warmer periods, May 26–30 and after June 16, the downward conductive heat flux was more pronounced.

There are obvious spatial differences at times when the bottom of the sea ice began to melt, ranging between May 17 and June 20, 2020, across 15 IMB (SIMBA, Table 1) in the DN, which mainly depends on the thicknesses of sea ice and the overlying snow cover (Lei et al., 2023a). While the seawater temperature forcing under all DN sites was similar, the relatively thin sea ice at some locations made the ice layer more sensitive to seasonal surface warming, leading to earlier melt onset at those locations. Basal ice melt at various IMB (SIMBA, Table 1) at L1, L2 and L3 commenced on June 15, June 20 and June 12, respectively (Figure 17), concurrent with an ocean-to-ice heat flux of around 10 W m^{-2}, about 5 times the December-to-April mean (Lei et al., 2022a). In addition, a seasonal IMB (SIMB3, Table 1) deployed at L2 observed the bottom ice melt at this site beginning June 11, 2020 (Perovich et al., 2023). At the Central Observatory the earliest basal melt was observed on May 27 (Salganik et al., 2023), and melt ponds started to form at the same time (Webster et al., 2022). Freshening just under the ice with the formation of under-ice meltwater layers was observed by the IMB (SIMBA, Table 1) temperature profiles, at L1 and L2 on July 31 and June 26, respectively, but at L3 already on June 16 (Lei et al., 2022a). Also, in the Central Observatory the earliest record of under-ice meltwater layers was on June 16 (Smith et al., 2022; Salganik et al., 2023). The difference in timing of under-ice meltwater layers may be related to the thinner ice present at L3 and part of the Central Observatory. This thinner ice could have allowed earlier meltwater drainage, lower draft or higher occurrence of ridges at these sites, each of which could have controlled the accumulation of meltwater below the ice (Salganik et al., 2023).

In the ocean, there was a shoaling of the upper-ocean mixed layer toward the end of the time period (see Rabe et al., 2022, their Figure 10, for Woods Hole Ice-tethered Profiler data from L1 without data gaps; see also Schulz et al., n.d.). The seawater temperatures were close to freezing, almost as low as the lowest observed in the DN further north during April. At the same time, absolute salinity was generally closest to that of Fram Strait inflow of Atlantic Water (Figure 18). One Salinity Ice Tether (SIT, Table 1) recorded almost equal conservative temperature and absolute salinity in the top 100 m at M3 until early June with a small increase thereafter (Figure 19), suggesting that the base of the mixed layer stayed deeper than that until June 15 at this location about 20 km from L2. However, a few warm spells occurred at M3 around 100 m depth and from about June 10 between about 50 m and 100 m depth (not shown). The deep signal is hinted at in the L2 Woods Hole Ice-tethered Profiler values deeper in the water column (Figure 18a) before the profiler was no longer able to reach the upper water column.

The automated observations in the DN at L2 were particularly important for the description of the phytoplankton bloom under the MOSAiC floe, which developed during the absence of RV *Polarstern* following the increase in photosynthetically active radiation in the water column under the ice (Figure 18c). This timing coincided not only with a general increase in incoming solar radiation (not shown) but also with the gradual melting of snow at L2 during June which, although differing across the floe, shows the overall disappearance of the snow cover. While the under-ice bloom was fully developed by the time that discrete sampling began again in the Central Observatory on June 16 (not shown), the Woods Hole Ice-tethered Profiler chlorophyll *a* fluorescence data indicate that the ecologically important onset of biomass increases occurred in the upper 30 m at the beginning of June, with subsequent deepening of biomass down to 70 m (Figure 18d). Despite the large-scale gradient in stratification shallower than 100 m from the Amundsen to the Nansen basins (Rabe et al., 2022, their Figure 10) the change in photosynthetically active radiation coincided with a small increase in upper ocean stratification starting on June 4 that covered approximately the top 100 m (Figures 18a and 19). Turbulent mixing, however, was still focused on the top 40–70 m most of the time in early May and late June, making likely that similar conditions prevailed during the time we focus on here (Schulz et al., 2022) and, thus, allowing phytoplankton to stay in that depth range (Figure 18d). Furthermore, the Woods Hole Ice-tethered Profiler chlorophyll *a* fluorescence data potentially indicates an export event of biomass from the sea ice in mid-May, which would fit well with the observed melt onset dates in the DN, as described above. Further analysis is needed to confirm this export event, such as that done by Laney et al. (2014) for prior observations.

Figure 18. Ocean properties late May to early June, observed by Woods Hole Ice-tethered Profiler #94 at site L2.

Figure 19. Absolute salinity at discrete depths at site M3 from late May to early June.

4. DISCUSSION

a. Discussion of DN results and synergies with remote sensing and other observations

Our observational results outlined in Section 3 describe the overall drift of the buoys and illustrate the ability of the MOSAiC DN to resolve spatially variant coupled-system processes, from small scale to mesoscale, and fill temporal gaps during the drift by autonomously observing even in the absence of manual observations. Here, we address these results considering existing literature and show synergies with remote sensing and other observations.

From the different ice observations and electromagnetic induction surveys we know that the region of the DN was initially covered primarily by first-year ice, with approximately 10% being multi-year ice that survived from the previous growth year (Krumpen et al., 2021, their Figure 5a). The observations stem from the marginal ice zone, that was found far north in the central Arctic, and follow a long-term shift in ice types across the Arctic. Warming and reduced sea ice cover have been reported during 1990–2018 in the Bering and Chukchi seas (Danielson et al., 2020), and the eastern Arctic is also approaching a state of seasonal ice cover (Haine and Martin, 2017; Perovich et al., 2020). Therefore, the observed prevailing pattern of first-year ice during the DN drift appears to be a “normal feature” on the pan-Arctic scale.

During our 30 mid-winter days, atmospheric near-surface variability was strongest at time scales of less than one day, and temporal variability was much larger than spatial variability most of the time; the latter was also true for wind-driven ice motion. Although the monthly-mean (winter) atmospheric variables observed immediately above the surface were small, relative to the temporal variability, there were differences in the air temperature and the net atmospheric energy flux between sites. These differences influenced the ice temperature across the DN, also considering the conductive heat flux through the variable snow cover. The conductive heat flux through the snow varied between sites in the mean over the 30 days as well as showing temporal variability. The latter can be explained by changes in air temperature to more than 50%, in contrast to the late spring/early summer situation (Figure 11d), where we find these changes to be only about half that. This difference can be explained by the complex thermodynamic characteristics of the snow and sea ice surfaces during the melting period, such as significant temporal changes in snow moisture content (Sturm et al., 2002; Nicolaus et al., 2003). Ice growth appears to have been dominated by absolute ice and snow thickness at each buoy, with the highest heat flux coinciding with the smallest ice and snow thickness. This result indicates that as Arctic sea ice thins, heat released from the sea ice-ocean system towards the near-surface atmosphere in winter can be expected to increase, assuming the snow depth does not increase. It also means that ice growth rates would increase accordingly (Stefan, 1891; Maykut and Untersteiner, 1971). Our preliminary analysis does not suggest a strong influence of storms on sea ice formation, such as found by Graham et al. (2019) for N-ICE2015 (see Section 2e), though the observed sudden changes in wind direction (Figure 8) likely led to events in the ice dynamics (e.g., Figure 10g) and some lead formation (Section 3c) that may have released heat and moisture from the ocean directly to the atmosphere.

The effect of atmosphere-ice-ocean momentum transfer was subject to internal dynamical processes in both the sea ice and the ocean. The DN position observations, which resolve ice motion on a large range of time scales, show that the sea ice motion is strongly correlated with the near-surface wind, as is the upper portion of the ocean mixed layer, where significant spatial and temporal variability was observed. However, deformation in the sea ice is only sometimes linked with wind transitions, whereas at times the ice-internal stresses dampened the momentum transfer from the atmosphere. Consolidated ice cover generally damps momentum transfer between the atmosphere and the ocean heterogeneously (Cole et al., 2017), although that dampening is generally more pronounced in the marginal ice zone (Manucharyan and Thompson, 2017) than in the even more consolidated ice cover we observed. Ocean mixed layer horizontal density gradients and deeper ocean eddies also impacted the mixed layer currents. Hence, the dynamics of all three media played a role in the dynamics of the ice and the ocean surveyed, while neither the ice nor the ocean seems to have impacted the observed winds significantly during our 3-day mid-winter period.

The ocean observations in the DN show a complex interplay between spatial and temporal variability. Even though the mesoscale and sub-mesoscales were not resolved instantaneously, we could observe quasi-synoptic features, such as eddies, often at more than one site over time periods of one to several days; some of these features were in direct contact with the surface, while others were isolated by local stratification close to the surface. Studying those processes in detail is beyond the scope of this work, as that generally involves direct and indirect feedbacks between ocean, ice and atmosphere. The reader is referred to ocean-focused studies, such as Hoppmann et al. (2022), Kawaguchi et al. (2022), Kuznetsov et al. (2023), and Fang et al. (n.d.).

Apart from the small influence of snow and ice conditions on the mean atmospheric variables near the surface, the DN captured several transient atmospheric features with substantially shorter time scales than the 30 mid-winter days, such as clouds, fronts and pressure gradients of the passing synoptic systems. This atmospheric variability forced the observed divergence of sea ice and brief departures from the overall thermodynamic homogeneity. Here, we illustrate the combined use of the DN observations and a scanning Ka-band radar (provided by the Department of Energy Atmospheric Measurements Program), mounted on top of the bridge of RV *Polarstern*. The radar observations (Figure S4) reveal details of how a shallow, spatially limited cloud field produced the variability in LW_d (see also Figure 9) across the DN. Near 23:00 UTC December 26, the skies were mostly clear across the domain, with low values of LW_d. Shortly before 00:00 UTC December 27, a region of clouds crossed the domain from the southwest (L1) and sequentially raised the LW_d by 40–50 W m^{-2} across the different sites, with related increases in F_{atm} and T_a and subsequent decreases in LW_d, T_a, and F_{atm}. The changes in F_{atm} represent the changes in the atmosphere's net thermodynamic forcing of the sea ice surface. Similarly, the ship-mounted C-band radar onboard RV *Polarstern*, using a similar digitizing system approach as the N-ICE2015 campaign (Oikkonen et al., 2017), captured the very episodic (hours to days) and localized sea ice deformation events. These radar observations agree with our findings on sea ice deformation in Section 3a and c and highlight the benefit of covering different scales with the DN and this radar.

Due to the invisibility from space and the reduced accessibility for in situ sampling, observations of under-ice phytoplankton blooms in the Arctic are sparse (Ardyna et al., 2020), hence the MOSAiC DN observations from late spring/early summer cover a gap in knowledge. The previously available data from the 1950s (Apollonio, 1959; English, 1961) indicate that blooms under multi-year ice started later (i.e., at the end of June) but developed higher biomass than observed by the DN. During SHEBA (Section 2e) two phytoplankton blooms were observed around the Chukchi Plateau and the southeastern Makarov Basin from late May 1998 to early September 1998, covering a similar vertical range as the DN observations, though with an order of magnitude higher concentration of chlorophyll *a* (Sherr et al., 2003). More recent observations below central Arctic first-year ice (Boles et al., 2020) indicate similar timing and magnitude of under-ice blooms as observed in the DN.

Overall, the DN captured variability at the scales set out to be studied in MOSAiC, even though the upper ocean mesoscale and sub-mesoscales could not be resolved in the way planned. However, the varying ice drift during several selected time periods still allows a detailed, quasi-synoptic analysis of both the sub-mesoscale and mesoscale ocean variability. As the ocean was observed at a larger scale than planned, we can obtain a better impression of the conditions and dynamics on scales up to 40 km.

Further remote sensing observations during MOSAiC captured different temporal and spatial scales than the DN, including information on the deformation and morphological changes in the ice surface by satellite, airborne, and surface-based remote sensing; for example, SAR-based ice-motion tracking (Nicolaus et al., 2022; Guo et al., 2023), melt pond distribution and albedo (Neckel et al., 2023, Sperzel et al., 2023), sea ice topography (Hutter et al., 2023; see also Figure 6), and sea ice thickness (von Albedyll et al., 2022; see map of airborne campaigns parallel to MOSAiC in Figure S5). Analyzing these data sets in conjunction with DN observations has been the subject of studies targeting specific variables and aspects of the MOSAiC coupled system.

b. DN model applications and synergies

The MOSAiC observations, in particular those by the DN, provide a unique opportunity to facilitate model and forecast improvements. The WMO Year of Polar Prediction (YOPP) initiative, aimed to advance polar prediction capabilities (Jung et al., 2016), coordinated its international efforts between 2013 and 2022 with MOSAiC. In particular, several operational Numerical Weather Prediction centers saved additional model parameters at high temporal and spatial resolutions along the MOSAiC track to enable in-depth analyses, evaluation, and forecast improvements of the coupled Arctic atmosphere-ice-ocean system (e.g., Bauer et al., 2020; Solomon et al., 2023). Promising studies exemplifying the value of MOSAiC data in general for model evaluation have already been appearing (e.g., Dethloff et al., 2022). In the following we provide only selected examples of how the information about spatial heterogeneity measured by the DN can provide added value to evaluating models and forecast systems.

The MOSAiC campaign was provided with real-time sea ice drift forecasts by the Sea Ice Drift Forecast Experiment (SIDFEx) for the Central Observatory and a number of DN sites to facilitate satellite image ordering and other logistical tasks (Nicolaus et al., 2022). The representation of sea ice deformation in models has been studied widely (e.g., Spreen et al., 2017; Rampal et al., 2019) and a recent study by Korosov et al. (2023) highlights the potential of assimilating satellite-derived sea ice deformation to improve sea icesea ice deformation forecasts up to 3–4 days. One could use the SIDFEx forecasts to compare the sea ice deformation forecast skill of a broad range of forecast systems with lead times up to 10 days. The systems with spatial resolutions of 5–12 km (e.g., Guiavarc'h et al., 2019), though designed to represent average behavior on scales of about 100 km and weeks to months (Blockley et al., 2020), may be able to forecast deformation events on the scale of the outer ring of the DN, like those described in Section 3c.

Figure 20. Comparison of wintertime observations and 2-day forecasts during October 15, 2019–March 15, 2020.

The DN observations have also been used to evaluate coupled processes unique to the Arctic in forecast systems, such as the representation of low-level clouds, the representation of the stable boundary layer, atmosphere-snow interaction, and ocean-sea ice-atmosphere coupling (see Solomon et al., 2023). Such evaluations are illustrated in Figure 20, where observations of wintertime skin temperature, measured with the Atmospheric Surface Flux Stations at the L sites and from the Central Observatory meteorological installation, and of the surface ice temperature, measured with several IMB (SIMB3, Table 1), are compared to forecasts from five state-of-the-art coupled forecast systems at a 2-day lead time. The observed low frequency skin temperature variability is simulated by all the forecast systems. This close correspondence with observations is not seen for the surface ice temperature (Figure 20b), where the modeled temperatures differ by ±10°C from the observations by the different IMB. The DN provides observations that cover a variety of conditions within a model grid box, thereby substantially enhancing the ability to evaluate and improve simulations of the coupled Arctic system.

The Next Generation Earth Modelling Systems (nextGEMS) global storm- and eddy-resolving models with European Centre for Medium-Range Weather Forecasts (ECMWF) Integrated Forecasting System and the ICOsahedral Nonhydrostatic model represent a new class of kilometer-scale climate models that are the starting point for climate adaptation “Digital Twins” (Bauer et al., 2021a; 2021b). With grid box sizes well below 10 km (e.g., 4.4 km), they resolve linear kinematic features in the sea ice cover and the scale of the DN with tens to hundreds of points (not shown). Whether these kilometer-scale models start to feature some of the Arctic sub-grid variability (with respect to more typical 100 km climate model grid boxes) or whether they still suffer from being too spatially homogeneous can also be answered with the unique DN observations.

Comparing observations to model simulations generally suffers from differences between the internal variability of the model and the observations (e.g., Strobach and Bel, 2017; Jain et al., 2023). One effective way of maximizing the value of field-campaign data for climate model evaluation is to “nudge” the large-scale circulation in climate models, as demonstrated for MOSAiC data by Pithan et al. (2023). Another example is a high-resolution implementation of an ocean-only model with an irregular grid, sigma vertical coordinates and a level upper (ice) boundary, where the ocean is nudged by the seawater temperature and salinity observed in the ocean by the DN, allowing to resolve sub-mesoscale and mesoscale features (Kuznetsov et al., 2023).

5. CONCLUSIONS

The MOSAiC Distributed Network of autonomous ice-tethered “buoy” platforms operated during the drift from the eastern Eurasian Arctic to Fram Strait in late 2019 through the first half of 2020, and with a reduced setup from late summer to early autumn 2020, after relocation to the central Arctic in late summer. The network was comprised of different instrument systems clustered around individual nodes or sites to observe the coupled atmosphere-ice-ocean climate system in the central Arctic. Instrument systems had varying complexity, ranging from comprehensive flux stations to simple position-tracking drifters. All instrumentation not only recorded autonomously but relayed most of the data via satellite to land or via radio link to the central MOSAiC ship, with the remaining data obtained during maintenance visits or after recovery. Our work presented here has focused on the utility of the MOSAiC DN for observing spatial variability on model grid scales, exploiting the autonomous nature of the instruments.

The DN observations were able to capture simultaneously both vertical processes at a single ice floe and horizontally heterogeneous processes on scales of 10–100 km, as well as on smaller scales quasi-synoptically along the drift. In addition to complex autonomous instruments, the distributed deployment of position-tracking buoys has provided information about the localized and aggregate ice dynamics, allowing relationships to the wind and ocean forcing to be identified. Importantly, the DN sites compared to crewed observations at the Central Observatory are able to provide unique insights into how representative single floe comprehensive measurements are of conditions across scales of 10–100 km, and can give long-duration estimates of the spatial heterogeneity of the coupled atmosphere, ice and ocean systems. The DN successfully observed the transition to ice melt in late spring/early summer and the change between the regions affected by low-salinity polar surface waters and those affected by near-surface waters of Atlantic origin. The corresponding time period, when the Central Observatory was unattended, was a critical time to complete our observations of the full seasonal cycle of the ice within the DN, including optical measurements of biology and chemistry, all subject to changing rapidly with climate change

(Bluhm et al., 2020; Mortenson et al., 2020). Hence, there is a continuous need for more telemetered, autonomous observations, such as those of the DN. Our results also emphasize the need to carefully consider the difference of ice thickness and overall ice topography (e.g., ridges) at various buoy deployment sites, which may cause significant small-scale changes in mass and energy exchanges between atmosphere, sea ice and ocean.

The comprehensive nature of the instruments, and the parallel operation of an icebreaker and ice-floe-scale Central Observatory with complementary measurements and manual sampling, are important aspects of the MOSAiC DN and are unprecedented in their entirety. Together they facilitate analysis of processes that would not be possible with either clusters of autonomous instrumentation separated by larger distances than the DN sites or the stand-alone use of autonomous systems. The scientific value of the DN reaches in multiple directions. The multitude of temporal and spatial scales covered by the DN make it particularly suited to upscaling and downscaling of information, including scales that are less than large-scale model grid cells. Collectively, these observations support improved model parameterizations of ocean, sea ice, and atmosphere processes along with their key coupling interactions, as well as unique new possibilities for model validation. Lastly, this successful implementation demonstrates the feasibility of such networks and provides key guidance for future autonomous observing network installations, which ought to become more common in a warming world where everyone, including scientists, have to reduce their emissions.

Acknowledgments

This work was carried out and data used in this manuscript were produced as part of the international Multidisciplinary drifting Observatory for the Study of the Arctic Climate (MOSAiC) with the tag MOSAiC20192020. We thank all persons involved in the expedition of the Research Vessel *Polarstern* during MOSAiC in 2019–2020 (AWI_PS122_00) as listed in the general MOSAiC acknowledgement (Nixdorf et al., 2021). In particular, we would like to thank teachers and young scientists of the MOSAiC summer school who helped with deployment of the DN from *Akademik Fedorov*. A subset of the observations was provided by the Atmospheric Radiation Measurement (ARM) User Facility, a U. S. Department of Energy (DOE) Office of Science User Facility managed by the Biological and Environmental Research Program. We acknowledge the World Meteorological Organization's Polar Prediction Project, which contributed significantly to the conceptual design of the MOSAiC DN for use in model assessment and development.

Funding statement

The following projects and funding agencies contributed to this work:

- the German Federal Ministry of Education and Research (BMBF) through financing the Alfred-Wegener-Institut Helmholtz-Zentrum für Polar- und Meeresforschung (AWI), RV *Polarstern* expedition PS122 under the grant N-2014-H-060_Dethloff, and the projects EPICA (# 03F0889A), IceSense (03F0866A);
- the AWI through its projects: AWI_OCEAN, AWI_ICE, AWI_SNOW, AWI_ECO, AWI_ATMO, AWI_BGC. The AWI buoy program was funded by the Helmholtz strategic investment Frontiers in Arctic Marine Monitoring (FRAM);
- the U. S. National Science Foundation (OPP-1724551, OPP-1722729, OPP-1723400, OPP-1756100, OPP-2034919);
- the U. S. National Oceanographic and Atmospheric Administration's Physical Sciences Laboratory (NA22OAR4320151), Arctic Research Program, and Global Ocean Monitoring and Observing Program (FundRef https://doi.org/10.13039/100018302);
- the U. S. Department of Energy Atmospheric System Research Program (DE-SC0021341, DE-SC0021342);
- the Deutsche Forschungsgemeinschaft (DFG, German Research Foundation) through the Transregional Collaborative Research Centre TRR-172 "ArctiC Amplification: Climate Relevant Atmospheric and SurfaCe Processes, and Feedback Mechanisms (AC)^3" (grant 268020496);

- the European Union’s Horizon 2020 collaborative project NextGEMS (grant number 101003470);
- The project Sub-Mesoscale Dynamics and Nutrients (SMEDYN) within the INternational Science Program for Integrative Research in Earth Systems (INSPIRES) of the Alfred-Wegener-Institut Helmholtz-Zentrum für Polar- und Meeresforschung;
- the US Interagency Arctic Buoy Program (USIABP) support for the International Arctic Buoy Programme, which partially covered the satellite telemetry costs;
- the Research Council of Norway through project HAVOC (grant no 280292) and CAATEX (grant no 280531);
- the National Natural Science Foundation of China (grant grant number 41976219);
- the NOAA Global Ocean Monitoring and Observing (GOMO) Arctic Research Program (ARP; FundRef https://doi.org/10.13039/100018302) and the NOAA Physical Sciences Laboratory (PSL);
- the Met Office Hadley Centre Climate Programme funded by DSIT; and
- the European Commission for EU H2020 through the project Arctic PASSION (grant no. 101003472).

Author Contribution

Contributed to conception and design

BR, JH, JR, MDS, MH, MN, TS, TK, OP, WS

Contributed to acquisition of data

AJ, BR, DMW, JH, JO, JR, JT, KRC, MDS, MH, MN, MT, TK, TS, TR, OP, RL, RK, STC, WS

Contributed to analysis and interpretation of data

AJ, AS, BR, DMW, EB, HG, JH, JR, MAG, MDS, MH, MN, MT, OP, RL, TK, TS, VL

Drafted and/or revised the article

All authors

Approved the submitted version for publication

All authors

Competing interest

All authors declare that they have no competing interests.

Data accessibility statement

All data have been archived in the MOSAiC Central Storage (MCS) and in the data repositories PANGAEA and the Arctic Data Center. Most of the unprocessed, near-real-time data is available at seaiceportal.de for preview only. References to published data sets are cited in the text.

References

Alfred-Wegener-Institut Helmholtz-Zentrum für Polar- und Meeresforschung. 2017. Polar research and supply vessel POLARSTERN operated by the Alfred-Wegener-Institute. *Journal of Large-Scale Research Facilities* **3**: A119. DOI: http://dx.doi.org/10.17815/jlsrf-3-163.

Andreas, EL, Horst, TW, Grachev, AA, Persson, POG, Fairall, CW, Guest, PS, Jordan, RE. 2010a. Parametrizing turbulent exchange over summer sea ice and the marginal ice zone. *Quarterly Journal of the Royal Meteorological Society* **136**(649): 927–943. DOI: http://dx.doi.org/10.1002/qj.618.

Andreas, EL, Persson, POG, Grachev, AA, Jordan, RE, Horst, TW, Guest, PS, Fairall, CW. 2010b. Parameterizing turbulent exchange over sea ice in winter. *Journal of Hydrometeorology* **11**(1): 87–104. DOI: http://dx.doi.org/10.1175/2009JHM1102.1.

Andreas, EL, Fairall, CW, Guest, PS, Persson, POG. 1999: An overview of the SHEBA atmospheric flux program. In *Fifth Conference on Polar Meteorology and Oceanography*, Dallas, TX, January 10–15,1999, American Meteorological Society, Boston, MA, pp. 550–555 (preprint).

Apollonio, S. 1959. Hydrobiological measurements on IGY drift station Bravo. National Academy of Sciences IGY Bulletins 27. *Eos, Transactions American Geophysical Union* **40**(3): 316–319. DOI: http://dx.doi.org/10.1029/TR040i003p00269.

Ardyna, M, Mundy, CJ, Mayot, N, Matthes, LC, Oziel, L, Horvat, C, Leu, E, Assmy, P, Hill, V, Matrai, PA, Gale, M, Melnikov, IA, Arrigo, KA. 2020. Under-ice phytoplankton blooms: shedding light on the “invisible” part of Arctic primary production. *Frontiers in Marine Science* **7**. DOI: http://dx.doi.org/10.3389/fmars.2020.608032.

Athanase, M, Sennéchael, N, Garric, G, Koenig, Z, Boles, E, Provost, C. 2019. New hydrographic measurements of the upper Arctic western Eurasian Basin in 2017 reveal fresher mixed layer and shallower warm layer than 2005–2012 climatology. *Journal of Geophysical Research: Oceans* **124**(2): 1091–1114. DOI: http://dx.doi.org/10.1029/2018JC014701.

Bauer, P, Dueben, PD, Hoefler, T, Quintino, T, Schulthess, TC, Wedi, NP. 2021a. The digital revolution of Earth-system science. *Nature Computational Science* **1**(2): 104–113. DOI: http://dx.doi.org/10.1038/s43588-021-00023-0.

Bauer, P, Stevens, B, Hazeleger, W. 2021b. A digital twin of Earth for the green transition. *Nature Climate Change* **11**(2): 80–83. DOI: http://dx.doi.org/10.1038/s41558-021-00986-y.

Belter, HJ, Krumpen, T, von Albedyll, L, Alekseeva, TA, Birnbaum, G, Frolov, SV, Hendricks, S, Herber, A, Polyakov, I, Raphael, I, Ricker, R, Serovetnikov, SS, Webster, M, Haas, C. 2021. Interannual variability in Transpolar Drift summer sea ice thickness and potential impact of Atlantification. *The Cryosphere* **15**(6): 2575–2591. DOI: http://dx.doi.org/10.5194/tc-15-2575-2021.

Bliss, A, Hutchings, J, Anderson, P, Anhaus, P, Belter, H J, Berge, J, Bessonov, V, Cheng, B, Cole, S, Costa, D, Cottier, F, Cox, CJ, De La Torre, PR, Divine, DV, Emzivat, G, Fang, YC, Fons, S, Gallagher, M, Geoffrey, M, Granskog, MA, Haapala, J, Haas, C, Hoppmann, M, Høyland, KV, Hwang, B, Itkin, P, Johnsen, G, Juttila, A, Kanzow, T, Katlein, C, Kopec, T, Krishfield, R, Krumpen, T, Kuznetsov, I, Lange, B, Lei, R, Li, T, Mäkynen, M, Moore, R, Morgenstern, A, Morris, SM, Nicolaus, M, Olsen, LM, Osborn, J, Perovich, D, Persson, O, Petrovsky, T, Rabe, B, Raphael, I, Regnery, J, Ricker, R, Riemann-Campe, K, Rohde, J, Salganik, E, Shaw, B, Sheikin, I, Shupe, MD, Smolyanitsky, V, Sokolov, V, Stanton, T, Tao, R, Timofeeva, A, Toole, J, Uttal, T, Vogedes, D, Watkins, D, Zhu, J, Zolich, A, Zuo, G. 2022. Sea ice drift tracks from the Distributed Network of autonomous buoys deployed during the Multidisciplinary drifting Observatory for the Study of Arctic Climate (MOSAiC) expedition 2019–2021. *NSF Arctic Data Center*. DOI: http://dx.doi.org/10.18739/A21N7XP19.

Bliss AC, Hutchings JK, Watkins DM. 2023. Sea ice drift tracks from autonomous buoys in the MOSAiC Distributed Network. *Scientific Data* **10**(1): 403. DOI: http://dx.doi.org/10.1038/s41597-023-02311-y.

Bluhm BA, Janout, MA, Danielson, SL, Ellingsen, I, Gavrilo, M, Grebmeier, JM, Hopcroft, RR, Iken, KB, Ingvaldsen, RB, Jorgensen, LL, Kosobokova, KN, Kwok, R, Polyakov, IV, Renaud, PE, Carmack, EC. 2020. The pan-Arctic continental slope: sharp gradients of physical processes affect pelagic and benthic ecosystems. *Frontiers in Marine Science* **7**. DOI: http://dx.doi.org/10.3389/fmars.2020.544386.

Boles, E, Provost, C, Garçon, V, Bertosio, C, Athanase, M, Koenig, Z, Sennéchael, N. 2020. Under-ice phytoplankton blooms in the central Arctic Ocean: insights from the first biogeochemical IAOOS platform drift in 2017. *Journal of Geophysical Research: Oceans* **125**(3): e2019JC015608. DOI: http://dx.doi.org/10.1029/2019JC015608.

Bourassa, MA, Gille, ST, Bitz, C, Carlson, D, Cerovecki, I, Clayson, CA, Cronin, MF, Drennan, WM, Fairall, CW, Hoffman, RN, Magnusdottir, G, Pinker, RT, Renfrew, IA, Serreze, M, Speer, K, Talley, LD, Wick, GA. 2013. High-latitude ocean and sea ice surface fluxes: challenges for climate research. *Bulletin of the American Meteorological Society* **94**(3): 403–423. DOI: http://dx.doi.org/10.1175/BAMS-D-11-00244.1.

Brenner, S, Thomson, J, Rainville, L, Crews, L, Lee, CM. 2023. Wind-driven motions of the ocean surface mixed layer in the western Arctic. *Journal of Physical Oceanography* **53**(7): 1787–1804. DOI: http://dx.doi.org/10.1175/JPO-D-22-0112.1.

Chan, FMM, King, TG, Stout, KJ. 1996. The influence of sampling strategy on a circular feature in coordinate measurements. *Measurement* **19**(2): 73–81. DOI: http://dx.doi.org/10.1016/S0263-2241(96)00067-X.

Clement Kinney, J, Assmann, KM, Maslowski, W, Björk, G, Jakobsson, M, Jutterström, S, Lee, YJ, Osinski, R, Semiletov, I, Ulfsbo, A, Wåhlström, I, Anderson, LG. 2022. On the circulation, water mass distribution, and nutrient concentrations of the western Chukchi Sea. *Ocean Science* **18**(1): 29–49. DOI: http://dx.doi.org/10.5194/os-18-29-2022.

Cohen, L, Hudson, SR, Walden, VP, Graham, RM, Granskog, MA. 2017. Meteorological conditions in a thinner Arctic sea ice regime from winter to summer during the Norwegian Young Sea Ice expedition (N-ICE2015). *Journal of Geophysical Research: Atmospheres* **122**(14): 7235–7259. DOI: http://dx.doi.org/10.1002/2016JD026034.

Cole, ST, Thwaites, FT, Krishfield, RA, Toole, JM. 2015. Processing of velocity observations from Ice-Tethered Profilers. *OCEANS 2015 - MTS/IEEE Washington*. Washington, DC, USA. DOI: http://dx.doi.org/10.23919/OCEANS.2015.7401887.

Cox, CJ, Gallagher, MR, Shupe, MD, Persson, POG, Solomon, A, Fairall, CW, Ayers, T, Blomquist, B, Brooks, IM, Costa, D, Grachev, A, Gottas, D, Hutchings, JK, Kutchenreiter, M, Leach, J, Morris, SM, Morris, V, Osborn, J, Pezoa, S, Preußer, A, Riihimaki, LD, Uttal, T. 2023a: Continuous observations of the surface energy budget and meteorology over the Arctic sea ice during MOSAiC. *Scientific Data* **10***(519)*. DOI: https://dx.doi.org/10.1038/s41597-023-02415-5.

Cox, C, Gallagher, M, Shupe, M, Persson, O, Blomquist, B, Grachev, A, Riihimaki, L, Kutchenreiter, M, Morris, V, Solomon, A, Brooks, I, Costa, D, Gottas, D, Hutchings, J, Osborn, J, Morris, S, Preusser, A, Uttal, T. 2023b. Met City meteorological and surface flux measurements (Level 3 Final), Multidisciplinary Drifting Observatory for the Study of Arctic Climate (MOSAiC), central Arctic, October 2019–September 2020. *NSF Arctic Data Center*. DOI: http://dx.doi.org/10.18739/A2PV6B83F.

Cox, C, Gallagher, M, Shupe, M, Persson, O, Grachev, A, Solomon, A, Ayers, T, Costa, D, Hutchings, J, Leach, J, Morris, S, Osborn, J, Pezoa, S, Uttal, T. 2023c. Atmospheric Surface Flux Station #30 measurements (Level 3 Final), Multidisciplinary Drifting Observatory for the Study of Arctic Climate (MOSAiC), central Arctic, October 2019–September 2020. *NSF Arctic Data Center*. DOI: http://dx.doi.org/10.18739/A2FF3M18K.

Cox, C, Gallagher, M, Shupe, M, Persson, O, Grachev, A, Solomon, A, Ayers, T, Costa, D, Hutchings, J, Leach, J, Morris, S, Osborn, J, Pezoa, S, Uttal, T. 2023d. Atmospheric Surface Flux Station #40 measurements (Level 3 Final), Multidisciplinary Drifting Observatory for the Study of Arctic Climate (MOSAiC), central Arctic, October 2019–September 2020. *NSF Arctic Data Center*. DOI: http://dx.doi.org/10.18739/A25X25F0P.

Cox, C, Gallagher, M, Shupe, M, Persson, O, Grachev, A, Solomon, A, Ayers, T, Costa, D, Hutchings, J, Leach, J, Morris, S, Osborn, J, Pezoa, S, Uttal, T. 2023e. Atmospheric Surface Flux Station #50 measurements (Level 3 Final), Multidisciplinary Drifting Observatory for the Study of Arctic Climate (MOSAiC), central Arctic, October 2019–September 2020. *NSF Arctic Data Center*. DOI: http://dx.doi.org/10.18739/A2XD0R00S.

d'Ovidio, F, De Monte, S, Alvain, S, Dandonneau, Y, Lévy, M. 2010. Fluid dynamical niches of phytoplankton types. *Proceedings of the National Academy of Sciences* **107**(43): 18366–18370. DOI: http://dx.doi.org/10.1073/pnas.1004620107.

Danielson, SL, Ahkinga, O, Ashjian, C, Basyuk, E, Cooper, LW, Eisner, L, Farley, E, Iken, KB, Grebmeier, JM, Juranek, L, Khen, G, Jayne, SR, Kikuchi, T, Ladd, C, Lu, K, McCabe, RM, Moore, GWK, Nishino, S, Ozenna, F, Pickart, RS, Weingartner, TJ. 2020. Manifestation and consequences of warming and altered heat fluxes over the Bering and Chukchi Sea continental shelves. *Deep Sea Research Part II: Topical Studies in Oceanography* **177**: 104781. DOI: http://dx.doi.org/10.1016/j.dsr2.2020.104781.

Dethloff, K, Maslowski, W, Hendricks, S, Lee, Y J, Goessling, H F, Krumpen, T, Haas, C, Handorf, D, Ricker, R, Bessonov, V, Cassano, J J, Kinney, J C, Osinski, R, Rex, M, Rinke, A, Sokolova, J, Sommerfeld, A. 2022. Arctic sea ice anomalies during the MOSAiC winter 2019/20. *The Cryosphere* **16**(3): 981–1005. DOI: http://dx.doi.org/10.5194/tc-16-981-2022.

English, TS. 1961. Some biological observations in the central North Polar Sea Drift Station Alpha, 1957–1958. *Scientific Reports No.* **15:** 1–80. Calgary, AB: Arctic Institute of North America.

Ermold, W, Rigor, I. 2023. In Situ Observations from the International Arctic Buoy Programme (IABP) 2017–2022, Level 1. *NSF Arctic Data Center*. DOI: http://dx.doi.org/10.18739/A20V89J8K.

Falkner, KK, Steele, M, Woodgate, RA, Swift, JH, Aagaard, K, Morison, J. 2005. Dissolved oxygen extrema in the Arctic Ocean halocline from the North Pole to the Lincoln Sea. *Deep Sea Research Part I: Oceanographic Research Papers* **52**(7): 1138–1154. DOI: http://dx.doi.org/10.1016/j.dsr.2005.01.007.

Fang, YC, Rabe, B, Kuznetsov, I, Hoppmann, M, Tippenhauer, S, Regnery, J, He, H, Li, T. n.d. Upper-ocean variability in the Amundsen Basin of the Arctic Ocean during early winter: insights from the MOSAiC expedition. *Elementa: Science of the Anthropocene* (submitted).

Flores, H, Veyssière, G, Castellani, G, Wilkinson, J, Hoppmann, M, Karcher, M, Valcic, L, Cornils, A, Geoffroy, M, Nicolaus M, Niehoff, B, Priou, P, Schmidt, K, Stroeve, J. 2023. Sea-ice decline could keep zooplankton deeper for longer. *Nature Climate Change* **13**(10): 1122–1130. DOI: http://dx.doi.org/10.1038/s41558-023-01779-1.

Fong, AA, Hoppe, CJM, Aberle, N, Ashjian, CJ, Assmy, P, Bai, Y, Bakker, DCE, Balmonte, JP, Barry, KR, Bertilsson, S, Boulton, W, Bowman, J, Bozzato, D, Bratbak, G, Buck, M, Campbell, RG, Castellani, G, Chamberlain, EJ, Chen, J, Chierici, M, Cornils, A, Creamean, JM, Damm, E, Dethloff, K, Droste, ES, Ebenhöh, O, Eggers, SL, Engel, A, Flores, H, Fransson, A, Frickenhaus, S, Gardner, J, Gelfman, CE, Granskog, MA, Graeve, M, Havermans, C, Heuzé, C, Hildebrandt, N, Hill, TCJ, Hoppema, M, Immerz, A, Jin, H, Koch, B, Kong, X, Kraberg, A, Lan, M, Lange, BA, Larsen, A, Lebreton, B, Leu, E, Loose, B, Maslowski, W, Mavis, C, Metfies, K, Mock, T, Müller, O, Nicolaus, M, Niehoff, B, Nomura, D, Nöthig, EM, Oggier, M, Oldenburg, E, Olsen, LM, Peeken, I, Perovich, DK, Popa, O, Rabe, B, Ren, J, Rex, M, Rinke, A, Rokitta, S, Rost, B, Sakinan, S, Salganik, E, Schaafsma, FL, Schäfer, H, Schmidt, K, Shoemaker, KM, Shupe, MD, Snoeijs-Leijonmalm, P, Stefels, J, Svenson, A, Tao, R, Torres-Valdés, S, Torstensson, A, Toseland, A, Ulfsbo, A, Van Leeuwe, MA, Vortkamp, M, Webb, AL, Gradinger, RR. n.d. Overview of the MOSAiC expedition: Ecosystem. *Elementa: Science of the Anthropocene* (submitted). Preprint at DOI: http://dx.doi.org/10.31223/X5P091.

GEBCO Bathymetric Compilation Group 2020. 2020. The GEBCO_2020 Grid – a continuous terrain model of the global oceans and land. *British Oceanographic Data Centre*, National Oceanography Centre, NERC, UK. DOI: http://dx.doi.org/10.5285/A29C5465-B138-234D-E053-6C86ABC040B9.

George, TM, Manucharyan, GE, Thompson, AF. 2021. Deep learning to infer eddy heat fluxes from sea surface height patterns of mesoscale turbulence. *Nature Communications* **12**(1): 800. DOI: http://dx.doi.org/10.1038/s41467-020-20779-9.

Gimbert, F, Jourdain, NC, Marsan, D, Weiss, J, Barnier, B. 2012. Recent mechanical weakening of the Arctic sea ice cover as revealed from larger inertial oscillations. *Journal of Geophysical Research: Oceans* **117**(C11). DOI: https://dx.doi.org/10.1029/2011JC007633.

Golden, KM, Ackley, SF, Lytle, VI. 1998. The percolation phase transition in sea ice. *Science* **282**(5397): 2238–2241. DOI: http://dx.doi.org/10.1126/science.282.5397.2238.

Graham, RM, Itkin, P, Meyer, A, Sundfjord, A, Spreen, G, Smedsrud, LH, Liston, GE, Cheng, B, Cohen, L, Divine, D, Fer, I, Fransson, A, Gerland, S, Haapala, J, Hudson, SR, Johansson, A M, King, J, Merkouriadi, I, Peterson, AK, Provost, C, Randelhoff, A, Rinke, A, Rösel, A, Sennéchael, N, Walden, VP, Duarte, P, Assmy, P, Steen, H, Granskog, MA. 2019. Winter storms accelerate the demise of sea ice in the Atlantic sector of the Arctic Ocean. *Scientific Reports* **9**(1): 9222. DOI: http://dx.doi.org/10.1038/s41598-019-45574-5.

Granskog MA, Fer I, Rinke A, Steen H. 2018. Atmosphere-ice-ocean-ecosystem processes in a thinner Arctic sea ice regime: The Norwegian Young Sea ICE (N-ICE2015) Expedition. *Journal of Geophysical Research: Oceans* **123**(3): 1586–1594. DOI: http://dx.doi.org/10.1002/2017JC013328.

Granskog, MA, Høyland, KV, De La Torre, PR, Divine, DV, Katlein, C, Itkin, P, Raphael, I, Olsen, LM. 2020. Temperature and heating induced temperature difference measurements from the sea ice mass balance buoy SIMBA 2020T60. 4 datasets. *PANGAEA*. DOI: http://dx.doi.org/10.1594/PANGAEA.924269

Global Runoff Data Centre (GRDC). 2023. Global Freshwater Fluxes into the World's Oceans. Online provided by Global Runoff Data Centre. Koblenz: Federal Institute of Hydrology (BfG).

Guiavarc'h, C, Roberts-Jones, J, Harris, C, Lea, DJ, Ryan, A, Ascione, I. 2019. Assessment of ocean analysis and forecast from an atmosphere–ocean coupled data assimilation operational system. *Ocean Sciences* **15**(5): 1307–1326. DOI: http://dx.doi.org/10.5194/os-15-1307-2019.

Guo, W, Itkin, P, Singha, S, Doulgeris, AP, Johansson, M, Spreen, G. 2023. Sea ice classification of TerraSAR-X ScanSAR images for the MOSAiC expedition incorporating per-class incidence angle dependency of image texture. *The Cryosphere* **17**(3): 1279–1297. DOI: http://dx.doi.org/10.5194/tc-17-1279-2023.

Haarsma, RJ, Roberts, MJ, Vidale, PL, Senior, CA, Bellucci, A, Bao, Q, Chang, P, Corti, S, Fučkar, NS, Guemas, V, Hardenberg, J von, Hazeleger, W, Kodama, C, Koenigk, T, Leung, LR, Lu, J, Luo, JJ, Mao, J, Mizielinski, MS, Mizuta, R, Nobre, P, Satoh, M, Scoccimarro, E, Semmler, T, Small, J, von Storch, JS. 2016. High Resolution Model Intercomparison Project (HighResMIP v1.0) for CMIP6. *Geoscientific Model Development* **9**(11): 4185–4208. DOI: http://dx.doi.org/10.5194/gmd-9-4185-2016.

Haas C. 2020. Links to master tracks in different resolutions of POLARSTERN cruise PS122/2, Arctic Ocean – Arctic Ocean, 2019-12-13 – 2020-02-24 (Version 2). *PANGAEA*. DOI: http://dx.doi.org/10.1594/PANGAEA.924674.

Haine, TWN, Curry, B, Gerdes, R, Hansen, E, Karcher, M, Lee, C, Rudels, B, Spreen, G, de Steur, L, Stewart, KD, Woodgate, R. 2015. Arctic freshwater export: status, mechanisms, and prospects. *Global and Planetary Change* **125**: 13–35. DOI: http://dx.doi.org/10.1016/j.gloplacha.2014.11.013.

Haine, TWN, Martin, T. 2017. The Arctic - Subarctic sea ice system is entering a seasonal regime: implications for future Arctic amplification. *Scientific Reports* **7**(1): 4618. DOI: http://dx.doi.org/10.1038/s41598-017-04573-0.

Hatakeyama, K, Hosono, M, Shimada, K, Kikuchi, T, Nishino, S. 2001. JAMSTEC Compact Arctic Drifter (J-CAD) : A new Generation drifting buoy to observe the Arctic Ocean, *Journal of the Japan Society for Marine Surveys and Technology* **13**(1): 55–68. DOI: http://dx.doi.org/10.11306/jsmst.13.1_55.

Herber, A, Becker, S, Belter, HJ, Brauchle, J, Ehrlich, A, Klingebiel, M, Krumpen, T, Lüpkes, C, Mech, M, Moser, M, Wendisch, M. 2021. MOSAiC expedition: airborne surveys with research aircraft POLAR 5 and POLAR 6 in 2020. *Reports on Polar and Marine Research* **754**: 1–99. Alfred-Wegener-Institut Helmholtz-Zentrum für Polar- und Meeresforschung. DOI: http://dx.doi.org/10.48433/BZPM_0754_2021.

Heuzé, C, Zanowski, H, Karam, S, Muilwijk, M. 2023. The deep Arctic Ocean and Fram Strait in CMIP6 models. *Journal of Climate* **36**: 2551–2584. DOI: http://dx.doi.org/10.1175/JCLI-D-22-0194.1.

Hoppmann, M, Kuznetsov, I, Fang, YC, Rabe, B. 2021a. Raw seawater temperature, conductivity and salinity obtained at different depths by CTD buoy 2019O4 as part of the MOSAiC Distributed Network. *PANGAEA*. DOI: http://dx.doi.org/10.1594/PANGAEA.933933

Hoppmann, M, Kuznetsov, I, Fang, YC, Rabe, B. 2021b. Raw seawater temperature, conductivity and salinity obtained at different depths by CTD buoy 2019O6 as part of the MOSAiC Distributed Network. *PANGAEA*. DOI: http://dx.doi.org/10.1594/PANGAEA.933941

Hoppmann, M, Kuznetsov, I, Fang, YC, Rabe, B. 2021c. Raw seawater temperature, conductivity and salinity obtained at different depths by CTD buoy 2019O7 as part of the MOSAiC Distributed Network. *PANGAEA*. DOI: http://dx.doi.org/10.1594/PANGAEA.933939

Hoppmann, M, Kuznetsov, I, Fang, YC, Rabe, B. 2022a. Mesoscale observations of temperature and salinity in the Arctic Transpolar Drift: a high-resolution dataset from the MOSAiC Distributed Network. *Earth System Science Data* **14**(11): 4901–4921. DOI: http://dx.doi.org/10.5194/essd-14-4901-2022.

Hoppmann, M, Kuznetsov, I, Fang, YC, Rabe, B. 2022b. Processed data of CTD buoys 2019O1 to 2019O8 as part of the MOSAiC Distributed Network: 8 datasets. *PANGAEA*. DOI: http://dx.doi.org/10.1594/PANGAEA.940320

Huang, Y, Taylor, PC, Rose, FG, Rutan, DA, Shupe, MD, Webster, MA, Smith, MM. 2022. Toward a more realistic representation of surface albedo in NASA CERES-derived surface radiative fluxes. *Elementa: Science of the Anthropocene* **10**(1): 00013. DOI: http://dx.doi.org/10.1525/elementa.2022.00013.

Hunkins, K. 1967. Inertial oscillations of Fletcher's Ice Island (T-3). *Journal of Geophysical Research* **72**(4): 1165–1174. DOI: http://dx.doi.org/10.1029/JZ072i004p01165.

Hutchings, JK, Heil, P, Steer, A, Hibler III, WD. 2012. Subsynoptic scale spatial variability of sea ice deformation in the western Weddell Sea during early summer. *Journal of Geophysical Research: Oceans* **117**(C1): 2011JC006961. DOI: https://dx.doi.org/10.1029/2011JC006961.

Hutchings, JK, Roberts, A, Geiger, CA, Richter-Menge, J. 2011. Spatial and temporal characterization of sea-ice deformation. *Annals of Glaciology* **52**(57): 360–368. DOI: http://dx.doi.org/10.3189/172756411795931769.

Hutter, N, Bouchat, A, Dupont, F, Dukhovskoy, D, Koldunov, N, Lee, YJ, Lemieux, JF, Lique, C, Losch, M, Maslowski, W, Myers, PG, Ólason, E, Rampal, P, Rasmussen, T, Talandier, C, Tremblay, B, Wang, Q. 2022a. Sea Ice Rheology Experiment (SIREx): 2. Evaluating Linear Kinematic Features in High-Resolution Sea Ice Simulations. *Journal of Geophysical*

Research: Oceans **127**(4): e2021JC017666. DOI: http://dx.doi.org/10.1029/2021JC017666.

Hutter, N, Hendricks, S, Jutila, A, Birnbaum, G, von Albedyll, L, Ricker, R, Haas, C. 2023. Gridded segments of sea-ice or snow surface elevation and freeboard from helicopter-borne laser scanner during the MOSAiC expedition, Version 1: 64 datasets. *PANGAEA*. DOI: http://dx.doi.org/10.1594/PANGAEA.950339.

Hutter, N, Hendricks, S, Jutila, A, Ricker, R, von Albedyll, L, Birnbaum, G, Haas, C. 2023. Digital elevation models of the sea-ice surface from airborne laser scanning during MOSAiC. *Scientific Data* **10**(1): 729. DOI: http://dx.doi.org/10.1038/s41597-023-02565-6.

Hutter, N., Hendricks, S., Jutila, A., Ricker, R., von Albedyll, L., Birnbaum, G., and Haas, C. (2023): Digital elevation models of the sea-ice surface from airborne laser scanning during MOSAiC. *Scientific Data* **10**(729). DOI: https://dx.doi.org/10.1038/s41597-023-02565-6.

IABP. 2023: https://iabp.apl.uw.edu/, last accessed 30 January, 2024.

Intergovernmental Panel On Climate Change (IPCC). 2022. The Ocean and Cryosphere in a Changing Climate: Special Report of the Intergovernmental Panel on Climate Change. 1st ed. Cambridge University Press. DOI: http://dx.doi.org/10.1017/9781009157964

Itkin, P, Hendricks, S, Webster, M, von Albedyll, L, Arndt, S, Divine, D, Jaggi, M, Oggier, M, Raphael, I, Ricker, R, Rohde, J, Schneebeli, M, Liston, GE. 2023. Sea ice and snow characteristics from year-long transects at the MOSAiC Central Observatory. *Elementa: Science of the Anthropocene* **11**(1): 00048. DOI: http://dx.doi.org/10.1525/elementa.2022.00048.

Itkin, P, Spreen, G, Cheng, B, Doble, M, Girard-Ardhuin, F, Haapala, J, Hughes, N, Kaleschke, L, Nicolaus, M, Wilkinson, J. 2017. Thin ice and storms: sea ice deformation from buoy arrays deployed during N-ICE2015. *Journal of Geophysical Research: Oceans* **122**(6): 4661–4674. DOI: http://dx.doi.org/10.1002/2016JC012403.

Jackson, K, Wilkinson J, Maksym, T, Meldrum, D, Beckers, J, Haas, C, Mackenzie, D. 2013. A novel and low-cost sea ice mass balance buoy. *Journal of Atmospheric and Oceanic Technology* **30**(11): 2676–2688. DOI: http://dx.doi.org/10.1175/JTECH-D-13-00058.1.

Jain, S, Scaife, AA, Shepherd, TG, Deser, C, Dunstone, N, Schmidt, GA, Trenberth, KE, Turkington, T. 2023. Importance of internal variability for climate model assessment. *NPJ Climate and Atmospheric Science* **6**(1): 68. DOI: http://dx.doi.org/10.1038/s41612-023-00389-0.

Jin, M, Deal, C, Maslowski, W, Matrai, P, Roberts, A, Osinski, R, Lee, YJ, Frants, M, Elliott, S, Jeffery, N, Hunke, E, Wang, S. 2018. Effects of model resolution and ocean mixing on forced ice-ocean physical and biogeochemical simulations using global and regional system models. *Journal of Geophysical Research: Oceans* **123**(1): 358–377. DOI: http://dx.doi.org/10.1002/2017JC013365.

Jonassen, MO, Chechin, D, Karpechko, A, Lüpkes, C, Spengler, T, Tepstra, A, Vihma, T, Zhang, X. 2020a. *Dynamical Processes in the Arctic Atmosphere*. In: Kokhanovsky, A, Tomasi, C, editors. Physics and Chemistry of the Arctic Atmosphere. Cham: Springer International Publishing. pp1–51. DOI: http://dx.doi.org/10.1007/978-3-030-33566-3_1.

Kalnay, E, Kanamitsu, M, Kistler, R, Collins, W, Deaven, D, Gandin, L, Iredell, M, Saha, S, White, G, Woollen, J, Zhu, Y, Chelliah, M, Ebisuzaki, W, Higgins, W, Janowiak, J, Mo, KC, Ropelewski, C, Wang, J, Leetmaa, A, Reynolds, R, Jenne, R, Joseph, D. 1996. The NCEP/NCAR 40-year reanalysis project. *Bulletin of the American Meteorological Society* **77**(3): 437–471. DOI: http://dx.doi.org/10.1175/1520-0477(1996)077<0437:TNYRP>2.0.CO;2.

Kanzow, T. 2020. Links to master tracks in different resolutions of POLARSTERN cruise PS122/3, Arctic Ocean – Longyearbyen, 2020-02-24 – 2020-06-04 (Version 2). *PANGAEA*. DOI: http://dx.doi.org/10.1594/PANGAEA.924681.

Katlein, C, Mohrholz, V, Sheikin, I, Itkin, P, Divine, DV, Stroeve, J, Jutila, A, Krampe, D, Shimanchuk, E, Raphael, I, Rabe, B, Kuznetsov, I, Mallet, M, Liu, H, Hoppmann, M, Fang, YC, Dumitrascu, A, Arndt, S, Anhaus, P, Nicolaus, M, Matero, I, Oggier, M, Eicken, H, Haas, C. 2020. Platelet ice under Arctic pack ice in winter. *Geophysical Research Letters* **47**(16). DOI: http://dx.doi.org/10.1029/2020GL088898.

Kawaguchi, Y, Koenig, Z, Nomura, D, Hoppmann, M, Inoue, J, Fang, YC, Schulz, K, Gallagher, M, Katlein, C, Nicolaus, M, Rabe, B. 2022. Turbulent mixing during late summer in the ice–ocean boundary layer in the central Arctic Ocean: results from the MOSAiC expedition. *Journal of Geophysical Research: Oceans* **127**(8): e2021JC017975. DOI: http://dx.doi.org/10.1029/2021JC017975.

Kay, JE, L'Ecuyer, T, Chepfer, H, Loeb, N, Morrison, A, Cesana, G. 2016. Recent advances in Arctic cloud and climate research. *Current Climate Change Reports* **2**(4): 159–169. DOI: http://dx.doi.org/10.1007/s40641-016-0051-9.

Kikuchi, T, Inoue, J, Langevin, D. 2007. Argo-type profiling float observations under the Arctic multiyear ice. *Deep Sea Research Part I: Oceanographic Research Papers* **54**(9): 1675–1686. DOI: http://dx.doi.org/10.1016/j.dsr.2007.05.011.

Koenig, Z, Provost, C, Villacieros-Robineau, N, Sennéchael, N, Meyer, A. 2016. Winter ocean-ice interactions under thin sea ice observed by IAOOS platforms during N-ICE2015: Salty surface mixed layer and active basal melt: *Journal of Geophysical Research: Oceans* **121**(10): 7898–7916. DOI: http://dx.doi.org/10.1002/2016JC012195.

Koenigk, T, Mikolajewicz, U, Haak, H, Jungclaus, J. 2007. Arctic freshwater export in the 20th and 21st centuries. *Journal of Geophysical Research: Biogeosciences* **112**(G4). DOI: http://dx.doi.org/10.1029/2006JG000274.

Koo, Y, Lei, R, Cheng, Y, Cheng, B, Xie, H, Hoppmann, M, Kurtz, NT, Ackley, SF, Mestas-Nuñez, AM. 2021. Estimation of thermodynamic and dynamic contributions to sea ice growth in the Central Arctic using ICESat-2 and MOSAiC SIMBA buoy data. *Remote Sensing of Environment* **267**: 112730. DOI: http://dx.doi.org/10.1016/j.rse.2021.112730.

Korhonen, M, Rudels, B, Marnela, M, Wisotzki, A, Zhao, J. 2013. Time and space variability of freshwater content, heat content and seasonal ice melt in the Arctic Ocean from 1991 to 2011. *Ocean Science* **9**(6): 1015–1055. DOI: http://dx.doi.org/10.5194/os-9-1015-2013.

Krishfield, R, Toole, J, Proshutinsky, A, Timmermans, ML. 2008. Automated Ice-Tethered Profilers for seawater observations under pack ice in all seasons. *Journal of Atmospheric and Oceanic Technology* **25**(11): 2091–2105. DOI: http://dx.doi.org/10.1175/2008JTECHO587.1.

Krueger, F, Rackow, T. 2020. The (drawn) Distributed Network around Polarstern, MOSAiC expedition. *Zenodo*. DOI: http://dx.doi.org/10.5281/ZENODO.3696854.

Krumpen, T, Birrien, F, Kauker, F, Rackow, T, von Albedyll, L, Angelopoulos, M, Belter, HJ, Bessonov, V, Damm, E, Dethloff, K, Haapala, J, Haas, C, Harris, C, Hendricks, S, Hoelemann, J, Hoppmann, M, Kaleschke, L, Karcher, M, Kolabutin, N, Lei, R, Lenz, J, Morgenstern, A, Nicolaus, M, Nixdorf, U, Petrovsky, T, Rabe, B, Rabenstein, L, Rex, M, Ricker, R, Rohde, J, Shimanchuk, E, Singha, S, Smolyanitsky, V, Sokolov, V, Stanton, T, Timofeeva, A, Tsamados, M, Watkins, D. 2020. The MOSAiC ice floe: sediment-laden survivor from the Siberian shelf. *The Cryosphere* **14**(7): 2173–2187. DOI: http://dx.doi.org/10.5194/tc-14-2173-2020.

Krumpen, T, von Albedyll, L, Goessling, HF, Hendricks, S, Juhls, B, Spreen, G, Willmes, S, Belter, HJ, Dethloff, K, Haas, C, Kaleschke, L, Katlein, C, Tian-Kunze, X, Ricker, R, Rostosky, P, Rückert, J, Singha, S, Sokolova, J. 2021. MOSAiC drift expedition from October 2019 to July 2020: sea ice conditions from space and comparison with previous years. *The Cryosphere* **15**(8): 3897–3920. DOI: http://dx.doi.org/10.5194/tc-15-3897-2021.

Kuznetsov, I, Rabe, B, Androsov, A, Fang, YC, Hoppmann, M, Quintanilla-Zurita, A, Harig, S, Tippenhauer, S, Schulz, K, Mohrholz, V, Fer, I, Fofonova, V, Janout, M. n.d. Dynamical reconstruction of the upper-ocean state in the central Arctic during the winter period of the

MOSAiC expedition. *EGUsphere preprint.* DOI: http://dx.doi.org/10.5194/egusphere-2023-1353.

Kwok R. 2001. Deformation of the Arctic Ocean sea ice cover between November 1996 and April 1997: A qualitative survey. In: Dempsey JP, Shen HH, editors. *IUTAM Symposium on Scaling Laws in Ice Mechanics and Ice Dynamics*. Dordrecht: Springer Netherlands. pp. 315–322. DOI: http://dx.doi.org/10.1007/978-94-015-9735-7_26.

Laney, SR, Krishfield, RA, Toole, JM, Hammar, TR, Ashjian, CJ, Timmermans, ML. 2014. Assessing algal biomass and bio-optical distributions in perennially ice-covered polar ocean ecosystems. *Polar Science* **8**(2): 73–85. DOI: http://dx.doi.org/10.1016/j.polar.2013.12.003.

Lee, CM, DeGrandpre, M, Guthrie, J, Hill, V, Kwok, R, Morison, J, Cox, C, Singh, H, Stanton, T, Wilkinson, J. 2022. Emerging technologies and approaches for in situ, autonomous observing in the Arctic. *Oceanography* **35**(3–4): 210–221. DOI: http://dx.doi.org/10.5670/oceanog.2022.127.

Lee, CM, Thomson, J, the Marginal Ice Zone Team, the Arctic Sea State Team. 2017. An autonomous approach to observing the seasonal ice zone in the western Arctic. *Oceanography* **30**(2): 56–68. DOI: http://dx.doi.org/10.5670/oceanog.2017.222.

Lei, R, Cheng, B, Hoppmann, M, Haapala, J, Lan, M. 2022b. Temperature and heating induced temperature difference measurements from SIMBA-type sea ice mass balance buoy 2019T56, deployed during MOSAiC 2019/20: 4 datasets. *PANGAEA*. DOI: http://dx.doi.org/10.1594/PANGAEA.940360.

Lei, R, Cheng, B, Hoppmann, M, Zhang, F, Zuo, G, Hutchings, JK, Lin, L, Lan, M, Wang, H, Regnery, J, Krumpen, T, Haapala, J, Rabe, B, Perovich, DK, Nicolaus, M. 2022a. Seasonality and timing of sea ice mass balance and heat fluxes in the Arctic transpolar drift during 2019–2020. *Elementa: Science of the Anthropocene* **10**(1): 000089. DOI: http://dx.doi.org/10.1525/elementa.2021.000089.

Lei, R, Cheng, B, Hoppmann, M, Zuo, G, Lan, M. 2022g. Temperature and heating induced temperature difference measurements from SIMBA-type sea ice mass balance buoy 2019T62, deployed during MOSAiC 2019/20: 4 datasets. *PANGAEA*. DOI: http://dx.doi.org/10.1594/PANGAEA.940231.

Lei, R, Cheng, B, Hoppmann M, Zuo, G. 2021b. Temperature and heating induced temperature difference measurements from SIMBA-type sea ice mass balance buoy 2019T66, deployed during MOSAiC 2019/20: 4 datasets. *PANGAEA*. DOI: http://dx.doi.org/10.1594/PANGAEA.938134.

Lei, R, Cheng, B, Hoppmann, M, Zuo, G. 2021c. Temperature and heating induced temperature difference measurements from SIMBA-type sea ice mass balance buoy 2019T67, deployed during MOSAiC 2019/20: 4 datasets. *PANGAEA*. DOI: http://dx.doi.org/10.1594/PANGAEA.938128.

Lei, R, Cheng, B, Hoppmann, M, Zuo, G. 2021d. Temperature and heating induced temperature difference measurements from SIMBA-type sea ice mass balance buoy 2019T69, deployed during MOSAiC 2019/20: 4 datasets. *PANGAEA*. DOI: http://dx.doi.org/10.1594/PANGAEA.938096.

Lei, R, Cheng, B, Hoppmann, M, Zuo, G. 2022c. Temperature and heating induced temperature difference measurements from SIMBA-type sea ice mass balance buoy 2019T58, deployed during MOSAiC 2019/20: 4 datasets. *PANGAEA*. DOI: http://dx.doi.org/10.1594/PANGAEA.940393.

Lei, R, Cheng, B, Hoppmann, M, Zuo, G. 2022d. Temperature and heating induced temperature difference measurements from SIMBA-type sea ice mass balance buoy 2019T64, deployed during MOSAiC 2019/20: 4 datasets. *PANGAEA*. DOI: http://dx.doi.org/10.1594/PANGAEA.940617.

Lei, R, Cheng, B, Hoppmann, M, Zuo, G. 2022e. Temperature and heating induced temperature difference measurements from SIMBA-type sea ice mass balance buoy 2019T68, deployed during MOSAiC 2019/20: 4 datasets. *PANGAEA*. DOI: http://dx.doi.org/10.1594/PANGAEA.940650.

Lei, R, Cheng, B, Hoppmann, M, Zuo, G. 2022f. Temperature and heating induced temperature difference measurements from SIMBA-type sea ice mass balance buoy 2019T72, deployed during MOSAiC 2019/20: 4 datasets. *PANGAEA*. DOI: http://dx.doi.org/10.1594/PANGAEA.940668.

Lei, R, Cheng, B, Zuo, G, Hoppmann, M, Lan, M. 2022k. Temperature and heating induced temperature difference measurements from SIMBA-type sea ice mass balance buoy 2019T70, deployed during MOSAiC 2019/20: 4 datasets. *PANGAEA*. DOI: http://dx.doi.org/10.1594/PANGAEA.940659.

Lei, R, Cheng, B, Zuo, G, Hoppmann, M. 2022h. Temperature and heating induced temperature difference measurements from SIMBA-type sea ice mass balance buoy 2019T47, deployed during MOSAiC 2019/20: 4 datasets. *PANGAEA*. DOI: http://dx.doi.org/10.1594/PANGAEA.940387.

Lei, R, Cheng, B, Zuo G, Hoppmann, M. 2022i. Temperature and heating induced temperature difference measurements from SIMBA-type sea ice mass balance buoy 2019T63, deployed during MOSAiC 2019/20: 4 datasets. *PANGAEA*. DOI: http://dx.doi.org/10.1594/PANGAEA.940593.

Lei, R, Cheng, B, Zuo, G, Hoppmann, M. 2022j. Temperature and heating induced temperature difference measurements from SIMBA-type sea ice mass balance buoy 2019T65, deployed during MOSAiC 2019/20: 4 datasets. PANGAEA. DOI: http://dx.doi.org/10.1594/PANGAEA.940634.

Lei, R, Hutchings, JK, Cheng, B, Hoppmann, M. 2022l. Temperature and heating induced temperature difference measurements from SIMBA-type sea ice mass balance buoy 2020T75, deployed during MOSAiC 2019/20: 4 datasets. PANGAEA. DOI: http://dx.doi.org/10.1594/PANGAEA.940740.

Lei, R, Hutchings, JK, Hoppmann, M, Yuan, Z. 2022m. Temperature and heating induced temperature difference measurements from SIMBA-type sea ice mass balance buoy 2020T79, deployed during MOSAiC 2019/20: 4 datasets. PANGAEA. DOI: http://dx.doi.org/10.1594/PANGAEA.940712.

Lei, R, Hutchings, JK, Watkins, D, Hoppmann, M. 2021a. Sea ice drift from autonomous measurements from buoy 2020P225, deployed during MOSAiC 2019/20. PANGAEA. DOI: http://dx.doi.org/10.1594/PANGAEA.939043.

Levy, M, Martin, AP. 2013. The influence of mesoscale and submesoscale heterogeneity on ocean biogeochemical reactions. *Global Biogeochemical Cycles* **27**(4): 1139–1150. DOI: http://dx.doi.org/10.1002/2012GB004518.

Li, G, Cheng, L, Zhu, J, Trenberth, KE, Mann, ME, Abraham, JP. 2020. Increasing ocean stratification over the past half-century. *Nature Climate Change* **10**(12): 1116–1123. DOI: http://dx.doi.org/10.1038/s41558-020-00918-2.

Li, T, Zhu, J, Zhai, L. 2021b. Drift Towing Ocean Profiler (DTOP) data on sea ice, meteorological conditions and drift of sea ice from buoy 2019V1, deployed during MOSAiC 2019/20: 2 datasets. *PANGAEA*. DOI: http://dx.doi.org/10.1594/PANGAEA.937212.

Li, T, Zhu, J, Zhai, L. 2021c. Drift Towing Ocean Profiler (DTOP) data on sea ice, meteorological conditions and drift of sea ice from buoy 2019V2, deployed during MOSAiC 2019/20: 2 datasets. *PANGAEA*. DOI: http://dx.doi.org/10.1594/PANGAEA.937940.

Li, T, Zhu, J, Zhai, L. 2021d. Drift Towing Ocean Profiler (DTOP) data on sea ice, meteorological conditions and drift of sea ice from buoy 2019V4, deployed during MOSAiC 2019/20: 2 datasets. *PANGAEA*. DOI: http://dx.doi.org/10.1594/PANGAEA.937949.

Li, T, Zhu, J, Zhai, L. 2021a. Ocean data of the Drift Towing Ocean Profiler (DTOP) data on sea ice, meteorological conditions and drift of sea ice from buoy 2019V5. *PANGAEA*. DOI: http://dx.doi.org/10.1594/PANGAEA.937955.

Light, B, Smith, MM, Perovich, DK, Webster, MA, Holland, MM, Linhardt, F, Raphael, IA, Clemens-Sewall, D, Macfarlane, AR, Anhaus, P, Bailey, DA. 2022. Arctic sea ice albedo: Spectral composition, spatial heterogeneity, and temporal evolution observed during the MOSAiC drift. *Elementa: Science of the Anthropocene* **10**(1): 000103. DOI: http://dx.doi.org/10.1525/elementa.2021.000103.

Lindsay, R, Schweiger, A. 2015. Arctic sea ice thickness loss determined using subsurface, aircraft, and satellite observations. *The Cryosphere* **9**(1): 269–283. DOI: http://dx.doi.org/10.5194/tc-9-269-2015.

Mahadevan, A. 2016. The impact of submesoscale physics on primary productivity of plankton. *Annual Review of Marine Science* **8**(1): 161–184. DOI: http://dx.doi.org/10.1146/annurev-marine-010814-015912.

Manucharyan, GE, Thompson, AF. 2017. Submesoscale sea ice-ocean interactions in marginal ice zones. *Journal of Geophysical Research: Oceans* **122**(12): 9455–9475. DOI: http://dx.doi.org/10.1002/2017JC012895.

Marsan, D, Stern, H, Lindsay, R, Weiss, J. 2004. Scale dependence and localization of the deformation of Arctic sea ice. *Physical Review Letters* **93**(17). DOI: http://dx.doi.org/10.1103/PhysRevLett.93.178501.

Maslowski, W, Clement Kinney, J, Higgins, M, Roberts, A. 2012. The future of Arctic sea ice. *Annual Review of Earth and Planetary Sciences* **40**(1): 625–654. DOI: http://dx.doi.org/10.1146/annurev-earth-042711-105345.

Maykut, GA, Untersteiner, N. 1971. Some results from a time-dependent thermodynamic model of sea ice. *Journal of Geophysical Research* **76**(6): 1550–1575. DOI: http://dx.doi.org/10.1029/JC076i006p01550.

Maykut, GA. 1978. Energy exchange over young sea ice in the central Arctic. *Journal of Geophysical Research* **83**(C7): 3646–3658. DOI: http://dx.doi.org/10.1029/JC083iC07p03646.

McDougall, TJ, Barker, PM. 2011. Getting started with TEOS-10 and the Gibbs Seawater (GSW) Oceanographic Toolbox. SCOR/IAPSO WG127.

McDougall, TJ, Feistel, R, Millero, F, Jackett, DR, Wright, D, King, B, Marion, G, Chen, CTA, Spitzer, P. 2010. The international thermodynamic equation of seawater – 2010:

calculation and use of thermodynamic properties. Paris: 196 S. *IOC Manuals and guides 56*. http://unesdoc.unesco.org/images/0018/001881/188170e.pdf.

McPhee, MG. 1978. A simulation of inertial oscillation in drifting pack ice. *Dynamics of Atmospheres and Oceans* **2**(2): 107–122. DOI: http://dx.doi.org/10.1016/0377-0265(78)90005-2.

Mortenson, E, Steiner, N, Monahan, AH, Hayashida, H, Sou, T, Shao, A. 2020. Modeled impacts of sea ice exchange processes on Arctic Ocean carbon uptake and acidification (1980–2015). *Journal of Geophysical Research: Oceans* **125**(7). DOI: http://dx.doi.org/10.1029/2019JC015782.

MOSAiC Consortium. 2016. MOSAiC Science Plan. Eprint ID 56333, https://epic.awi.de/id/eprint/56616/, last accessed June 30, 2023.

MOSAiC Consortium. 2018. MOSAiC Implementation Plan. Eprint ID 56333, https://epic.awi.de/id/eprint/56333/ , last accessed June 30, 2023.

NASA. 2023. NASA Goddard Space Flight Center, Ocean Ecology Laboratory, Ocean Biology Processing Group. Moderate-resolution Imaging Spectroradiometer (MODIS) Aqua Data; NASA OB.DAAC, Greenbelt, MD, USA. Accessed on January 01, 2018; see also https://oceancolor.gsfc.nasa.gov/.

Neckel, N, Fuchs, N, Birnbaum, G, Hutter, N, Jutila, A, Buth, L, von Albedyll, L, Ricker, R, Haas, C. 2023. Helicopter-borne RGB orthomosaics and photogrammetric digital elevation models from the MOSAiC Expedition. *Scientific Data* **10**(1): 426. DOI: http://dx.doi.org/10.1038/s41597-023-02318-5.

Nicolaus, M, Hoppmann, M, Arndt, S, Hendricks, S, Katlein, C, Nicolaus, A, Rossmann, L, Schiller, M, Schwegmann, S. 2021a. Snow depth and air temperature seasonality on sea ice derived from Snow Buoy measurements. *Frontiers in Marine Science* **8**: 655446. DOI: http://dx.doi.org/10.3389/fmars.2021.655446.

Nicolaus, M, Hoppmann, M, Lei, R, Belter, HJ, Fang, YC, Rohde, J. 2020a. Snow height on sea ice, meteorological conditions and drift of sea ice from autonomous measurements from buoy 2019S81, deployed during MOSAiC 2019/20. *PANGAEA*. DOI: http://dx.doi.org/10.1594/PANGAEA.925312.

Nicolaus, M, Hoppmann, M, Lei, R, Belter, HJ, Fang, YC, Rohde, J. 2020b. Snow height on sea ice, meteorological conditions and drift of sea ice from autonomous measurements from buoy 2019S94, deployed during MOSAiC 2019/20. *PANGAEA*. DOI: http://dx.doi.org/10.1594/PANGAEA.925325.

Nicolaus, M, Perovich, DK, Spreen, G, Granskog, MA, von Albedyll, L, Angelopoulos, M, Anhaus, P, Arndt, S, Belter, HJ, Bessonov, V, Birnbaum, G, Brauchle, J, Calmer, R, Cardellach, E, Cheng, B, Clemens-Sewall, D, Dadic, R, Damm, E, de Boer, G, Demir, O, Dethloff, K, Divine, DV, Fong, AA, Fons, S, Frey, MM, Fuchs, N, Gabarró, C, Gerland, S, Goessling, HF, Gradinger, R, Haapala, J, Haas, C, Hamilton, J, Hannula, HR, Hendricks, S, Herber, A, Heuzé, C, Hoppmann, M, Høyland, KV, Huntemann, M, Hutchings, JK, Hwang, B, Itkin, P, Jacobi, HW, Jaggi, M, Jutila, A, Kaleschke, L, Katlein, C, Kolabutin, N, Krampe, D, Kristensen, SS, Krumpen, T, Kurtz, N, Lampert, A, Lange, BA, Lei, R, Light, B, Linhardt, F, Liston, GE, Loose, B, Macfarlane, AR, Mahmud, M, Matero, IO, Maus, S, Morgenstern, A, Naderpour, R, Nandan, V, Niubom, A, Oggier, M, Oppelt, N, Pätzold, F, Perron, C, Petrovsky, T, Pirazzini, R, Polashenski, C, Rabe, B, Raphael, IA, Regnery, J, Rex, M, Ricker, R, Riemann-Campe, K, Rinke, A, Rohde, J, Salganik, E, Scharien, RK, Schiller, M, Schneebeli, M, Semmling, M, Shimanchuk, E, Shupe, MD, Smith, MM, Smolyanitsky, V, Sokolov, V, Stanton, T, Stroeve, J, Thielke, L, Timofeeva, A, Tonboe, RT, Tavri, A, Tsamados, M, Wagner, DN, Watkins, D, Webster, M, Wendisch, M. 2022. Overview of the MOSAiC expedition: snow and sea ice. *Elementa: Science of the Anthropocene* **10**(1): 000046. DOI: http://dx.doi.org/10.1525/elementa.2021.000046.

Nicolaus, M, Riemann-Campe, K, Bliss, A, Hutchings, JK, Granskog, MA, Haas, C, Hoppmann, M, Kanzow, T, Krishfield, RA, Lei, R, Rex, M, Tao, L, Rabe, B. 2021b. Drift trajectories of the main sites of the Distributed Network of MOSAiC 2019/2020: 15 datasets. *PANGAEA*. DOI: http://dx.doi.org/10.1594/PANGAEA.937204.

Nixdorf, U, Dethloff, K, Rex, M, Shupe, M, Sommerfeld, A, Perovich, DK, Nicolaus, M, Heuzé, C, Rabe, B, Loose, B, Damm, E, Gradinger, R, Fong, A, Maslowski, W, Rinke, A, Kwok, R, Spreen, G, Wendisch, M, Herber, A, Hirsekorn, M, Mohaupt, V, Frickenhaus, S, Immerz, A, Weiss-Tuider, K, König, B, Mengedoht, D, Regnery, J, Gerchow, P, Ransby, D, Krumpen, T, Morgenstern, A, Haas, C, Kanzow, T, Rack, FR, Saitzev, V, Sokolov, V, Makarov, A, Schwarze, S, Wunderlich, T, Wurr, K, Boetius, A. 2021. MOSAiC Extended Acknowledgement. *Zenodo*. DOI: http://dx.doi.org/10.5281/ZENODO.5179738.

Notz, D, Wettlaufer, JS, Worster, MG. 2005. A non-destructive method for measuring the salinity and solid fraction of growing sea ice in situ. *Journal of Glaciology* **51**(172): 159–166. DOI: http://dx.doi.org/10.3189/172756505781829548.

Nurser, AJG, Bacon, S. 2014. The Rossby radius in the Arctic Ocean. *Ocean Science* **10**(6): 967–975. DOI: http://dx.doi.org/10.5194/os-10-967-2014.

Oikkonen, A, Haapala, J, Lensu, M, Karvonen, J, Itkin, P. 2017. Small-scale sea ice deformation during N-ICE2015: From compact pack ice to marginal ice zone. *Journal of Geophysical Research: Oceans* **122**(6): 5105–5120. DOI: http://dx.doi.org/10.1002/2016JC012387.

Ocean University of China. 2024: Drift-Towing Ocean Profiler. http://coas.ouc.edu.cn/pogoc/2021/0713/c9714a342585/page.htm, last accessed on January 30, 2024.

Perovich, DK, Meier, W, Tschudi, M, Hendricks, S, Petty, AA, Divine, D, Farrell, S, Gerland, S, Haas, C, Kaleschke, L, Pavlova, O, Ricker, R, Tian-Kunze, X, Webster, M, Wood, K. 2020. Arctic Report Card 2020: Sea Ice. *Series: Arctic Report Card.* DOI: http://dx.doi.org/10.25923/N170-9H57.

Perovich, DK, Raphael, I, Moore, R, Clemens-Sewall, D, Lei, R, Sledd, A, Polashenski, C. 2023. Sea ice heat and mass balance measurements from four autonomous buoys during the MOSAiC drift campaign. *Elementa: Science of the Anthropocene* **11**(1): 00017. DOI: http://dx.doi.org/10.1525/elementa.2023.00017.

Perovich, DK, Richter-Menge, J, Polashenski, C, Elder, B, Arbetter, T, Brennick, O. 2014. Sea ice mass balance observations from the North Pole Environmental Observatory. *Geophysical Research Letters* **41**(6): 2019–2025. DOI: http://dx.doi.org/10.1002/2014GL059356.

Perovich, DK, Andreas, EL, Curry, JA, Eiken, H, Fairall, CW, Grenfell, TC, Guest, PS, Intrieri, J, Kadko, D, Lindsay, RW, McPhee, MG, Morison, J, Moritz, RE, Paulson, CA, Pegau, WS, Persson, POG, Pinkel, R, Richter-Menge, JA, Stanton, T, Stern, H, Sturm, M, Tucker, W B III, Uttal, T. 1999. Year on ice gives climate insights. *Eos Transactions* **80**(41): 481. DOI: http://dx.doi.org/10.1029/EO080i041p00481-01.

Perovich, DK, Elder, B. 2002. Estimates of ocean heat flux at SHEBA. *Geophysical Research Letters* **29**(9): 58-1-58–4. DOI: http://dx.doi.org/10.1029/2001GL014171.

Persson, POG, Fairall, CW, Andreas, EL, Guest, PS, Perovich, DK. 2002. Measurements near the Atmospheric Surface Flux Group tower at SHEBA: Near-surface conditions and surface energy budget. *Journal of Geophysical Research: Oceans* **107**(C10). DOI: http://dx.doi.org/10.1029/2000JC000705.

Persson, POG, Shupe, MD, Perovich, D, Solomon, A. 2017. Linking atmospheric synoptic transport, cloud phase, surface energy fluxes, and sea-ice growth: observations of midwinter SHEBA conditions. *Climate Dynamics* **49**(4): 1341–1364. DOI: http://dx.doi.org/10.1007/s00382-016-3383-1.

Persson, POG. 2012. Onset and end of the summer melt season over sea ice: thermal structure and surface energy perspective from SHEBA. *Climate Dynamics* **39**(6): 1349–1371. DOI: http://dx.doi.org/10.1007/s00382-011-1196-9.

Pithan, F, Athanase, M, Dahlke, S, Sánchez-Benítez, A, Shupe, MD, Sledd, A, Streffing, J, Svensson, G, Jung, T. 2023. Nudging allows direct evaluation of coupled climate models with in situ observations: a case study from the MOSAiC expedition. *Geoscientific Model Development* **16**(7): 1857–1873. DOI: http://dx.doi.org/10.5194/gmd-16-1857-2023.

Planck, CJ, Whitlock, J, Polashenski, C, Perovich, DK. 2019. The evolution of the seasonal ice mass balance buoy. *Cold Regions Science and Technology* **165**: 102792. DOI: http://dx.doi.org/10.1016/j.coldregions.2019.102792.

Polyakov, GV, Pnyushkov, AV, Alkire, M B, Ashik, IM, Baumann, TM, Carmack, EC, Goszczko, I, Guthrie, J, Ivanov, VV, Kanzow, T, Krishfield, R, Kwok, R, Sundfjord, A, Morison, J, Rember, R, Yulin, A. 2017. Greater role for Atlantic inflows on sea-ice loss in the Eurasian Basin of the Arctic Ocean. *Science* **356**(6335): 285–291. DOI: http://dx.doi.org/10.1126/science.aai8204.

Rabe, B, Heuzé, C, Regnery, J, Aksenov, Y, Allerholt, J, Athanase, M, Bai, Y, Basque, C, Bauch, D, Baumann, TM, Chen, D, Cole, ST, Craw, L, Davies, A, Damm, E, Dethloff, K, Divine, DV, Doglioni, F, Ebert, F, Fang, YC, Fer, I, Fong, AA, Gradinger, R, Granskog, MA, Graupner, R, Haas, C, He, H, He, Y, Hoppmann, M, Janout, M, Kadko, D, Kanzow, T, Karam, S, Kawaguchi, Y, Koenig, Z, Kong, B, Krishfield, RA, Krumpen, T, Kuhlmey, D, Kuznetsov, I, Lan, M, Laukert, G, Lei, R, Li, T, Torres-Valdés, S, Lin, L, Lin, L, Liu, H, Liu, N, Loose, B, Ma, X, McKay, R, Mallet, M, Mallett, RDC, Maslowski, W, Mertens, C, Mohrholz, V, Muilwijk, M, Nicolaus, M, O'Brien, JK, Perovich, DK, Ren, J, Rex, M, Ribeiro, N, Rinke, A, Schaffer, J, Schuffenhauer, I, Schulz, K, Shupe, MD, Shaw, W, Sokolov, V, Sommerfeld, A, Spreen, G, Stanton, T, Stephens, M, Su, J, Sukhikh, N, Sundfjord, A, Thomisch, K, Tippenhauer, S, Toole, JM, Vredenborg, M, Walter, M, Wang, H, Wang, L, Wang, Y, Wendisch, M, Zhao, J, Zhou, M, Zhu, J. 2022. Overview of the MOSAiC expedition: Physical oceanography. *Elementa: Science of the Anthropocene* **10**(1): 00062. DOI: http://dx.doi.org/10.1525/elementa.2021.00062.

Rabe, B, Karcher, M, Schauer, U, Toole, J, Krishfield, R, Pisarev, S, Kauker, F, Gerdes, R, Kikuchi, T. 2011. An assessment of Arctic Ocean freshwater content changes from the 1990s to 2006–2008. *Deep-Sea Research Part I: Oceanographic Research Papers* **58**(2): 173–185. DOI: http://dx.doi.org/10.1016/j.dsr.2010.12.002.

Rackow, T, Sein, DV, Semmler, T, Danilov, S, Koldunov, NV, Sidorenko, D, Wang, Q, Jung, T. 2019. Sensitivity of deep ocean biases to horizontal resolution in prototype CMIP6 simulations with AWI-CM1.0. *Geoscientific Model Development* **12**(7): 2635–2656. DOI: http://dx.doi.org/10.5194/gmd-12-2635-2019.

Rantanen, M, Karpechko, AY, Lipponen, A, Nordling, K, Hyvärinen, O, Ruosteenoja, K, Vihma, T, Laaksonen, A. 2022. The Arctic has warmed nearly four times faster than the globe since 1979. *Communications Earth and Environment* **3**(1): 168. DOI: http://dx.doi.org/10.1038/s43247-022-00498-3.

Rennermalm, AK, Wood, EF, Weaver, AJ, Eby, M, Déry, SJ. 2007. Relative sensitivity of the Atlantic meridional overturning circulation to river discharge into Hudson Bay and the Arctic Ocean. *Journal of Geophysical Research: Biogeosciences* **112**(G4). DOI: http://dx.doi.org/10.1029/2006JG000330.

Rex, M. 2020. Links to master tracks in different resolutions of POLARSTERN cruise PS122/1, Tromsø – Arctic Ocean, 2019-09-20 – 2019-12-13 (Version 2). *PANGAEA*. DOI: http://dx.doi.org/10.1594/PANGAEA.924668

Rex, M. 2021a. Master tracks in different resolutions of POLARSTERN cruise PS122/4, Longyearbyen – Arctic Ocean, 2020-06-04 – 2020-08-12. *PANGAEA*. DOI: http://dx.doi.org/10.1594/PANGAEA.926829

Rex, M. 2021b. Master tracks in different resolutions of POLARSTERN cruise PS122/5, Arctic Ocean – Bremerhaven, 2020-08-12 – 2020-10-12. *PANGAEA*. DOI: http://dx.doi.org/10.1594/PANGAEA.926910

Richter-Menge, JA, Perovich, DK, Elder, BC, Claffey, K, Rigor, I, Ortmeyer, M. 2006. Ice mass-balance buoys: a tool for measuring and attributing changes in the thickness of the Arctic sea-ice cover. *Annals of Glaciology* **44**: 205–210. DOI: http://dx.doi.org/10.3189/172756406781811727.

Rigor, I, Ortmeyer, M. 2001. International Arctic Buoy Program 2001 Data Report, APL-UW TM 6-02, Applied Physics Laboratory, University of Washington, 2002. https://iabp.apl.uw.edu/Data_Products/Reports/tm_6_02.pdf, last accessed on February 2, 2024

Rippeth, T, Fine, E. 2022. Turbulent mixing in a changing Arctic Ocean. *Oceanography* **35**(3–4): 66–75. DOI: http://dx.doi.org/10.5670/oceanog.2022.103.

Roberts, AF, Hunke, EC, Kamal, SM, Lipscomb, WH, Horvat, C, Maslowski, W. 2019. A variational method for sea ice ridging in Earth system models. *Journal of Advances in Modeling Earth Systems* **11**(3): 771–805. DOI: http://dx.doi.org/10.1029/2018MS001395.

Rudels, B. 2009. Arctic Ocean Circulation. In: Steele, E-CJH, Turekian, KK, Thorpe, SA, editors. *Encyclopedia of Ocean Sciences (Second Edition).* Oxford: Academic Press. P. 211–225. DOI: http://dx.doi.org/10.1016/B978-012374473-9.00601-9.

Salganik, E, Katlein, C, Lange, BA, Matero, I, Lei, R, Fong, AA, Fons, SW, Divine, D, Oggier, M, Castellani, G, Bozzato, D, Chamberlain, EJ, Hoppe, CJM, Müller, O, Gardner, J, Rinke, A, Simões Pereira, PS, Ulfsbo, A, Marsay, C, Webster, MA, Maus, S, Høyland, K, Granskog, MA. 2023. Temporal evolution of under-ice meltwater layers and false bottoms and their impact on summer Arctic sea ice mass balance. *Elementa: Science of the Anthropocene* **11**(1): 00035. DOI: http://dx.doi.org/10.1525/elementa.2022.00035.

Schartmüller, B, Anderson, P, McKee, D, Connan-McGinty, S, Kopec, TP, Daase, M, Johnsen, G, Berge J. 2023. Development and calibration of a high dynamic range and autonomous ocean-light instrument to measure sub-surface profiles in ice-covered waters. *Applied Optics* **62**: 8308. DOI: http://dx.doi.org/10.1364/ao.502437.

Schulz, K, Koenig, Z, Muilwijk, M, Bauch, D, Hoppe, CJM, Droste, E, Hoppmann, M, Chamberlain, EJ, Laukert, G, Stanton, T, Quintanilla Zurita, A, Fer, I, Heuzé, C, Karam, S, Mieruch-Schnuelle, S, Baumann, T, Vredenborg, M, Tippenhauer, S, Granskog, MA. n.d. The Eurasian Arctic Ocean along the MOSAiC drift (2019–2020): An interdisciplinary perspective on properties and processes. *Elementa: Science of the Anthropocene* (submitted). Preprint at DOI: http://dx.doi.org/10.31223/X5TT2W.

Schulz, K, Mohrholz, V, Fer, I, Janout, M, Hoppmann, M, Schaffer, J, Koenig, Z. 2022. A full year of turbulence measurements from a drift campaign in the Arctic Ocean 2019–2020. *Scientific Data* **9**(1): 472. DOI: http://dx.doi.org/10.1038/s41597-022-01574-1.

Sein, DV, Koldunov, NV, Danilov, S, Wang, Q, Sidorenko, D, Fast, I, Rackow, T, Cabos, W, Jung, T. 2017. Ocean modeling on a mesh with resolution following the local Rossby radius. *Journal of Advances in Modeling Earth Systems* **9**(7): 2601–2614. DOI: http://dx.doi.org/10.1002/2017MS001099.

Shaw, WJ, Stanton, TP, McPhee, MG, Kikuchi, T. 2008. Estimates of surface roughness length in heterogeneous under-ice boundary layers. *Journal of Geophysical Research: Oceans* **113**(C8): C08030. DOI: http://dx.doi.org/10.1029/2007JC004550.

Shaw, WJ, Stanton, TP, McPhee, MG, Morison, JH, Martinson, DG. 2009. Role of the upper ocean in the energy budget of Arctic sea ice during SHEBA. *Journal of Geophysical Research: Oceans* **114**(C6): C06012. DOI: http://dx.doi.org/10.1029/2008JC004991.

Sherr, EB, Sherr, BF, Wheeler, PA, Thompson, K. 2003. Temporal and spatial variation in stocks of autotrophic and heterotrophic microbes in the upper water column of the central Arctic

Ocean. *Deep Sea Research Part I: Oceanographic Research Papers* **50**(5): 557–571. DOI: http://dx.doi.org/10.1016/S0967-0637(03)00031-1.

Shibley, NC, Timmermans, ML, Carpenter, JR, Toole, JM. 2017. Spatial variability of the Arctic Ocean's double-diffusive staircase. *Journal of Geophysical Research: Oceans* **122**(2): 980–994. DOI: http://dx.doi.org/10.1002/2016JC012419.

Shupe, MD, Rex, M, Blomquist, B, Persson, POG, Schmale, J, Uttal, T, Althausen, D, Angot, H, Archer, S, Bariteau, L, Beck, I, Bilberry, J, Bucci, S, Buck, C, Boyer, M, Brasseur, Z, Brooks, IM, Calmer, R, Cassano, J, Castro, V, Chu, D, Costa, D, Cox, CJ, Creamean, J, Crewell, S, Dahlke, S, Damm, E, de Boer, G, Deckelmann, H, Dethloff, K, Dütsch, M, Ebell, K, Ehrlich, A, Ellis, J, Engelmann, R, Fong, AA, Frey, MM, Gallagher, MR, Ganzeveld, L, Gradinger, R, Graeser, J, Greenamyer, V, Griesche, H, Griffiths, S, Hamilton, J, Heinemann, G, Helmig, D, Herber, A, Heuzé, C, Hofer, J, Houchens, T, Howard, D, Inoue, J, Jacobi, HW, Jaiser, R, Jokinen, T, Jourdan, O, Jozef, G, King, W, Kirchgaessner, A, Klingebiel, M, Krassovski, M, Krumpen, T, Lampert, A, Landing, W, Laurila, T, Lawrence, D, Lonardi, M, Loose, B, Lüpkes, C, Maahn, M, Macke, A, Maslowski, W, Marsay, C, Maturilli, M, Mech, M, Morris, S, Moser, M, Nicolaus, M, Ortega, P, Osborn, J, Pätzold, F, Perovich, DK, Petäjä, T, Pilz, C, Pirazzini, R, Posman, K, Powers, H, Pratt, KA, Preußer, A, Quéléver, L, Radenz, M, Rabe, B, Rinke, A, Sachs, T, Schulz, A, Siebert, H, Silva, T, Solomon, A, Sommerfeld, A, Spreen, G, Stephens, M, Stohl, A, Svensson, G, Uin, J, Viegas, J, Voigt, C, von der Gathen, P, Wehner, B, Welker, JM, Wendisch, M, Werner, M, Xie, ZQ, Yue, F. 2022. Overview of the MOSAiC expedition: Atmosphere. *Elementa: Science of the Anthropocene* **10**(1): 00060. DOI: http://dx.doi.org/10.1525/elementa.2021.00060.

Shupe, MD, Rex, M, Dethloff, K, Damm, E, Fong, AA, Gradinger, R, Heuzé, C, Loose, B, Makarov, A, Maslowski, W, Nicolaus, M, Perovich, D, Rabe, B, Rinke, A, Sokolov, V, Sommerfeld, A, 2020. The MOSAiC Expedition: A Year Drifting with the Arctic Sea Ice. *Series: Arctic Report Card*. DOI: http://dx.doi.org/10.25923/9G3V-XH92.

Sirevaag, A, De La Rosa, S, Fer, I, Nicolaus, M, Tjernström, M, McPhee, MG. 2011. Mixing, heat fluxes and heat content evolution of the Arctic Ocean mixed layer. *Ocean Science* **7**(3): 335–349. DOI: http://dx.doi.org/10.5194/os-7-335-2011.

Solomon, A, Shupe, MD, Svensson, G, Barton, NP, Batrak, Y, Bazile, E, Day, JJ, Doyle, JD, Frank, HP, Keeley, S, Remes, T, Tolstykh, M. 2023. The winter central Arctic surface energy budget: A model evaluation using observations from the MOSAiC campaign.

Elementa: Science of the Anthropocene **11**(1): 00104. DOI: http://dx.doi.org/10.1525/elementa.2022.00104.

Sperzel, TR, Jäkel, E, Pätzold, F, Lampert, A, Niehaus, H, Spreen, G, Rosenburg, S, Birnbaum, G, Neckel, N, Wendisch, M. 2023. Surface albedo measurements and surface type classification from helicopter-based observations during MOSAiC. *Scientific Data* **10**(1): 584. DOI: http://dx.doi.org/10.1038/s41597-023-02492-6.

Spreen, G, Kwok, R, Menemenlis, D, Nguyen, AT. 2017. Sea-ice deformation in a coupled ocean–sea-ice model and in satellite remote sensing data. *The Cryosphere* **11**(4): 1553–1573. DOI: http://dx.doi.org/10.5194/tc-11-1553-2017.

Stanton, TP, Shaw, WJ, Hutchings, JK. 2012. Observational study of relationships between incoming radiation, open water fraction, and ocean-to-ice heat flux in the Transpolar Drift: 2002–2010. *Journal of Geophysical Research: Oceans* **117**(C7). DOI: http://dx.doi.org/10.1029/2011JC007871.

Stanton, TP, Shaw, WJ. 2023a. Observations from Autonomous Ocean Flux Buoy 43 deployed at site L1 during the MOSAiC transpolar drift, Arctic Basin, 2019–2020. *NSF Arctic Data Center*. DOI: http://dx.doi.org/10.18739/A2610VT5W

Stanton, TP, Shaw, WJ. 2023b. Observations from Autonomous Ocean Flux Buoy 44 deployed at site L2 during the MOSAiC transpolar drift, Arctic Basin, 2019–2020. *NSF Arctic Data Center*. DOI: http://dx.doi.org/10.18739/A2P26Q527

Stanton, TP, Shaw, WJ. 2023c. Observations from Autonomous Ocean Flux Buoy 45 deployed at site L3 during the MOSAiC transpolar drift, Arctic Basin, 2019–2020. *NSF Arctic Data Center*. DOI: http://dx.doi.org/10.18739/A2XG9FC60

Stanton, TP, Shaw, WJ. 2023d. Observations from Autonomous Ocean Flux Buoy 46 deployed at site CO during the MOSAiC transpolar drift, Arctic Basin, 2019–2020. *NSF Arctic Data Center*. DOI: http://dx.doi.org/10.18739/A2SQ8QK2V

Steele, M, Morley, R, Ermold, W. 2001. PHC: A global ocean hydrography with a high-quality Arctic Ocean. *Journal of Climate* **14**(9): 2079–2087. DOI: http://dx.doi.org/10.1175/1520-0442(2001)014<2079:PAGOHW>2.0.CO;2.

Stefan, J. 1891. Ueber die Theorie der Eisbildung, insbesondere über die Eisbildung im Polarmeere. *Annalen der Physik* **278**: 269–286.

Stramler, K, Del Genio, AD, Rossow, WB. 2011. Synoptically driven Arctic winter states. *Journal of Climate* **24**(6): 1747–1762. DOI: http://dx.doi.org/10.1175/2010JCLI3817.1 .

Strobach, E, Bel, G. 2017. The contribution of internal and model variabilities to the uncertainty in CMIP5 decadal climate predictions. *Climate Dynamics* **49**(9–10): 3221–3235. DOI: http://dx.doi.org/10.1007/s00382-016-3507-7.

SWITCHYARD. 2023: http://psc.apl.washington.edu/switchyard/, last accessed June 30, 2023.

Tao, R, Nicolaus, M, Katlein, C Anhaus, P Hoppmann, M Spreen, G Niehaus, H, Jäkel, E, Wendisch, M, Haas, C. n.D. Seasonality of spectral radiative fluxes and optical properties of Arctic sea ice. *Elementa: Science of the Anthropocene* (submitted).

Timmermans, ML, Cole, S, Toole, J. 2012. Horizontal density structure and restratification of the Arctic Ocean surface layer. *Journal of Physical Oceanography* **42**(4): 659–668. DOI: http://dx.doi.org/10.1175/JPO-D-11-0125.1.

Tjernström, M, Leck, C, Birch, CE, Bottenheim, JW, Brooks, BJ, Brooks, IM, Bäcklin, L, Chang, RYW, de Leeuw, G, Di Liberto, L, de la Rosa, S, Granath, E, Graus, M, Hansel, A, Heintzenberg, J, Held, A, Hind, A, Johnston, P, Knulst, J, Martin, M, Matrai, PA, Mauritsen, T, Müller, M, Norris, SJ, Orellana, MV, Orsini, DA, Paatero, J, Persson, POG, Gao, Q, Rauschenberg, C, Ristovski, Z, Sedlar, J, Shupe, MD, Sierau, B, Sirevaag, A, Sjogren, S, Stetzer, O, Swietlicki, E, Szczodrak, M, Vaattovaara, P, Wahlberg, N, Westberg, M, Wheeler, CR. 2014. The Arctic Summer Cloud Ocean Study (ASCOS): overview and experimental design. *Atmospheric Chemistry and Physics* **14**(6): 2823–2869. DOI: http://dx.doi.org/10.5194/acp-14-2823-2014.

Toole, JM, Krishfield, R, Timmermans, ML, Proshutinsky, A. 2011. The Ice-Tethered Profiler: Argo of the Arctic. *Oceanography* **24**(3): 126–135. DOI: http://dx.doi.org/10.5670/oceanog.2011.64.

Toole, JM, Krishfield, RA, O'Brien, JK, Houk, AE, Cole, ST, Woods Hole Oceanographic Institution Ice-Tethered Profiler Program. 2016. Ice-Tethered Profiler observations: Vertical profiles of temperature, salinity, oxygen, and ocean velocity from an Ice-Tethered Profiler buoy system. Dataset. *NOAA National Centers for Environmental Information*. Last accessed January 30, 2024. DOI: http://dx.doi.org/10.7289/V5MW2F7X.

Toole, JM, Timmermans, ML, Perovich, DK, Krishfield, RA, Proshutinsky, A, Richter-Menge, JA. 2010. Influences of the ocean surface mixed layer and thermohaline stratification on Arctic sea ice in the central Canada Basin. *Journal of Geophysical Research: Oceans* **115**(C10): 2009JC005660. DOI: http://dx.doi.org/10.1029/2009JC005660.

University of Washington. 2024: Measuring the Upper layer Temperature of the Polar Oceans. http://psc.apl.washington.edu/UpTempO/UpTempO.php, last accessed on February 7, 2024.

Untersteiner, N, Thorndike, AS, Rothrock, DA, Hunkins, KL. 2009. AIDJEX revisited: A look back at the U.S.-Canadian Arctic Ice Dynamics Joint Experiment 1970–78. *Arctic* **60**(3): 327–336. DOI: http://dx.doi.org/10.14430/arctic233.

von Albedyll, L, Hendricks, S, Grodofzig, R, Krumpen, T, Arndt, S, Belter, HJ, Birnbaum, G, Cheng, B, Hoppmann, M, Hutchings, JK, Itkin, P, Lei, R, Nicolaus, M, Ricker, R, Rohde, J, Suhrhoff, M, Timofeeva, A, Watkins, D, Webster, M, Haas, C. 2022. Thermodynamic and dynamic contributions to seasonal Arctic sea ice thickness distributions from airborne observations. *Elementa: Science of the Anthropocene* **10**(1): 00074. DOI: http://dx.doi.org/10.1525/elementa.2021.00074.

von Appen, WJ, Baumann, T, Janout, M, Koldunov, N, Lenn, YD, Pickart, R, Scott, R, Wang, Q. 2022. Eddies and the distribution of eddy kinetic energy in the Arctic Ocean. *Oceanography* **35**(3–4): 42–51. DOI: http://dx.doi.org/10.5670/oceanog.2022.122.

Wang, Q, Koldunov, NV, Danilov, S, Sidorenko, D, Wekerle, C, Scholz, P, Bashmachnikov, IL, Jung, T. 2020. Eddy kinetic energy in the Arctic Ocean from a global simulation with a 1-km Arctic. *Geophysical Research Letters* **47**(14). DOI: http://dx.doi.org/10.1029/2020GL088550.

Watkins, DM. 2023b. Relative motion of the buoys in the MOSAiC Distributed Network from 2019-12-20 to 2020-01-19. *Zenodo*. DOI: http://dx.doi.org/10.5281/ZENODO.10278327.

Watkins, DN, Persson, OPG, Hutchings, JK, Stanton, TP, Solomons, A. 2023c. Sea Ice and Ocean Response to a Strong Mid-Winter Cyclone in the Arctic Ocean. Abstract C41C-1534 presented at *AGU23*, San Francisco, CA, December 11–15, 2023. DOI: http://dx.doi.org/10.22541/essoar.170365235.53452562/v1.

Watkins, DM, Bliss, AC, Hutchings, JK, Wilhelmus, MM. 2023a. Evidence of abrupt transitions between sea ice dynamical regimes in the East Greenland marginal ice zone. *Geophysical Research Letters* **50**: 2023GL103558. DOI: http://dx.doi.org/10.1029/2023GL103558.

Webster, MA, Holland, M, Wright, NC, Hendricks, S, Hutter, N, Itkin, P, Light, B, Linhardt, F, Perovich, DK, Raphael, IA, Smith, MM, von Albedyll, L, Zhang, J. 2022. Spatiotemporal evolution of melt ponds on Arctic sea ice. *Elementa: Science of the Anthropocene* **10**(1): 000072. DOI: http://dx.doi.org/10.1525/elementa.2021.000072.

Wedi, NP, Polichtchouk, I, Dueben, P, Anantharaj, VG, Bauer, P, Boussetta, S, Browne, P, Deconinck, W, Gaudin, W, Hadade, I, Hatfield, S, Iffrig, O, Lopez, P, Maciel, P, Mueller, A, Saarinen, S, Sandu, I, Quintino, T, Vitart, F. 2020. A baseline for global weather and climate simulations at 1 km resolution. *Journal of Advances in Modeling Earth Systems* **12**(11). DOI: http://dx.doi.org/10.1029/2020MS002192.

Weingartner, T, Ashjian, C, Brigham, L, Haine, T, Mack, L, Perovich, D, Rabe, B. 2022. Introduction to the Special Issue on the New Arctic Ocean. *Oceanography* **35**(3–4): 6–9. DOI: http://dx.doi.org/10.5670/oceanog.2022.132

Wu, B, Handorf, D, Dethloff, K, Rinke, A, Hu, A. 2013. Winter weather patterns over Northern Eurasia and Arctic sea ice loss. *Monthly Weather Review* **141**(11): 3786–3800. DOI: http://dx.doi.org/10.1175/MWR-D-13-00046.1.

Figures and full captions

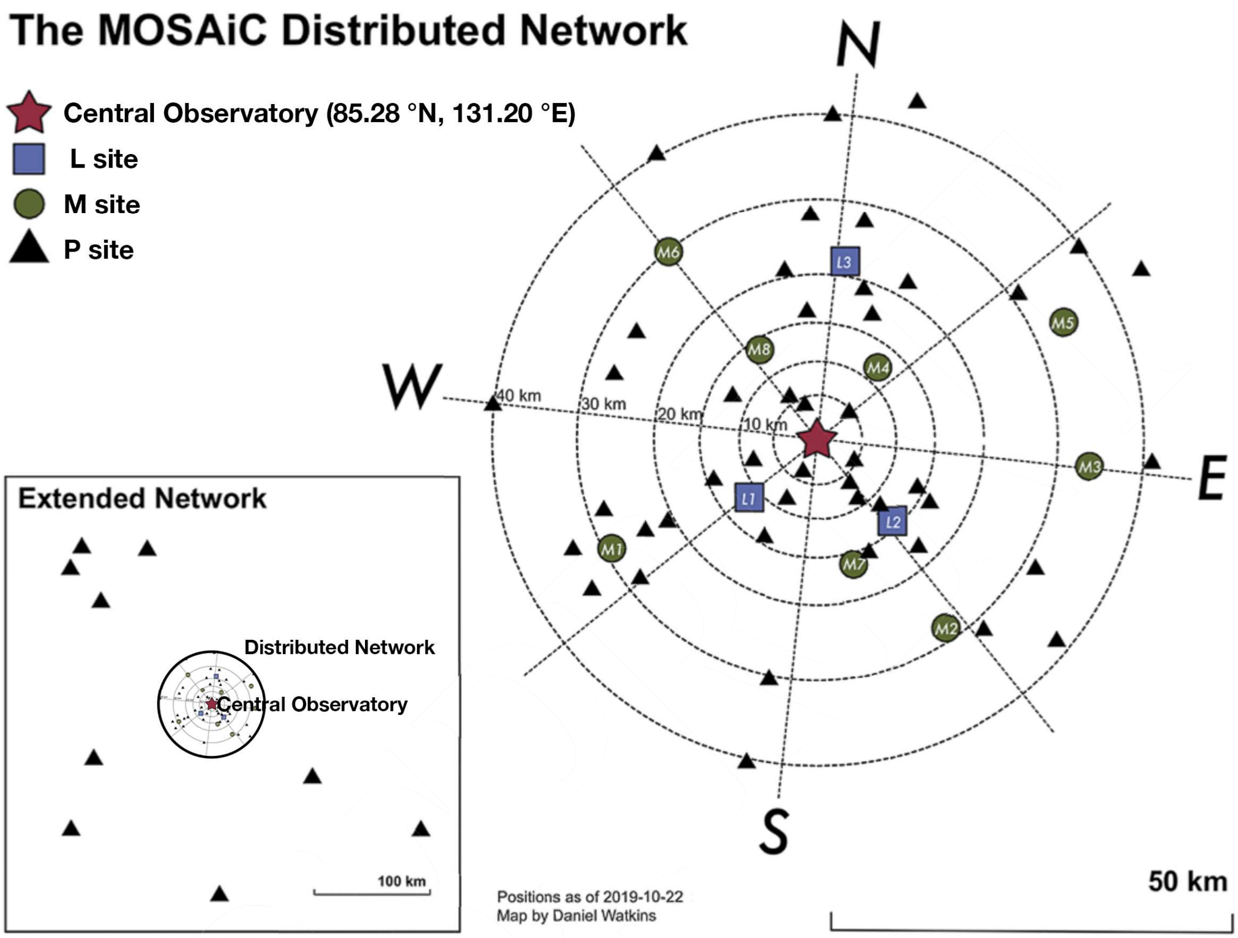

Figure 1. Actual layout of the Distributed Network after completing all initial deployments on October 22, 2019.

The different site types are distinguished by color as shown in the legend: L sites (blue squares), M sites (green circles) and P sites (black triangles). The Central Observatory with RV *Polarstern* is located in the center of the map (red star). Note that the LM site (not shown) was part of the wider Central Observatory, located 1–2 km away from RV *Polarstern*. The figure is modified from Krumpen and Sokolov (2020, their Figure 1.2).

Figure 2. Photographs of selected autonomous platforms (buoys) deployed in the two implementations of the Distributed Network.

a) Atmospheric Surface Flux Station (ASFS #50 at L3 (photo by Ola Persson); b) radiation station 2020R21 and thermistor string buoy 2020T81 deployed on a frozen melt pond (RITBOB; photo by Mario Hoppmann); c) Snow Buoy 2020S109 (Snow Buoy; photo by Mario Hoppmann); d) Unmanned (uncrewed) Ice Station (UMIS; photo by unknown); e) Seasonal Ice Mass Balance buoy (SIMB3; photo by unknown); f) Snow Ice Mass Balance Apparatus (SIMBA; photo by Mario

Hoppmann); g) Acoustic Zooplankton and Fish Profiler (AZFP) buoy and bio-optical buoy 2020M23 (IMBflex), with ablation stakes in the background (photo by Mario Hoppmann); h) First Institute of Oceanography Fixed-Level Ocean buoy (FIO FLB; photo by Bing Kong); i) Drift-Towing Ocean Profiler (D-TOP; photo by Mario Hoppmann); j) Woods-Hole Ice-Tethered Profiler (WHOI ITP; photo by unknown); k) position-tracking buoy 2020P162 (ice tracker; photo by Marcel Nicolaus); l) Salinity Ice Tether buoy (SIT; photo by Mario Hoppmann); m) Autonomous Ocean Flux Buoy (AOFB; photo by Michael Gallagher); n) light strings (OptiCAL, formerly Envipope; photo by Dmitry Divine); o) ice-Surface Velocity Profiler 2020P237 (iSVP; photo by Mario Hoppmann). Details of the different platform types are summarized in Tables 1 and S1.

Figure 3. Photographs of conditions during recovery of the Distributed Network platforms in 2020.

a) Atmospheric Surface Flux Station #50 turned upside down after ridging event at site L3 on February 4, requiring maintenance and reinstallation at the Central Observatory (photo by Michael Gallagher); b) surface unit and floatation of Woods Hole Ice-tethered Profiler #102 (2019W3) at site L3 during recovery in August: the tether had been severed so that the corresponding profiler could not be recovered as the tether had been severed (photo by Julia Regnery); c) Snow Buoy during recovery by “mummy chair” from the ship (photo by Julia Regnery).

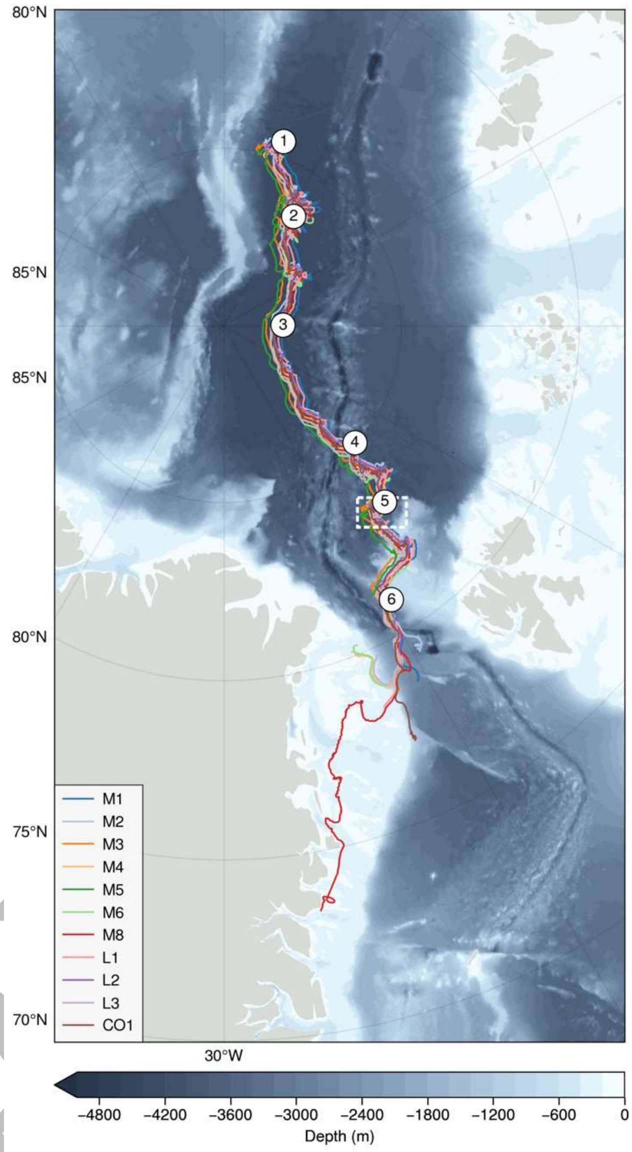

Figure 4. Drift tracks of the main sites of the Distributed Network.

Tracks of the 3 L sites and 8 M sites and the Central Observatory (CO1). Table S3 lists all data sources and their properties used to create the drift tracks, with further explanation given in Text S3. Drift track data are available from Nicolaus et al. (2021b). Note that the LM site (not shown) was part of the wider Central Observatory and very close to RV *Polarstern*, within 1–2 km when the ship was present. The numbers 1 to 6 on the track refer to the location of the maps in Figure 5, with Figure 1 located close to number 1. That part of the drift track where RV *Polarstern* was absent from the Central Observatory is marked by the white, dashed box, between about 82.4°N and 83.4°N. The seafloor topography and coastlines are based on the General Bathymetric Chart of the Oceans (GEBCO, 2020).

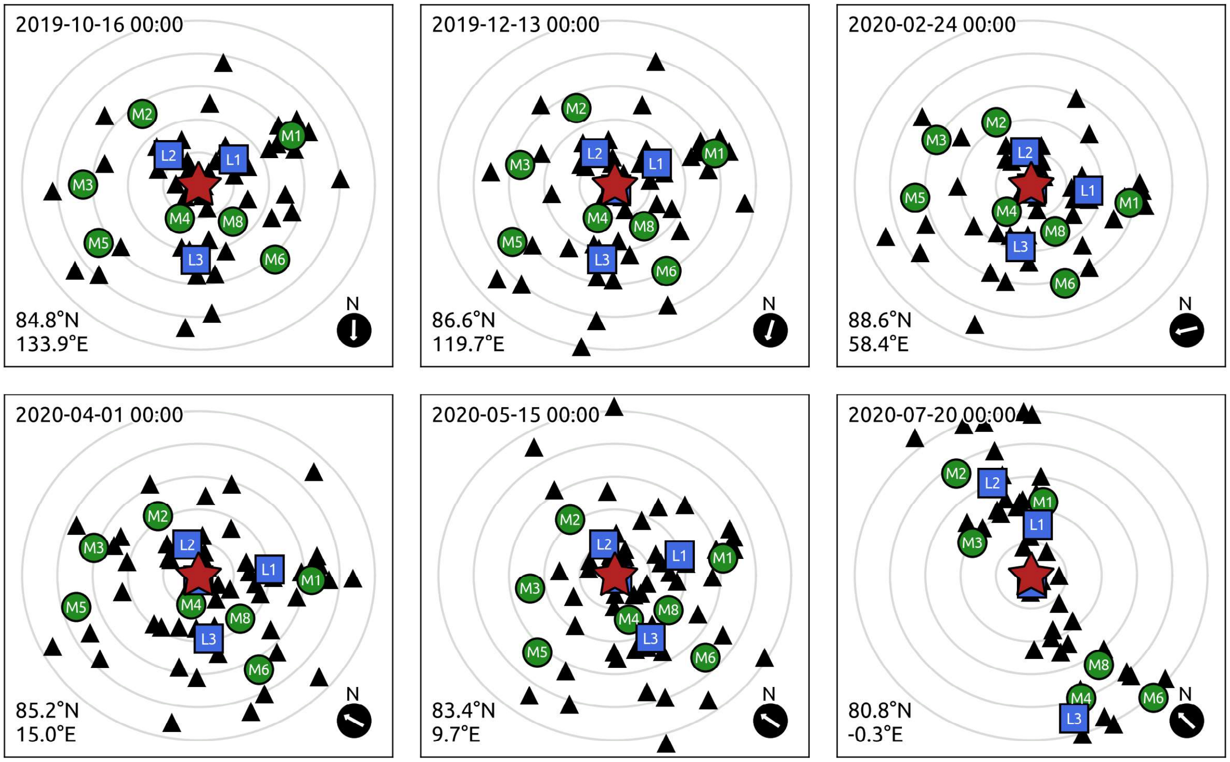

Figure 5. Evolution of the Distributed Network from mid-October 2019 to late July 2020. Position of the Distributed Network sites at six times during the drift in the transpolar drift, as marked in Figure 4. This set of maps documents the array after deployment, in late spring and towards the end of the drift as the array approached Fram Strait. Positions are shown in north polar stereographic projection; arrows in the lower right corners of each panel point north, and the position of the Central Observatory is shown in latitude/longitude in the lower left corner. Gray circles are plotted at 10 km intervals from the Central Observatory. The symbols refer to the Central Observatory, including the site LM (red star), the M sites (blue squares), the L sites (green circles) and the P sites (black triangles; see also Figure 1).

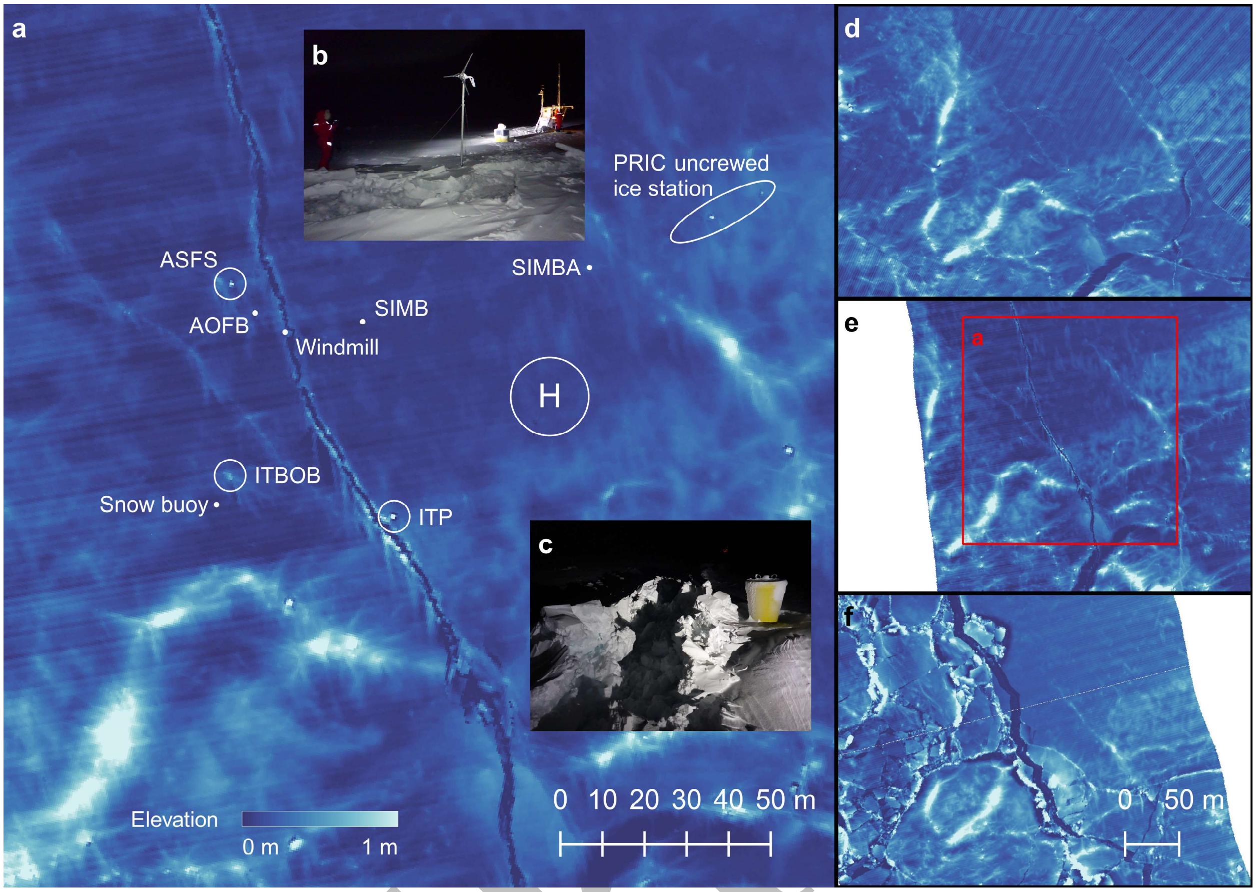

Figure 6. Surface elevation maps of site L3 in mid-winter from airborne laser scanner observations.

Shades of blue denote the approximate surface elevation according to the color bar, where the lightest blue indicates heights of 1 m and above. The large map in panel a shows the situation on January 25, 2020, where buoy locations are labeled. The combined radiation station and ice mass balance buoy (IMB) is labelled “ITBOB”. “H” marks the usual landing site for the helicopter. Photos b and c taken on January 20 show selected buoys and the developing crack in the ice (photos by Eric Brossier). The evolution throughout about one month is shown in panels d–f without annotations: d) January 8, e) January 25 and f) February 9. The red square in panel e shows the extent of panel a. The large crack from bottom right to top left is visible as a ragged dark-blue line after January 25. The Autonomous Ocean Flux Buoy (AOFB), Atmospheric Surface Flux Station (ASFS) and Woods Hole Ice-tethered Profiler (ITP) were subsequently damaged or disappeared as the crack developed into a pressure ridge (see also Figure 3a). Note the different horizontal scales in panel a and in panels d–f. The maps are based on data in Hutter et al. (2023a) and processed according to Hutter et al. (2023b).

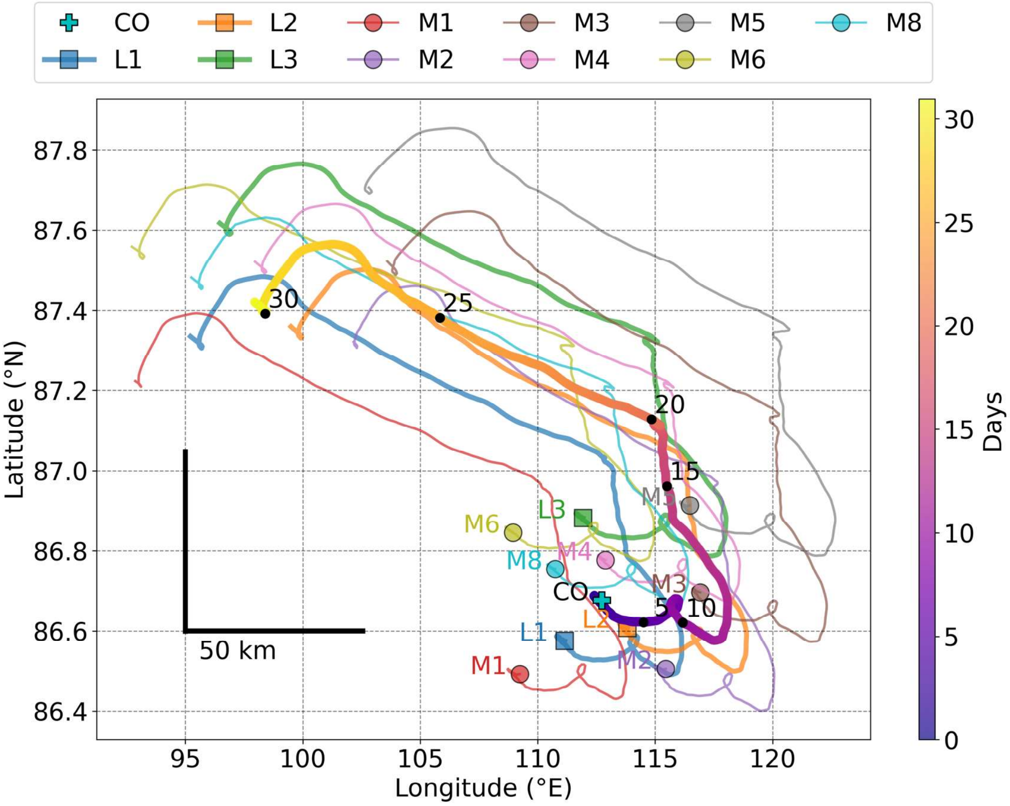

Figure 7. Geographic position of sites within the Distributed Network from late December to late January.

The black lines show the scale of horizontal distance in kilometers. The legend denotes the different sites with symbols corresponding to the position on December 20, 2019, and color to the lines of each site. Note that the P site tracks are omitted for clarity. CO is the position of the Central Observatory with RV *Polarstern*, with the 30-day time period shown in days from 20 December, 2019 (both in color and labelled every 5 days). The data for the M sites are from Salinity Ice Tether buoys (Hoppmann et al., 2022b).

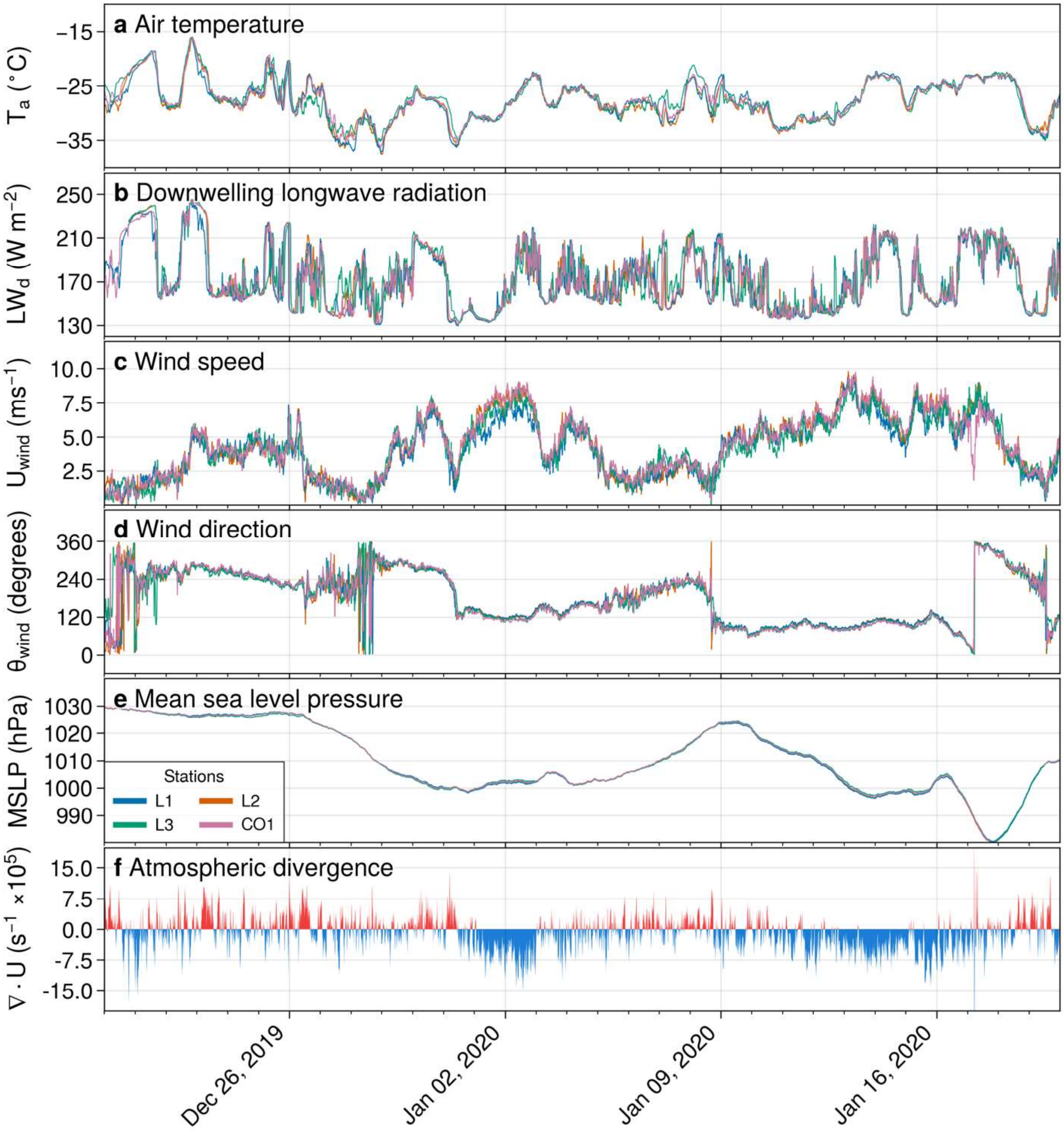

Figure 8. Time series of 10-minute means for meteorological measurements from late December to late January.

Observations from the meteorological installation at the Central Observatory (CO1 in the figure) and the three Atmospheric Surface Flux Stations at the L sites (L1–L3) during December 20, 2019–January 19, 2020: a) near-surface air temperature (T_a), b) downwelling longwave radiation (LW_d), c) wind speed (U_{wind}), d) wind direction (θ_{wind}; meteorological definition, opposite to the direction of motion), e) mean sea-level pressure (MSLP), and f) wind divergence across the L1–

L3 triangle ($\nabla \cdot U$; anomaly to the mean of the full time series). Note that the wind measurements at L1–L3 (Atmospheric Surface Flux Stations) were obtained at 3.8 m above the ice surface, and T_a at 2 m. Those at CO1 were obtained at approximately 6 m. The observational data can be found in Cox et al. (2023b 2023c; 2023d; 2023e).

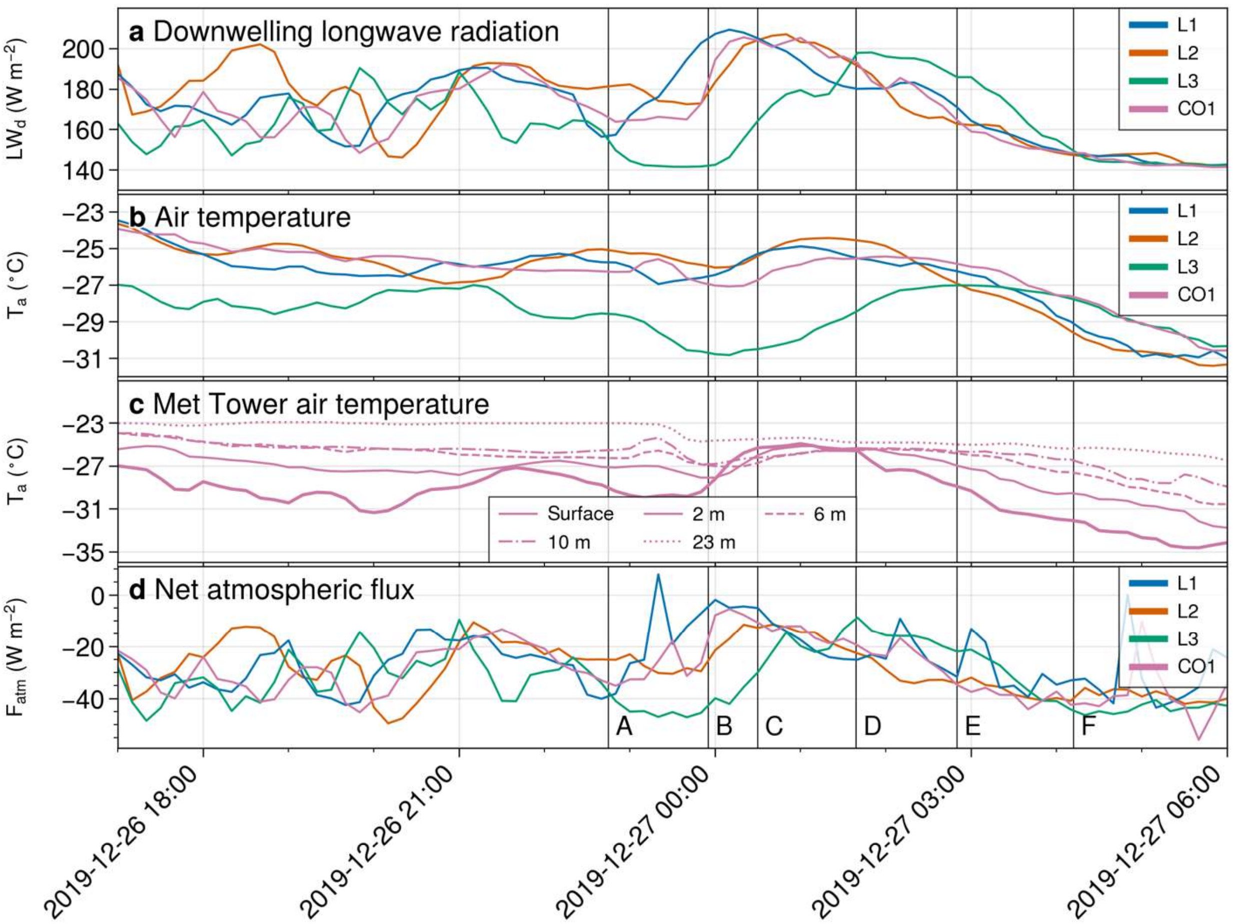

Figure 9. Time series of atmospheric variables between 17:00 December 26 and 06:00 December 27 in 2019.

a) Downwelling longwave radiation at the three L sites (L1–L3) and the meteorological installation at the Central Observatory (CO1), b) near-surface air temperature at the L sites (2 m height) and at CO1 (6 m height), c) air temperature at the different heights at CO1, and d) the net atmospheric energy flux (F_{atm}) at the three L sites and CO1. The six vertical lines labeled a–f show the times of the KaSACR reflectivity panels in Figure S4. The observational data are a subset of those shown in Figure 8.

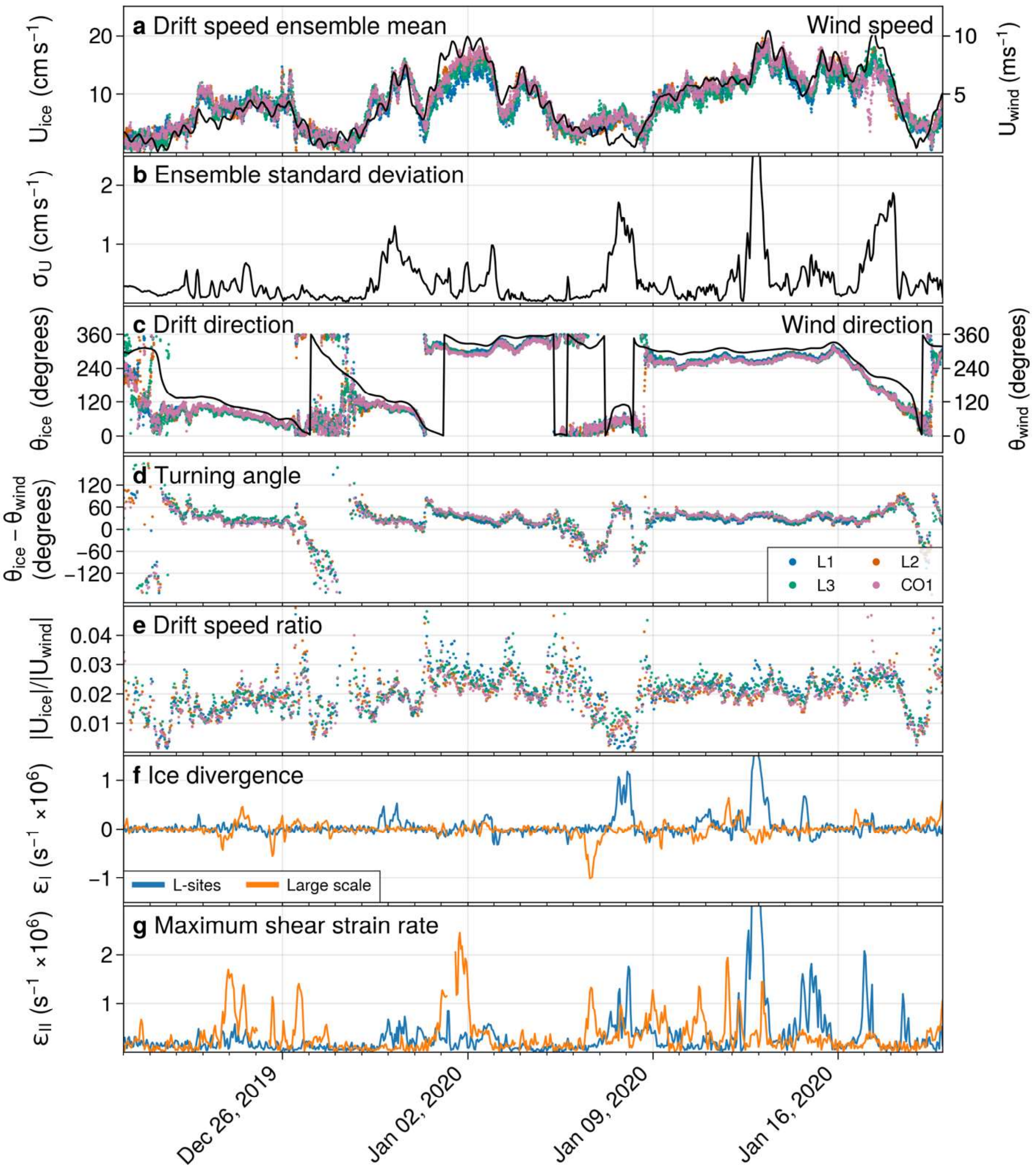

Figure 10. Time series of ice drift and deformation from late December to late January. Observations from the period December 19, 2019–January 19, 2020, for: a) wind speed at the L sites (L1–L3) and the Central Observatory (CO1; colored dots) and ensemble mean (black line) of ice drift speed of position-tracking buoys within the Distributed Network (DN; black line); b) standard deviation of the ensemble ice drift speed; c) ensemble mean drift direction and wind direction (positive in the direction of motion) of the time series in a; d) the difference between the

ice drift direction and the wind direction at the L sites and CO1 (turning angle); e) the ratio between the ice drift speed and the local wind speed at the L sites and CO1; f) the deformation calculated (following Hutchings et al., 2012; 2018) from buoys on the perimeter of the DN, where orange represents the large scale and blue shows the deformation of the L site triangle, which is a smaller scale; and (g) maximum shear strain rate for the same set of buoys as in panel f. Data from the L1–L3 sites and CO1 are shown in panels a–e as denoted by color in the legend. For panels a and c, only points where the wind speed was >1 m s^{-1} and drift speed >0.01 m s^{-1} are used. The data can be found under Bliss et al. (2022).

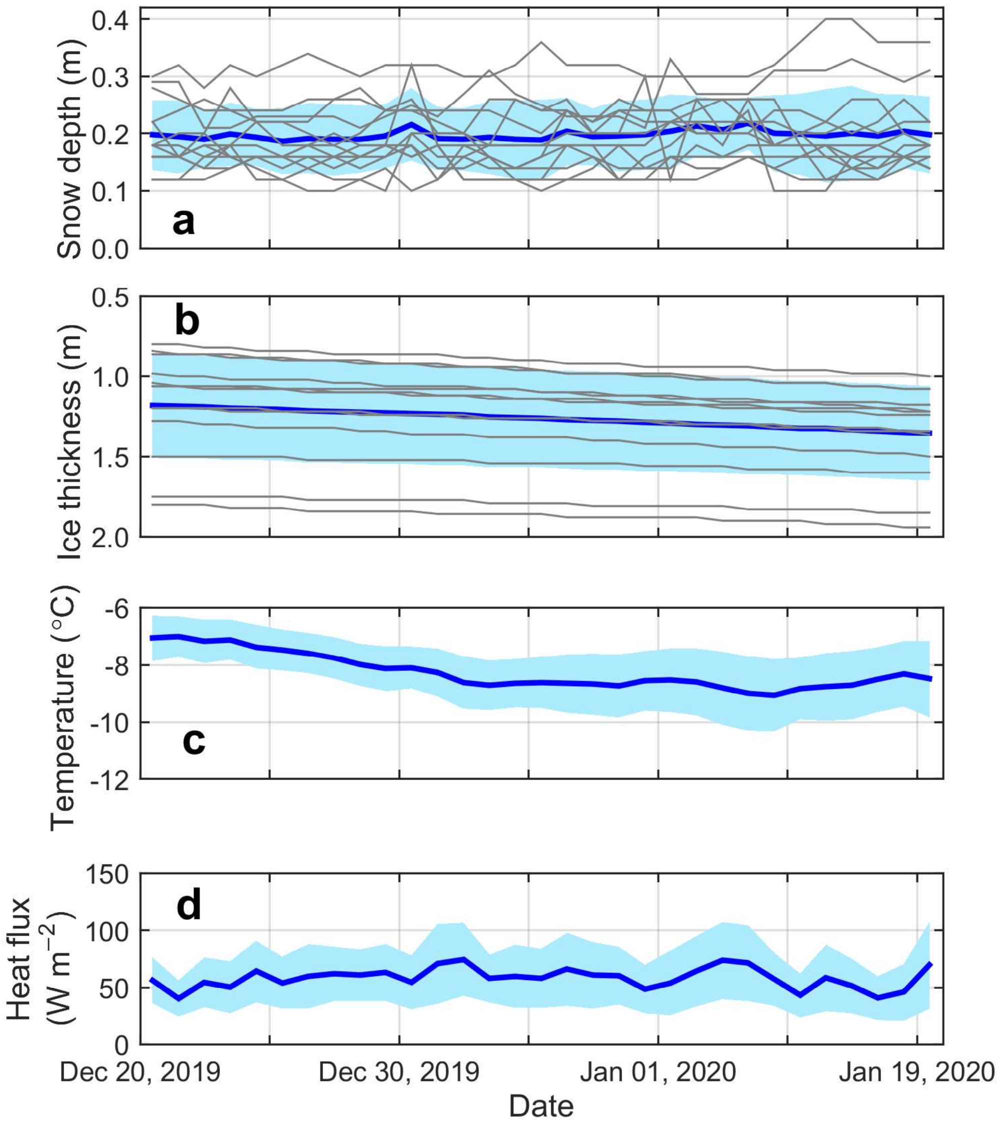

Figure 11. Snow and sea ice mass balance data from late December to late January. Observations of a) snow depth, b) ice thickness, c) bulk-average temperature through the ice layer, and d) conductive heat flux through the top ice layer during December 20, 2019–January 19, 2020, obtained from the measurements by 13 ice mass balance buoys (SIMBA; Table 1) deployed over the MOSAiC Distributed Network. The thick blue line and cyan shade are the average and standard deviation obtained from 13 measurement sites; the thin grey lines shown in panels a and b are the data obtained from each buoy. The data can be found under Lei et al. (2021b; 2021c; 2021d; 2022b; 2022c; 2022d; 2022e; 2022f; 2022g; 2022h; 2022I; 2022j; 2022k).

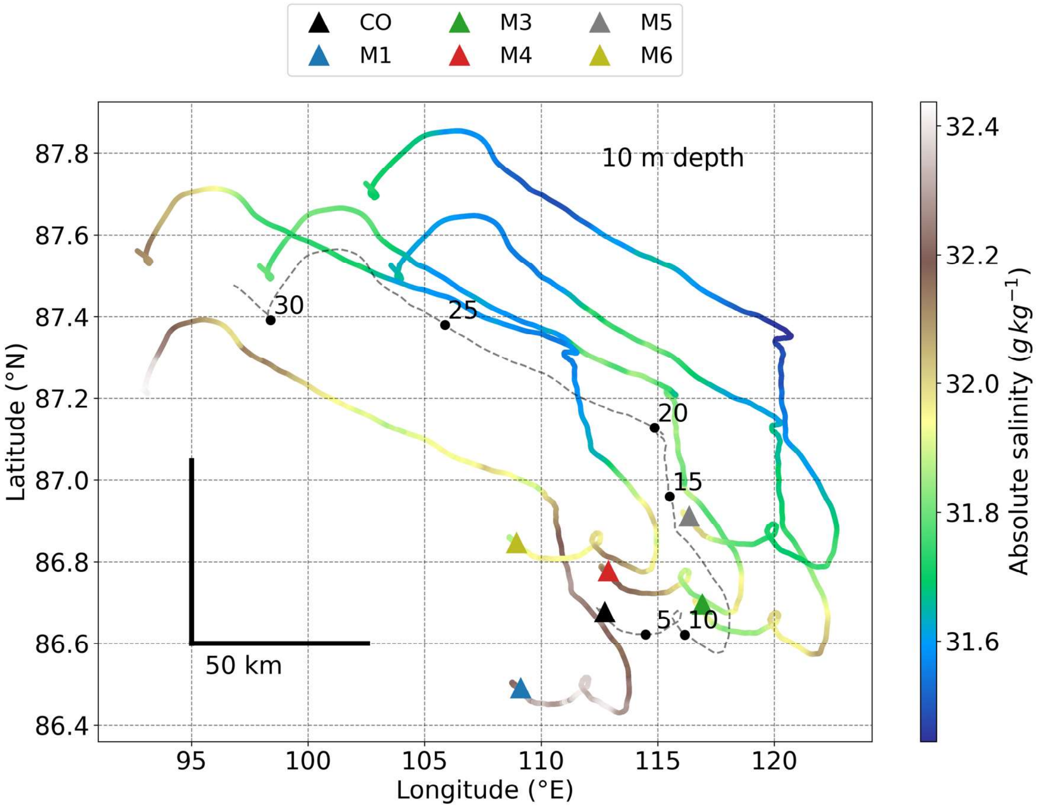

Figure 12. Horizontal distribution of absolute salinity at 10 m depth from late December to late January.

The initial positions of the buoys (denoted by site name in the legend) are denoted by colored triangles, and the track of the Central Observatory (CO) is denoted by the black dashed line. The numbers on the Central Observatory (CO) track are days from December 20, 2019. Absolute salinity is given in g kg^{-1} as defined by TEOS10 (see McDougall et al., 2010; McDougall and Barker, 2011). The data are from Salinity Ice Tether buoys (Hoppmann et al., 2022b).

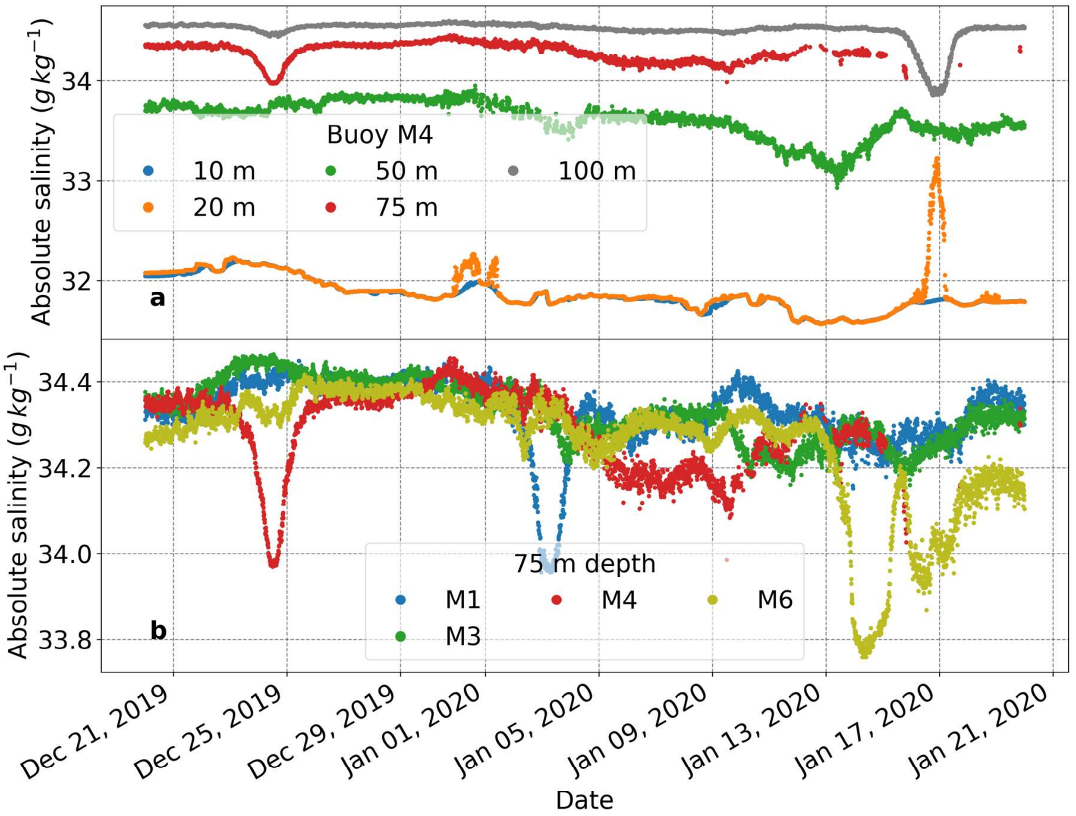

Figure 13. Absolute salinity at discrete depths across the Distributed Network from late December to late January.

The observations by different buoys with instruments at the depths shown are based on 10-minute measurement intervals. The depths (upper panel) and the sites (lower panel) are denoted by color, as shown in the legend. The data are from Salinity Ice Tether buoys (Hoppmann et al., 2022b).

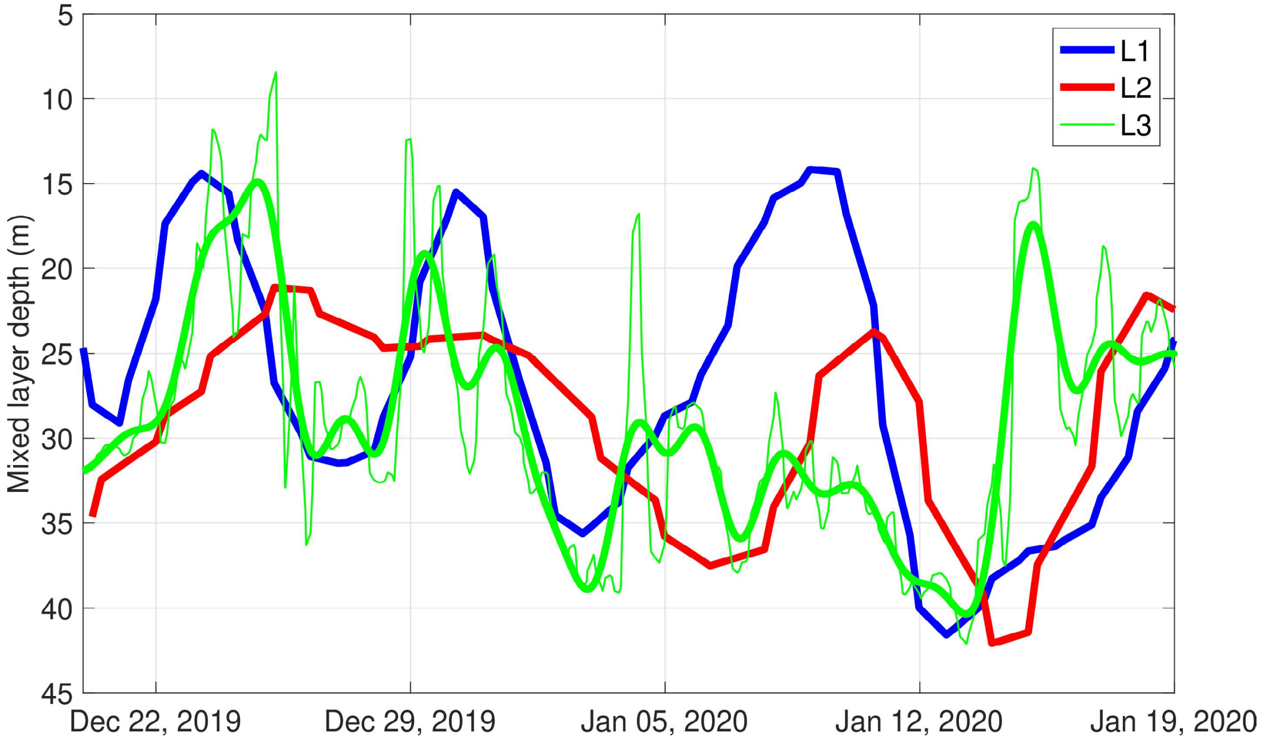

Figure 14. Time series of mixed layer depth at sites L1–3 from late December to early January.

The values are derived from conservative temperature and absolute salinity profiles (after TEOS10; see Figure 12) measured by the Woods Hole Ice-tethered Profiler at each L site, as denoted in the inset legend. The criterion for mixed layer depth assumes a density-step of 0.05 kg m^{-3} in accordance with Rabe et al. (2022), based on Toole et al. (2010). Note that the Woods Hole Ice-tethered Profiler at L1 and L2 only measured two profiles a day, whereas the one at L3 obtained profiles 8 times per day. Note that both the original values at L3 (thin line) and the 12-hour low-pass filtered values (5th order Butterworth filter; thick line) are shown. The Woods Hole Ice-tethered Profiler profile data can be found under Toole et al. (2016).

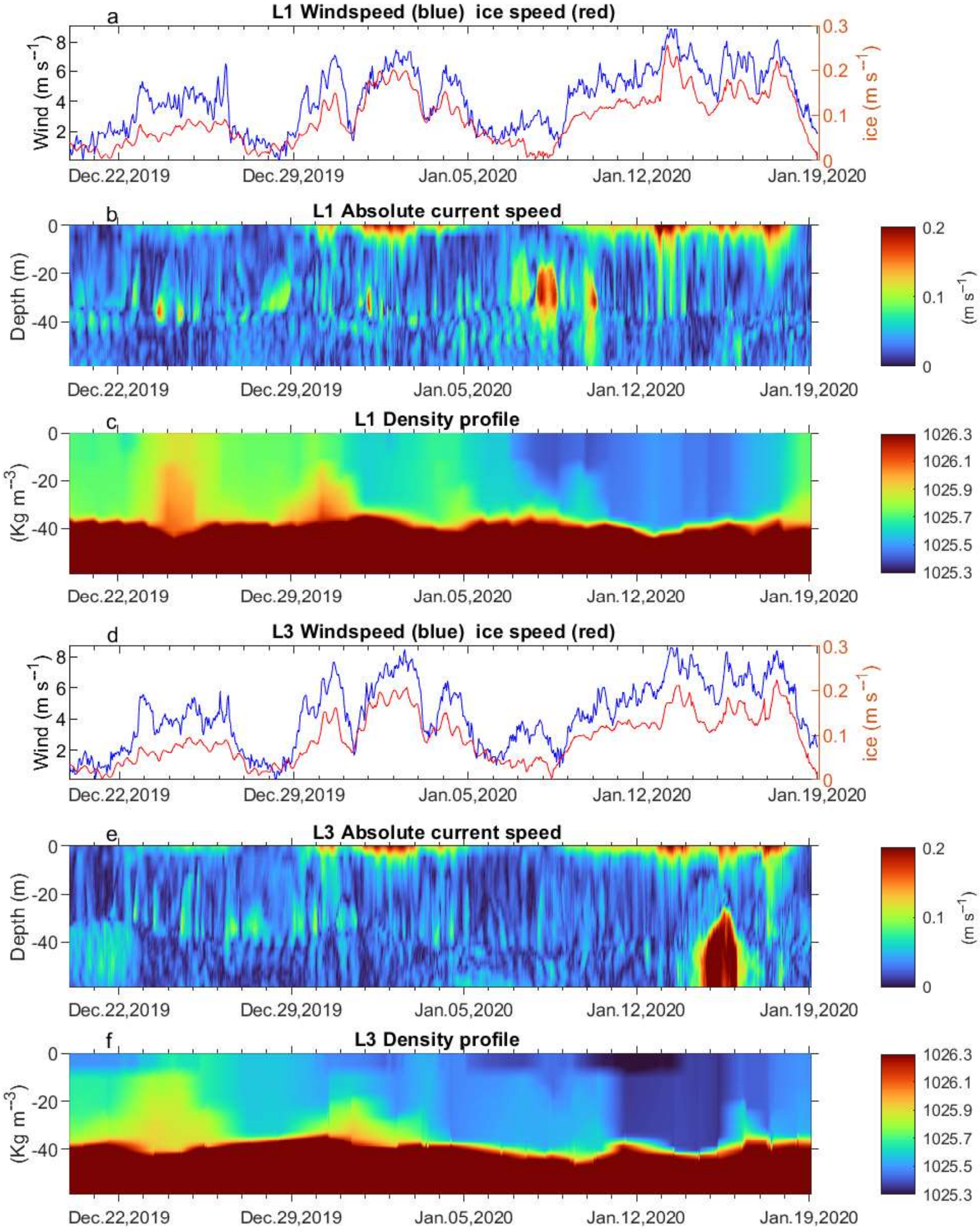

Figure 15. Wind, ice and ocean speed, and ocean density, from late December to late January .

Comparative observations at site L1 (a–c) and site L3 (d–f) of 1.8-m height wind forcing and ice speed (a, d), absolute current profiles with 15-minute averaging (b, e), and potential density, relative to 0 dbar (c, f). At each site the wind speed was measured by the adjacent Atmospheric Surface Flux Station, currents were derived from the acoustic doppler current profilers in the Autonomous Ocean Flux Buoys (AOFBs), and ice speed from the AOFB geographic position, while ocean density is based on observations by the co-located Woods Hole Ice-tethered Profiler (WHOI-ITP) CTD. The WHOI-ITP data can be found under Toole et al. (2016); the Atmospheric Surface Flux Station data are from Cox et al. (2023d; 2023e); the AOFB data are from Stanton and Shaw (2023a; 2023b; 2023c; 2023d).

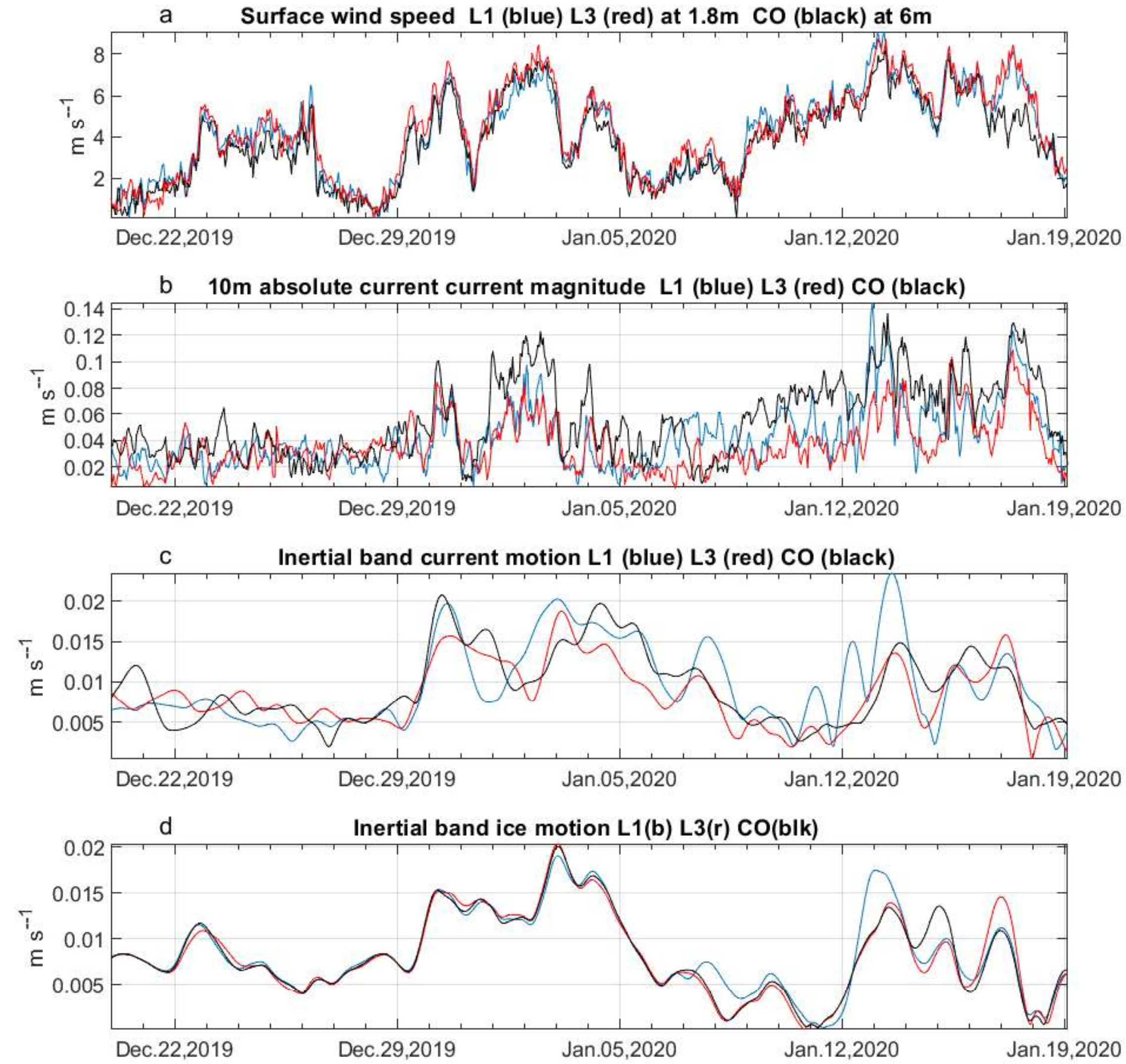

Figure 16. Wind speed, upper ocean currents and ice inertial band motion, late December to late January.

a) Observations of surface wind speed at sites L1, L3 and the Central Observatory (CO); b) corresponding 10 m depth absolute ocean current magnitudes; c) 0.3 f 6th order bandpass filtered 10 m depth inertial currents; and d) ice inertial band motion from Autonomous Ocean Flux Buoy (AOFB) position with the same filter used in panel c. The Coriolis parameter is $f = 2\omega\sin(\phi)$, where ϕ is the latitude and $\omega = 7.2921\ 10^{-5}\ \frac{rad}{s}$. The data in panel a are from Cox et al. (2023b; 2023d; 2023e); in panels b, c and d the AOFB data are from Stanton and Shaw (2023a; 2023b; 2023c; 2023d).

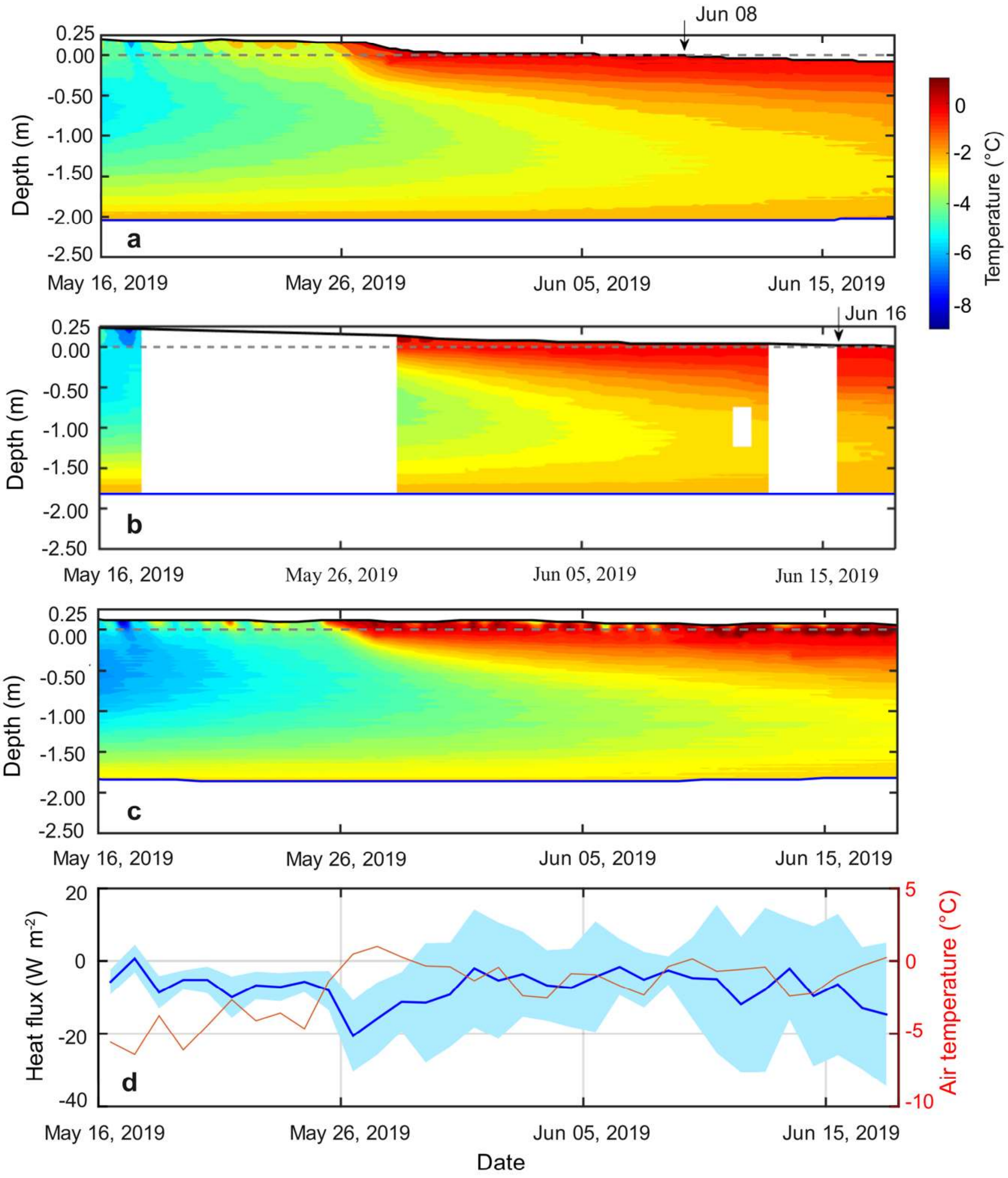

Figure 17. Late-spring snow and sea ice mass balance and conductive heat flux at the ice surface.

Changes in snow depth, ice thickness, and temperature at a) site L1, b) site L2, and c) site L3 May 16–June 18, 2020, with thick black line denoting snow or ice (after snow melted over) surface, grey dashed line denoting initial snow-ice interface, and thick black line denoting ice bottom. d)

Average (thick blue line) and standard deviation (shade) of daily conductive heat flux at the surface of the ice layer calculated from continuous measurements by 8 buoys at 5 sites (L1, L3, M3, M6, 1 buoy each; Central Observatory, 4 buoys). Also shown is the daily near-surface (2 m height) air temperature measured by the Unmanned (uncrewed) Ice Station at the site L3. These measurements agree approximately with measurements at 2 m height by Atmospheric Surface Flux Station #30 at the Central Observatory and can be expected to be representative of the region around the L sites, as spatial variability within the three Distributed Network sites with Atmospheric Surface Flux Stations installed was low for time scales greater than approximately 1 day (not shown). Data for panel a can be found under Lei et al. (2022c); for panel b, under Lei et al. (2022i); for panel c, under Lei et al. (2022k); and for panel d, under Lei et al. (2021b; 2022b; 2022c; 2022d; 2022g; 2022k; 2022l; 2022m).

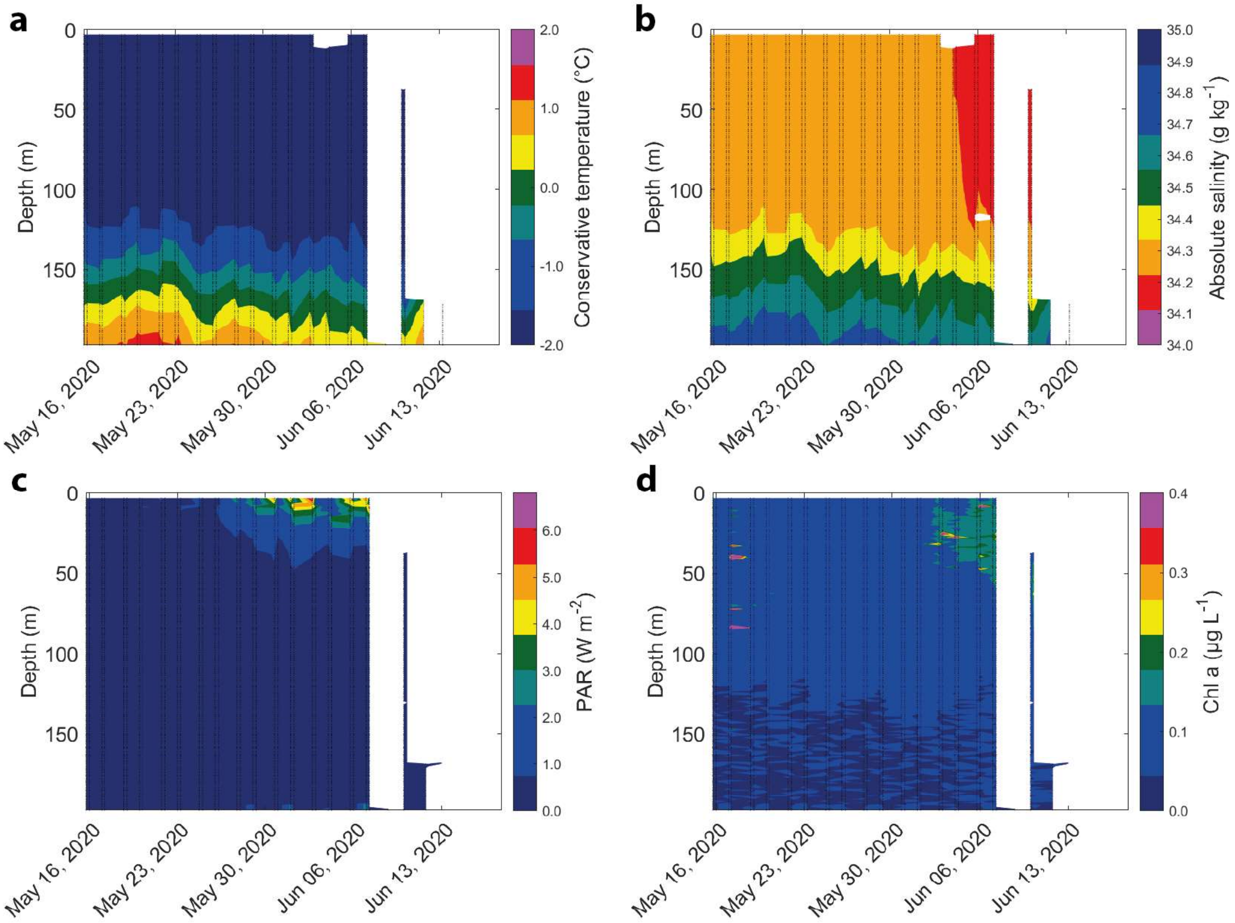

Figure 18. Ocean properties late May to early June, observed by Woods Hole Ice-tethered Profiler #94 at site L2.

Vertical sections are shown during the absence of manual observations for a) conservative temperature, b) absolute salinity, c) photosynthetically active radiation (PAR) and d) chlorophyll *a* (Chl *a*) based on fluorescence measurements and manufacturer's calibration (d); see Figure 12 for citations for TEOS10 conservative temperature and absolute salinity. Observed data locations are denoted by small black dots, and the contours are based on linear interpolation in the horizontal. Large gaps in observations are left blank; in early to mid-June the shallow topography likely led to the cable of the Woods Hole Ice-tethered Profiler at site L2 dragging across the seafloor and slanting from vertical, impeding the system from capturing full profiles. The interpolated, contoured section for Chl *a* in panel d reflects the actual point values (not shown). The data can be found under Toole et al. (2016).

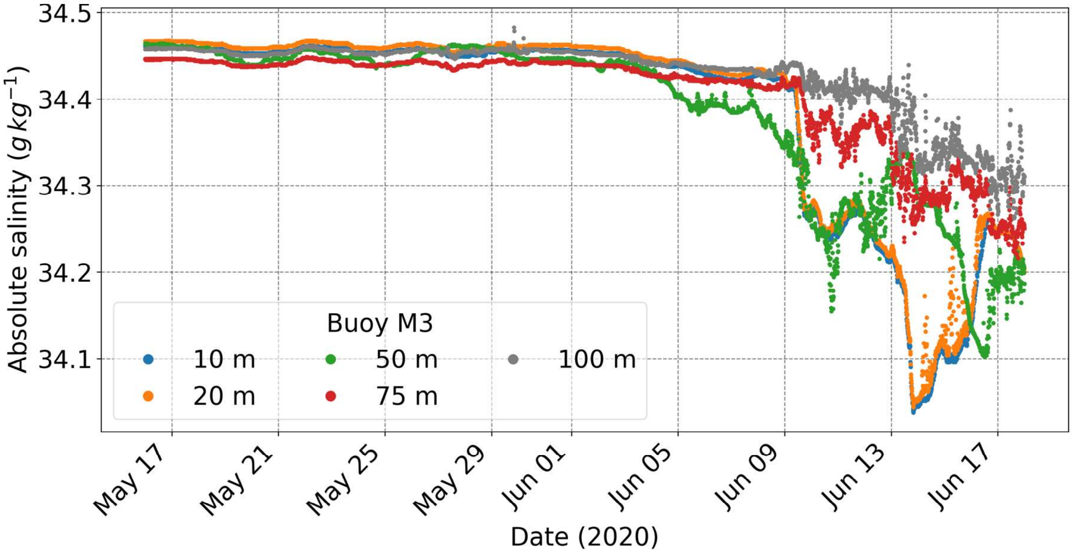

Figure 19. Absolute salinity at discrete depths at site M3 from late May to early June. The observations are by the same type of instrument as in Figure 13 but shown for May 16–June 18, 2020, with depths denoted by color, as shown in the legend. The data are from Salinity Ice Tether buoys (Hoppmann et al., 2022b).

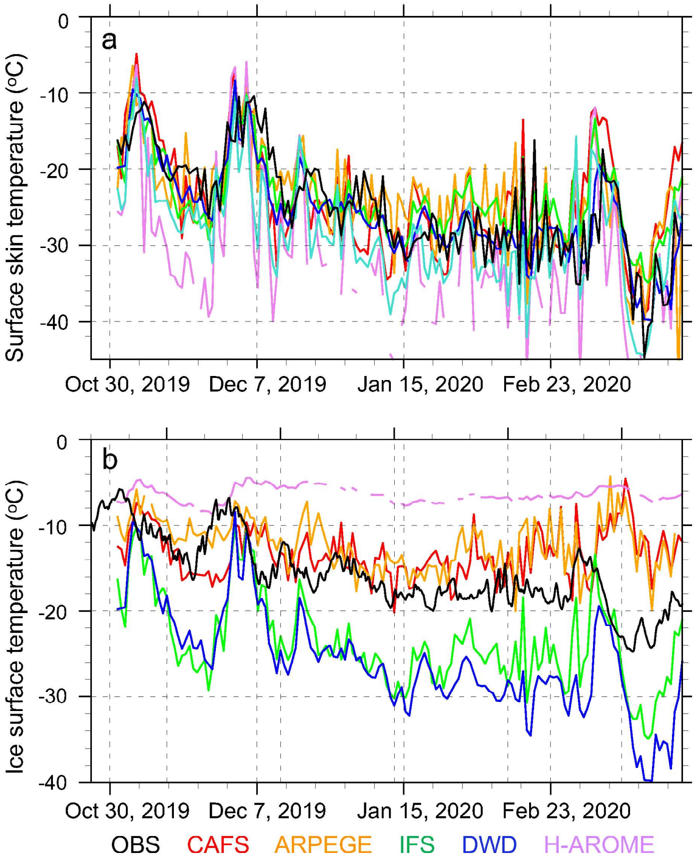

Figure 20. Comparison of wintertime observations and 2-day forecasts during October 15, 2019–March 15, 2020.

Observations (OBS, black lines) of a) skin temperature and b) surface ice temperature, averaged across the L sites and the Central Observatory meteorological installation, and compared to 2-day forecasts at the location of RV *Polarstern*. Forecasts systems (color-coded) shown: NOAA-PSL Coupled Arctic Forecast System (CAFS; red), Météo-France ARPEGE-GELATO forecast system (ARPEGE; orange), ECMWF Integrated Forecast System (IFS, green), German Weather Service forecast system (DWD; blue) and HARMONIE--AROME (H-AROME; purple). Details of these systems can be found in Solomon et al. (2023) and references therein.

Tables and full captions

Table 1. Types of autonomous buoy systems used during MOSAiC.

Buoy type (abbreviation)[a]	Reference	Buoy label[b]
Light strings (OptiCAL; formerly Envipope/LITO)	Schartmüller et al. (2023)	E buoy
Autonomous Ocean Flux Buoy (AOFB)	Stanton et al. (2012)	F buoy
Seasonal Ice Mass Balance buoy (SIMB3)	Planck et al. (2019)	I buoy
Bruncin-type Ice Mass Balance buoy with additional sensors (IMB-flex)	—[c]	M buoy
Salinity Ice Tether (SIT) with CTD	Hoppmann et al. (2022a)	O buoy
Position-tracking buoys (surface velocity profilers/ice trackers) of various types (SVP-B, IceTracker, iSVP, SVP-BT, Calib)	Bliss et al. (2023)	P, C buoy
Spectral radiation station and bio-optical buoys (Spectral Radiation Station, RITBOB); sometimes with additional instrumentation	Tao et al. (n.d.)	R buoy
Snow buoy (Snow Buoy)	Nicolaus et al. (2021a)	S buoy
Snow Ice Mass Balance Apparatus (SIMBA)	Jackson et al. (2013)	T buoy
UpTempO (UpTempO)	University of Washington (2024)	U buoy
Drift-Towing Oceanic Profiler (DTOP)	Li et al. (2021a)	V buoy
Woods Hole Ice-Tethered Profiler (WHOI ITP, WHOI BIO-ITP, WHOI ITP-V)	Toole et al. (2011); Krishfield et al. (2008); Cole et al. (2015)	W buoy
Atmospheric Surface Flux Station (ASFS)	Cox et al. (2023a)	—[d]
Dynamic Ocean Topography (DOT) Buoy	Lee et al. (2022)	—[d]
Unmanned (uncrewed) Ice Station (UMIS_PRIC_Ice, UMIS_PRIC_Ocean)	Lei et al. (2022)	—[d]
Acoustic Zooplankton Fish Profiler (AZFP) buoy	Flores et al. (2023)	—[d]
Light harp (light harp)	—[c]	—[d]
Salt harp (salt harp)	Notz et al. (2005)	—[d]
First Institute of Oceanography fixed-level buoy (FIO FLB)	—[c]	—[d]
Second Institute of Oceanography sediment trap (SIO sediment trap)	—[c]	—[d]

---

[a] Technical name by users/manufacturer; see Table S1 for detailed descriptions of the variables measured by each type, and Table S2 for a full list of buoys and their labels, where appropriate

[b] Nomenclature on meereisportal.de, distinguished by single letters in the label

[c] Citations for these buoys are not yet available, as they include novel technology

[d] Buoys without a label have not been available in near-real time through the seaiceportal.de, although some have been provided at other portals.

Table 2. Mean values of downwelling longwave radiation (LW_d), near-surface air temperature (T_a), and net surface energy flux (F_{atm}) measured[a] at 4 sites in the Distributed Network December 20, 2019–January 19, 2020.

Site	LW_d (W m^{-2})	T_a (°C)	F_{atm} (W m^{-2})[b]	Ice thickness (m)[c]	Snow depth (m)[c]	Initial distance to Central Observatory (km)[d]
"Met City" at Central Observatory (6 m height Ta):	172.1	*–27.5* [e]	–29.0	—[f]	—[f]	<1
L1 (2 m height T_a):	171.4	–27.7	–27.9	1.10	0.072	15
L2 (2 m height T_a):	172.8	–27.8	–26.8	1.27/1.54[g]	0.038/0.035[g]	12
L3 (2 m height T_a):	173.2	–27.5	–29.2	1.27	0.040	22

---

[a] LW_d and T_a are from the time series in Figure 8a and b; F_{atm} is from the same instrument system (not shown in the figure).

[b] Heights of measurements contributing to F_{atm} are considered unimportant, as all were within the atmospheric surface boundary layer.

[c] Mean values based on the time series shown in Figure 11 for sites L1–L3

[d] On December 20, 2019

[e] Value may not be comparable to values at the L sites, as it was measured at a different height.

[f] No autonomous observations of ice thickness and snow depth available close to the "Met City" installations

[g] Values are from two buoys at site L2.

Supplementary material for

The MOSAiC Distributed Network: observing the coupled Arctic system with multidisciplinary, coordinated platforms

Text S1. Further details on the planning process of the Distributed Network

The originally planned layout had considered the radially distributed network of sites around RV *Polarstern* ("PS" in Figure S1), with a corridor for logistics access by supply vessels (gray shading in Figure S1) with only few buoy sites and none of the heavily instrumented L sites. The position-tracking buoys (labels starting with "P" in Figure S1) had been clustered around RV *Polarstern* and each of the M and L sites. One M site ("MF") at 40 km distance to RV *Polarstern* had been planned, in addition, to capture conditions far away from the Central Observatory and the core of the distributed sites. This arrangement had been projected prior to the expedition onto satellite images of the larger region, including situations where marginal-ice-zone condition dominated, around the planned deployment of the MOSAiC Central Observatory (Figure S2). Further details of how floes were identified directly before buoy deployment in the field, using advanced products from satellite observations, can be found in Krumpen and Sokolov (2020).

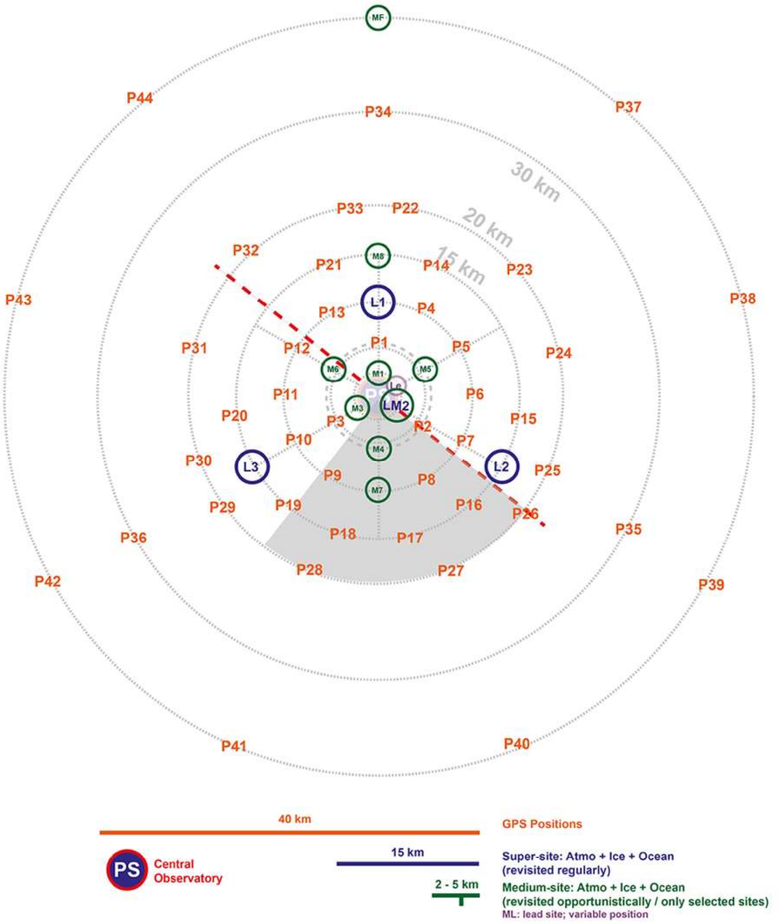

Figure S1. Planned layout of the DN prior to deployment in October 2019.
The different site types are distinguished by color as shown in the legend: L sites (blue), M sites (green) and P sites (orange). The Central Observatory with RV *Polarstern* is located in the centre, where the ship's assumed orientation is along the red dashed line. The gray shaded area denotes the logistics corridor planned for approach of supply ships.

Figure S2. A modified version of the layout from Figure S1 projected onto a satellite image. The sites were adjusted to fit the ice conditions in the marginal ice zone captured in this satellite image from MODIS, taken on September 29, 2017 around 79 N and 140 E. (NASA, 2017).

Table S1. Extended description of autonomous (buoy) system types as used during MOSAiC.

Buoy Type (abbreviation)[a]	Variable / measurement	Reference[b]	Buoy Label[c]
Light strings (OptiCAL; formerly Envipope/LITO)	Global Positioning System (GPS) position; light measurements at three wavelengths, chlorophyll a fluorescence	Schartmüller et al. (2023)	E buoy
Autonomous Ocean Flux Buoy (AOFB)	GPS position; eddy correlation fluxes of heat salt and momentum at 3 m depth, temperature, conductivity and salinity at 3 m depth, water velocity components every 2 m to 80 m depth, GPS position, 50 m depth thermal diffusivity	Stanton et al. (2012)	F buoy
Seasonal Ice Mass Balance buoy (SIMB3)	GPS position; sea ice thickness & snow depth (calculated from ultrasonic pingers), air, snow, ice and ocean temperatures at 0.02 m vertical spacing (thermistor chain)	Planck et al. (2019)	I buoy
Bruncin-type Ice Mass Balance buoy with additional sensors (IMB-flex)	GPS position; barometric pressure; hull temperature and humidity; Optional: *Chlorophyll a* & CDOM fluorescence, optical backscatter at 700 nm; ocean temperature, salinity, and pressure (SBE37 MicroCat); dissolved oxygen; air, snow, ice & ocean temperatures at 0.02 m vertical spacing (thermistor chain); camera images	—	M buoy
Salinity Ice Tether (SIT) with CTD	GPS position; T/S/P (SBE37 Microcat), surface temperature	Hoppmann et al. (2022a)	O buoy
Positioin-tracking buoys (surface velocity profilers / ice trackers) of various types (SVP-B, IceTracker, iSVP, SVP-BT, Calib)	GPS position. Optional: barometric pressure, surface temperature	Bliss et al. (2023)	P, C buoy
Spectral radiation station and bio-optical buoys (Spectral Radiation Station, RITBOB); sometimes with additional instrumentation	GPS position; barometric pressure; hull temperature & humidity; shortwave spectral radiation (incident, reflected, and transmitted). Optional: *Chlorophyll a* & CDOM fluorescence, optical backscatter at 700nm; ocean temperature, salinity, and pressure (SBE37 MicroCat); dissolved oxygen; air, snow, ice & ocean temperatures at 0.02 m vertical spacing (thermistor chain); WRGB light transmission at 0.05 m vertical spacing (light chain); camera images. Some units without telemetry	Tao et al. (n.d.)	R buoy

---

[a] Technical name by users/manufacturer; see Table S1 for detailed descriptions of the variables measured by each type, and Table S2 for a full list of buoys and their labels, where appropriate

[b] Citations for some of these buoys are not, yet, available, as they include novel technology

[c] Nomenclature on meereisportal.de, distinguished by single letters in the label. Buoys without a label have not been available in near-real time through the seaiceportal.de, although some have been provided at other portals

Table S1 continued.

Buoy (Type)	Variable / measurement	Reference	Buoy Label
Snow buoy (Snow Buoy)	GPS position; snow depth (4x), air temperature (1.5m), barometric pressure	Nicolaus et al. (2021a)	S buoy
Snow Ice Mass Balance Apparatus (SIMBA)	GPS position; air, snow, ice & ocean temperatures at 0.02 m vertical spacing (thermistor chain)	Jackson et al. (2013)	T buoy
UpTempO (UpTempO)	GPS position; ocean state (T/P) at different depths	University of Washington (2024)	U buoy
Drift-Towing Oceanic Profiler (DTOP)	GPS position; ocean state (T/S), surface meteorology (P/T/q), optional chlorophyll a, dissolved oxygen, ice T profile.	Li et al. (2021a)	V buoy
Woods Hole Ice-Tethered Profiler (WHOI ITP, WHOI BIO-ITP, WHOI ITP-V)	GPS position; ocean state (T/S/P), dissolved oxygen; optional: *Chlorophyll a* and CDOM fluorescence, optical backscatter at 700nm; ocean current velocity	Toole et al., (2011); Krishfield et al. (2008); Cole et al. (2015)	W buoy
Atmospheric Surface Flux Station (ASFS)	GPS position; surface meteorology (P, T, RH, winds), broadband radiative fluxes, surface turbulent heat fluxes, surface net heat flux, surface height change, surface skin temperature	Cox et al. (2023a)	—
Dynamic Ocean Topography (DOT) Buoy	GPS position; barometric pressure, temperature, sea surface height, pressure at 1m depth.	Lee et al. (2022)	—
Unmanned (uncrewed) Ice Station (UMIS_PRIC_Ice, UMIS_PRIC_Ocean)	GPS position; snow depth, ice thickness, snow-ice temperature profile, spectral radiation at 6 layer from upper surface to the water under the ice; ocean: conductivity and temperature of upper ocean at 5 fixed layer to 40 m under the ice, and dissolved oxygen/chlorophyll a at 5 and 20 m under the ice	Lei et al. (2022)	—
Acoustic Zooplankton Fish Profiler (AZFP) buoy	GPS position; barometric pressure, internal temperature and humidity; incoming broadband radiation, AZFP acoustic backscatter at 4 frequencies, chlorophyll a fluorescence, optical backscatter, webcam images	Flores et al. (2023)	—
Light harp (light harp)	Temperature, light (incoming and outgoing) in ice	—	—
Salt harp (salt harp)	Salinity in ice	Notz et al. (2005)	—
First Institute of Oceanography fixed-level buoy (FIO FLB)	GPS position; ocean state (T/S/P) at different depths		—
Second Institute of Oceanography sediment trap (SIO sediment trap)	collection of sediment samples, position	—	—

Text S2. Implementation of the mDN

In autumn 2020 the mDN was installed along the transit of RV *Polarstern* as it moved back northward into the central Arctic as well as in and around a new Central Observatory. This mDN was much less instrumented than the original DN and focused on detailed studies of surface re-freezing and new ice formation to characterize the transition from the summer melt season into freeze-up. This included snow thickness changes after initial freeze-up. Most buoys were installed within the Central Observatory and recovered towards the end of the drift with RV *Polarstern* by September 20, 2020. As the DN, the remaining buoys of the mDN continued reporting, drifting into the North Atlantic as late as summer 2022, the last one transmitting until September 2023 (2020P220).

The larger-scale mDN consisted of two Snow Buoys and eight position-tracking buoys with barometric pressure. These units were deployed on remote ice floes during the transits to (August 16 to 23, 2020) and from (September 21 to 30, 2020) the last implementation of the Central Observatory (Fgure S3a). A small-scale mDN was established around the main ice camp of this Central Observatory (Figure S3b, c and d) where 22 ice drifters were deployed, 10 of the drifters within 1 km of the ship, and the other 12 in equal amounts at about 4.5 km, 9 km, and 28 km distance to the ship. Within the Central Observatory, the devices were installed across different surface types, e.g., ridges, melt ponds, leads, or bare ice, to enable comparative studies of level and deformed ice and different types of freezing water surfaces. These installations consisted of five IMBs, four Snow Buoys, two radiation stations equipped with spectral radiometers, one Salinity Ice Tether buoy (Conductivity Temperature Depth), a twin-buoy setup equipped with an Acoustic Zooplankton Fish Profiler and a suite of complementary biooptical sensors. A recovered Autonomous Ocean Flux Buoy was partially re-deployed at the Central Observatory. Atmospheric Surface Flux Station #50 and Atmospheric Surface Flux Station #30 were deployed near a lead and within a melt pond, respectively, obtaining energy budgets during freeze-up over surfaces different from the main Central Observatory meteorological installation during this important transition period. Three position-tracking buoys were deployed in a triangle around an eddy covariance system installed close to a ridge. These mDN deployments provide a distributed network of observations that has a scale smaller than the original DN, and are also given in Table S2.

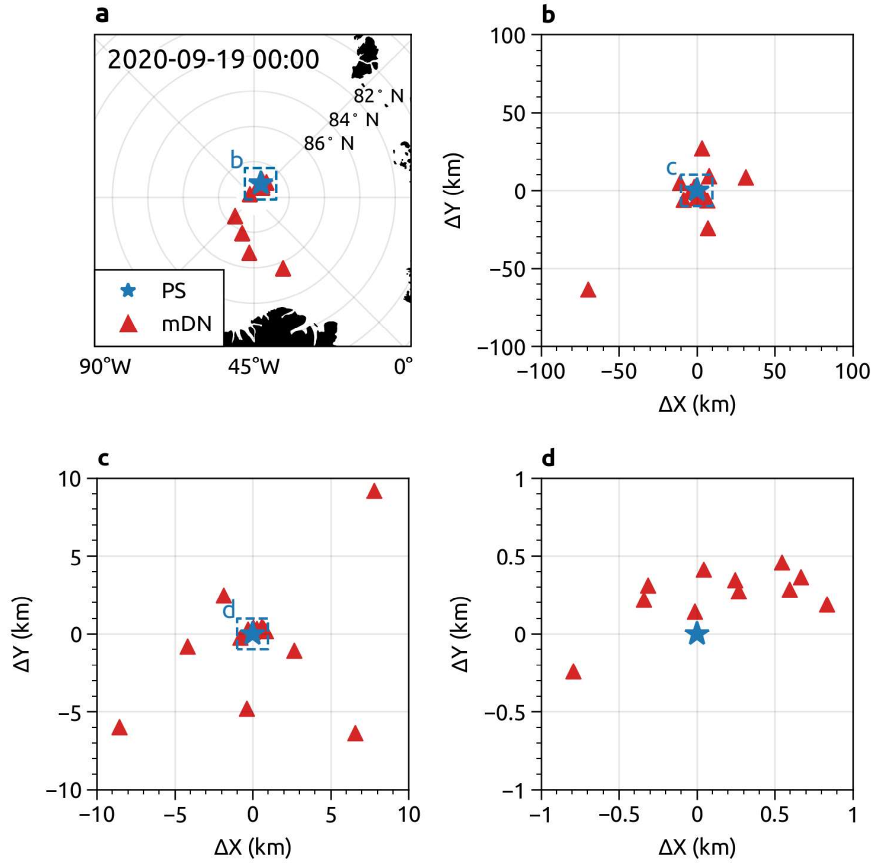

Figure S3. Positions of the main sites of the Distributed Network during the final leg. Position of the buoys in the second ("mini") implementation of the Distributed Network (mDN) on September 19, 2020. (a) shows the buoys deployed enroute to the site (red triangles) and the northernmost buoys remaining from the initial Distributed Netowork (gold circles). The blue star marks the location of the RV *Polarstern*. (b)–(d) show progressively smaller scales, with the boundaries of each panel marked by the blue dashed line in each prior panel.

Text S3. Drift trajectories for each site

For some sites, data sets from different buoys / sources were merged. While, by design, the drift and position of each P site are provided by the one buoy at each site (Bliss et al., 2022, 2023), the drift trajectory and position of all L and M sites are defined by merging the time series of selected buoys at each site (as in Nicolaus et al. 2021b). Data source names are consistent with the short names of sensor.awi.de and meereisportal.de, as well as with the tables in the MOSAiC cruise reports. In addition, the unique International Mobile Equipment Identity (IMEI) number is given. The original measurement frequency also depends on the platform technical properties and varies between 1 s and 1 h. The resulting data set is interpolated to hourly position data. The end dates given in Table S3 refer to the last position reported by the buoy. While all buoys were deployed on sea ice, most buoys melted out of the ice during their drift and continued in the open ocean. Hence, positions are not necessarily sea ice drift / positions. The selection of the formal position of each site was based on the following criteria:

- Length of the time series: The aim is to cover the entire time series until the last unit stopped reporting positions
- Frequency of measurements: Higher frequency is preferred, as the final data product was chosen to have a temporal resolution of 1 hour, which was the reporting interval of most units

Table S2. Autonomous (buoy) system deployments during MOSAiC, explained in Text S4.

The table is provided as an Excel file.

Text S4. Explanatory text related to Table S2.

For some sites, data sets from All buoy deployments are listed by the buoy label (meereisportal.de), buoy type, and date and site of deployment. The sites are given as “CO” (Central Observatory), “L1–L3”, “M”, “LM” for the DN; and “mDN” for the Central Observatory mDN deployments. Note that several platforms were recovered and then redeployed, denoted as a new deployment. The Buoy Type is defined in Tables 1 and S1. Where available, other buoy labels, such as labels given by the respective PI, are given under “Original Buoy Label”. Several buoys labelled starting with “P” and “U” were not deployed at one of the main sites but stand-alone on separate ice floes; here, no site labels are given, and the reader is referred to Bliss et al. (2023). Several buoys did not have telemetry and are listed as “local storage” under “IMEI”, though several did have radio links to transmit a subset of the data to the ship, such as the Atmospheric Surface Flux Station. Note that IMEI usually end on "0”; those listed with “1” or “2” at the end are internal numbers denoting the first and second redeployment of each buoy instrument package, respectively. A few buoys were not displayed in the meereisportal.de and, hence, do not have a corresponding buoy label. DN sites labelled starting with “Ak” were part of the DN extended network (Figure 1) and are not detailed further here.

Table S3. Data sources of the drift trajectories for each site[a].

Site[b]	Operational time range	IMEI[c] number	Data source	*f*[d]	Reference
CO1	October 4 2019 – April 23, 2020	—[e]	RV *Polarstern*	1 s	Rex (2020), Haas (2020), Kanzow (2020)
CO1	April 23, 2020 – November 11, 2020	300234068210310	2020P225	1 h	Lei et al. (2021a)
CO2	June 19, 2020 – June 26, 2020	—[e]	RV *Polarstern*	1 s	Rex (2021a), Rex (2021b)
CO2	June 26, 2020 – August 19, 2020	300025010649550	2020M26	1 h	Granskog et al. (2020)
CO3	August 21, 2020 – August 28, 2020	—[e]	RV *Polarstern*	1 s	Rex (2021b)
CO3	August 28, 2020 – August 9, 2021	300234068066320	2020O10	10 min	Hoppmann et al. (2021d)
L1	October 5 2019 – August 6, 2020	300234068704730	2019T67	30 min	Lei et al. (2021b)

---

[a] The full drift data set can be found under Nicolaus et al. (2021b).

[b] "CO1", "CO2" and "CO3" are used in the drift data set to denote different implementations of the Central Observatory, so that CO1 and CO2 were part of the first Distributed Network (DN), whereas CO3 was part of the second ("mini") implementation of the Distributed Network (mDN)

[c] International Mobile Equipment Identity

[d] Original measurement frequency

[e] The ship is not an autonomous buoy and does not have an IMEI

L2	October 7 2019 – August 18, 2020	300025010524990	2019W2	1 h	Toole et al. (2016)
L3	October 11 2019 – August 7, 2020	300234066081170	2019S94	1 h	Nicolaus et al. (2020b)
LM	October 29 2019 – August 14, 2020	300234068706330	2019T66	30 min	Lei et al. (2021c)
M1	October 5 2019 – May 9, 2020	300234067068380	2019V1	1 h	Li et al. (2021b)
M2	October 7 2019 – August 9, 2020	300234067064490	2019V2	1 h	Li et al. (2021c)
M3	October 7 2019 – August 3, 2020	300234066444880	2019S81	1 h	Nicolaus et al. (2020a)
M4	October 8 2019 – August 14, 2020	300234068166760	2019O4	10 min	Hoppmann et al. (2021a)
M5	October 9 2019 – August 17, 2020	300234067066520	2019V4	1 h	Li et al. (2021d)
M6	October 10 2019 – August 13, 2020	300234068514740	2019O6	10 min	Hoppmann et al. (2021b)
M7	October 11 2019 – October 25 2019	300234068519770	2019O7	10 min	Hoppmann et al. (2021c)
M8	October 11 2019 – September 29, 2020	300234068700320	2019T69	1 h	Lei et al. (2021d)

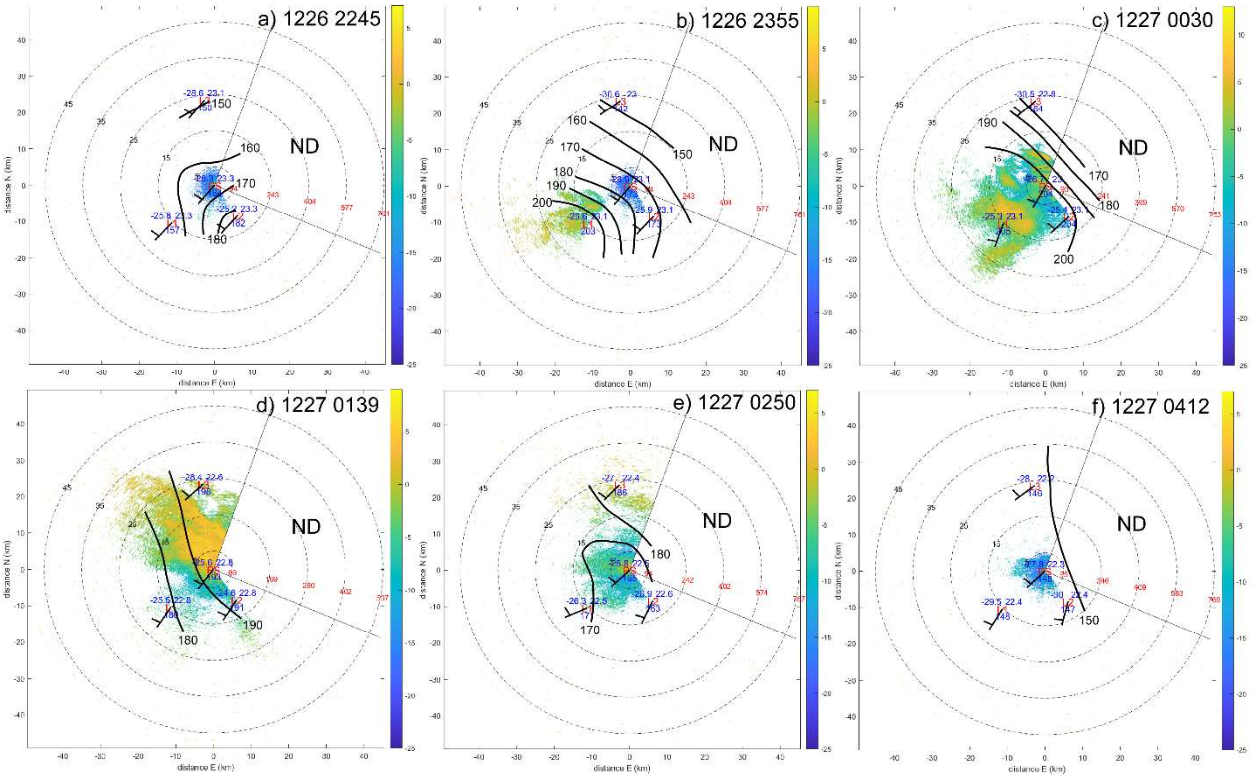

Figure S4. Radar reflectivity intensity (dBz) from the scanning Ka-band Doppler radar. The maps are at the six times shown in Figure 9 (Date & time shown in upper right). The L sites are indicated, while RV *Polarstern* (PS) is located at the center of each figure (note that the meteorological installations in the Central Observatory, “Met City", are <500 m from PS). The near-surface observations of air temperature, surface pressure, LW_d, and wind speed / direction are given at each of these surface sites. The isopleths show the analysis of the LW_d field (isopleth interval 10 W m^{-2}) based on these observations. The range from the radar (black numbers; km) is shown by the dashed concentric circles, which are also labeled by the height above the local surface (red; meters). Radar data was not obtained in the delineated sector to the northeast labeled “ND”. A signal-to-noise threshold of –10 dB is used for the reflectivity. The scanning Ka-band radar was operated by the United States Department of Energy Atmospheric Radiation Measurement program and was able to obtain meaningful radar reflectivity measurements of even fairly shallow clouds to a range of approximately 35 km using elevation angles <1°. These radar volumes were obtained every approximately 12 minutes and approximately covered the domain of the Distributed Network (DN) at a resolution of about 100 m. The spatial scales shown by the scanning radar data aids in upscaling atmospheric forcing parameters from variables measured at the DN sites.

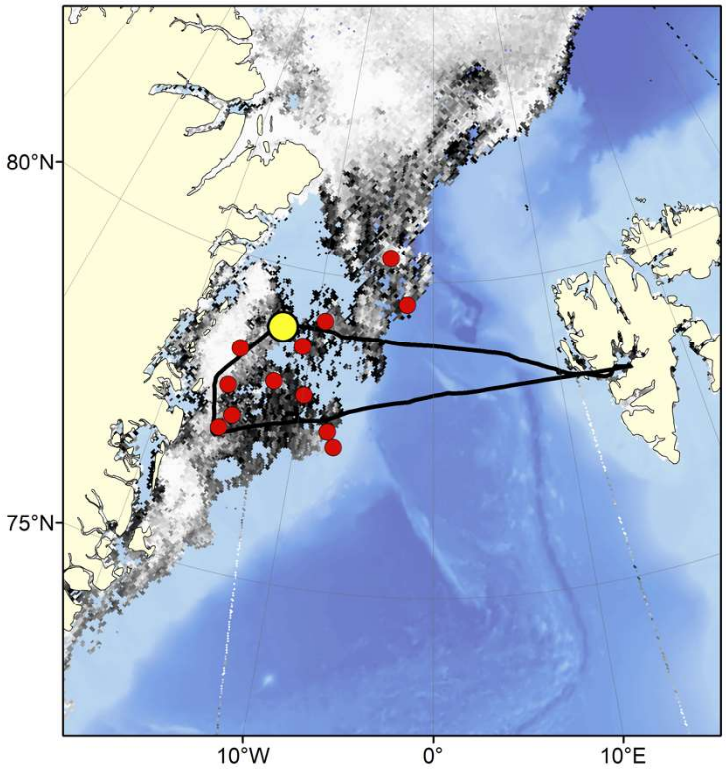

Figure S5. Map with the flight path of Polar 6 on September 2, 2020. The red dots indicate the position of active buoys from the MOSAiC DN. The yellow dot indicates the position of the icebreaker *Kronprins Haakon* (NPI) that was carrying out sea ice and oceanographic surveys in Fram Strait. The flights were part of the MOSAiC IceBird Campaign (Belter et al. 2021, Herber et al. 2021).

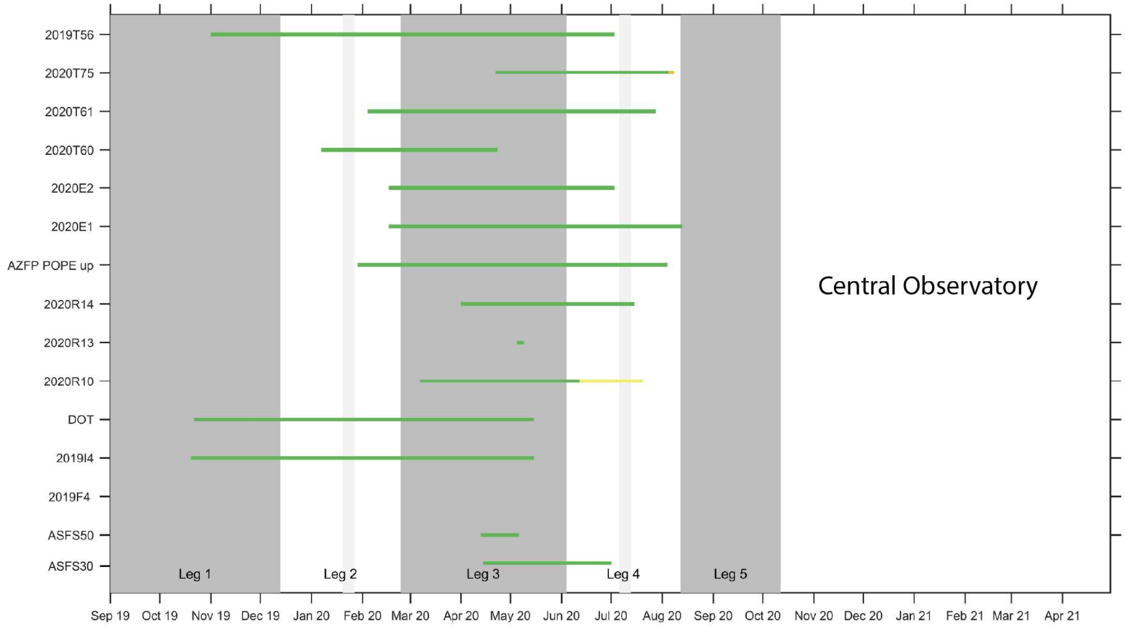
Central Observatory
2019T56
2020T75
2020T61
2020T60
2020E2
2020E1
AZFP POPE up
2020R14
2020R13
2020R10
DOT
2019I4
2019F4
ASFS50
ASFS30
Leg 1
Leg 2
Leg 3
Leg 4
Leg 5
Sep 19
Oct 19
Nov 19
Dec 19
Jan 20
Feb 20
Mar 20
Apr 20
May 20
Jun 20
Jul 20
Aug 20
Sep 20
Oct 20
Nov 20
Dec 20
Jan 21
Feb 21
Mar 21
Apr 21

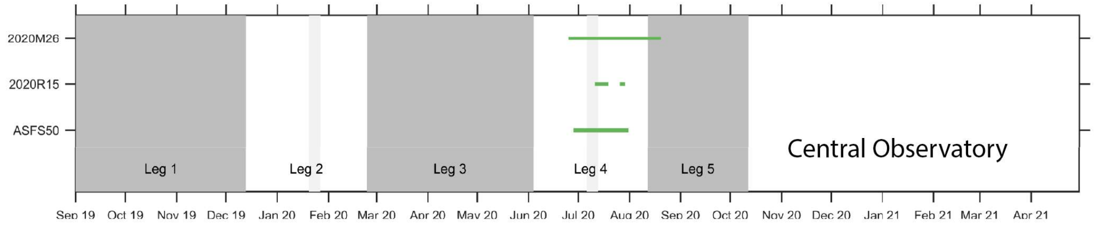
Central Observatory
2020M26
2020R15
ASFS50
Leg 1
Leg 2
Leg 3
Leg 4
Leg 5
Sep 19
Oct 19
Nov 19
Dec 19
Jan 20
Feb 20
Mar 20
Apr 20
May 20
Jun 20
Jul 20
Aug 20
Sep 20
Oct 20
Nov 20
Dec 20
Jan 21
Feb 21
Mar 21
Apr 21

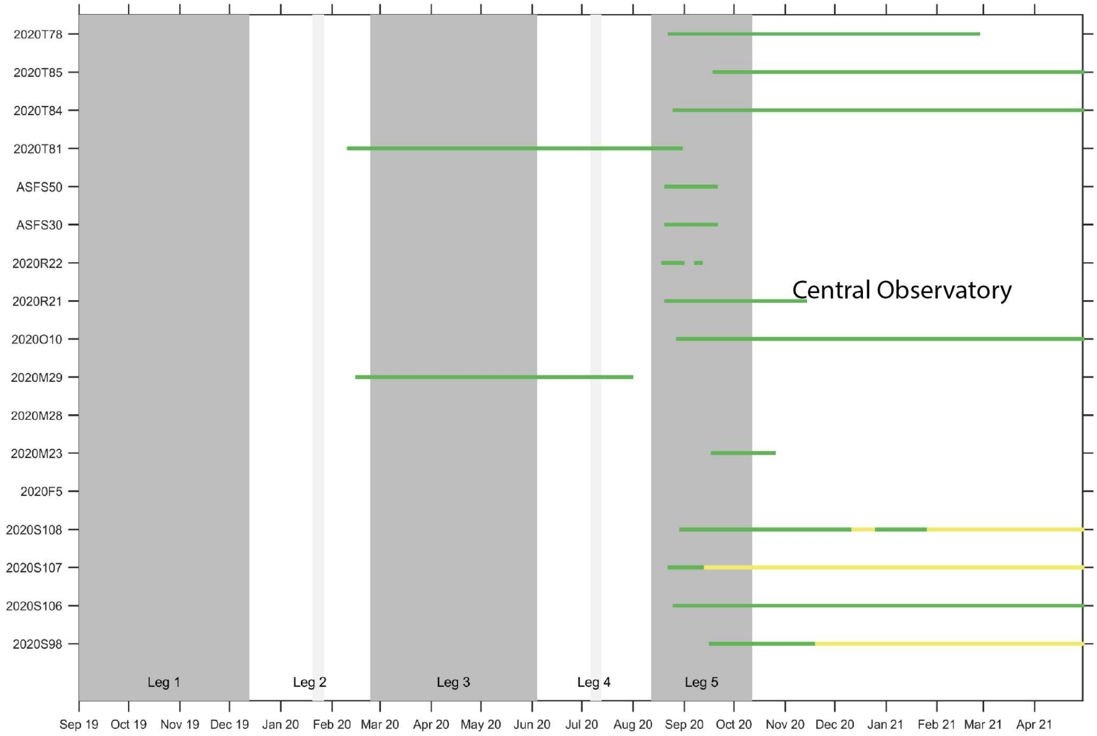
Central Observatory
2020T78
2020T85
2020T84
2020T81
ASFS50
ASFS30
2020R22
2020R21
2020O10
2020M29
2020M28
2020M23
2020F5
2020S108
2020S107
2020S106
2020S98
Leg 1
Leg 2
Leg 3
Leg 4
Leg 5
Sep 19
Oct 19
Nov 19
Dec 19
Jan 20
Feb 20
Mar 20
Apr 20
May 20
Jun 20
Jul 20
Aug 20
Sep 20
Oct 20
Nov 20
Dec 20
Jan 21
Feb 21
Mar 21
Apr 21

Figure S6: Status of observational buoys in the implementations of the Distributed Network against time.

The charts are arranged by site (L1–L3, LM and Central Observatory) and category. The status of each system is shown in color: all functioning optimally (green), partly functional (yellow) and position-only (orange). Note that the three panels for “Central Observatory” refer to the time before RV *Polarstern* left for resupply (CO1 in Table S3), after return of RV *Polarstern* until most of the DN was dismantled in Fram Strait (CO2) and the time after relocation of the Central Observatory to the central Arctic in late summer (CO3). The buoy label is given on the y-axis, the month and year in abbreviated form on the x-axis.

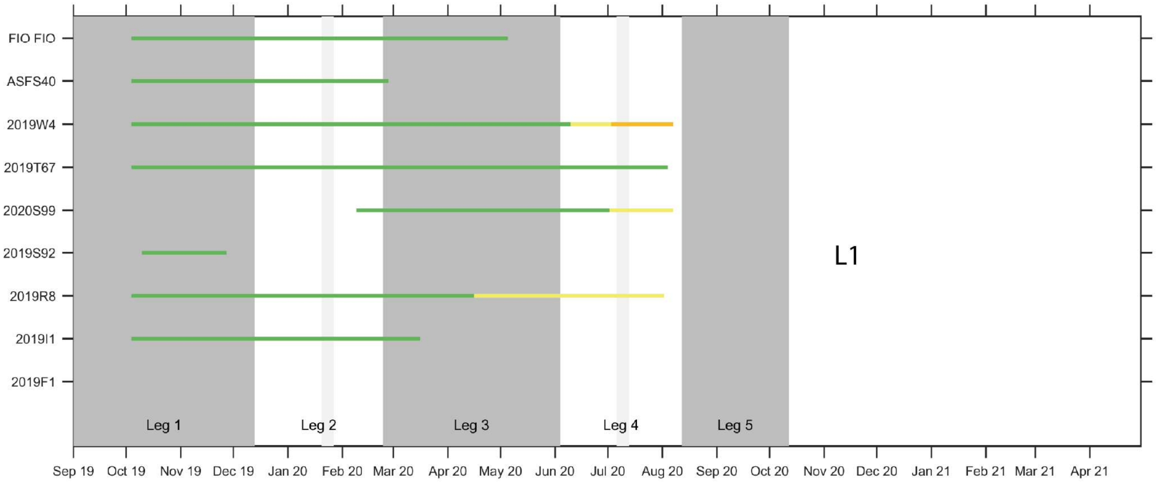

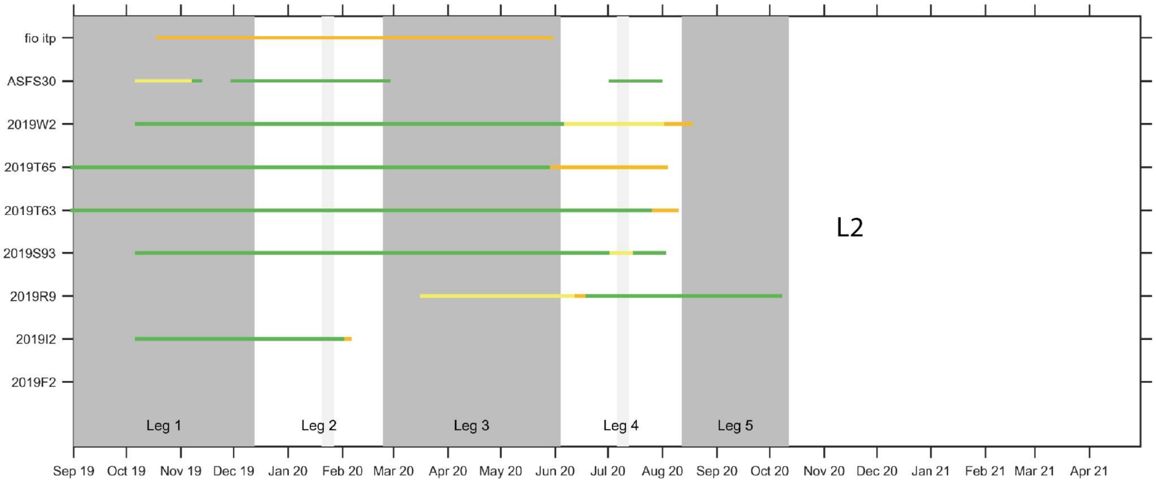

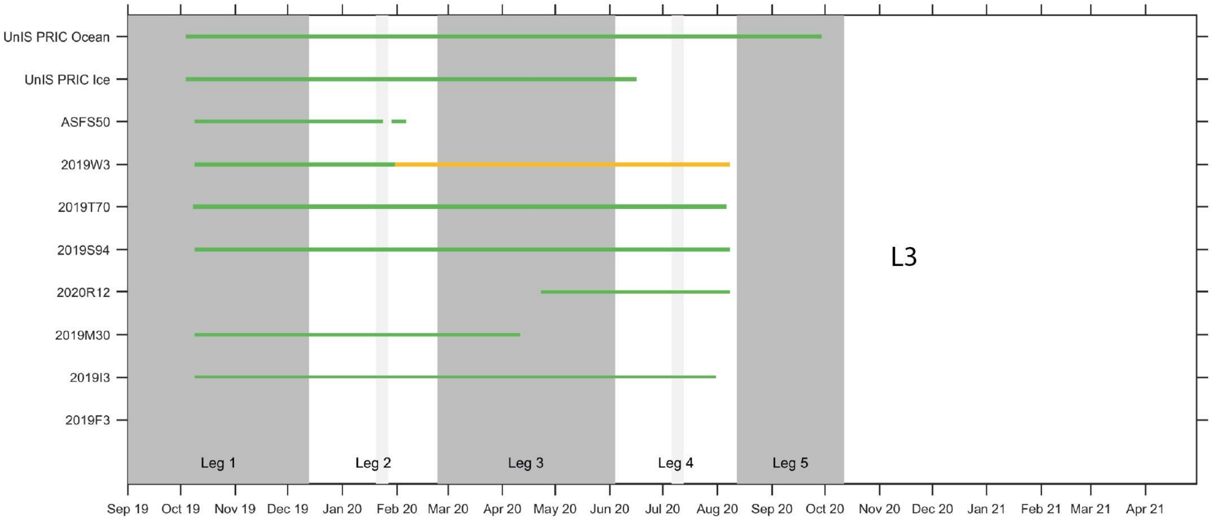

2463

2464 **Figure S5 continued.**

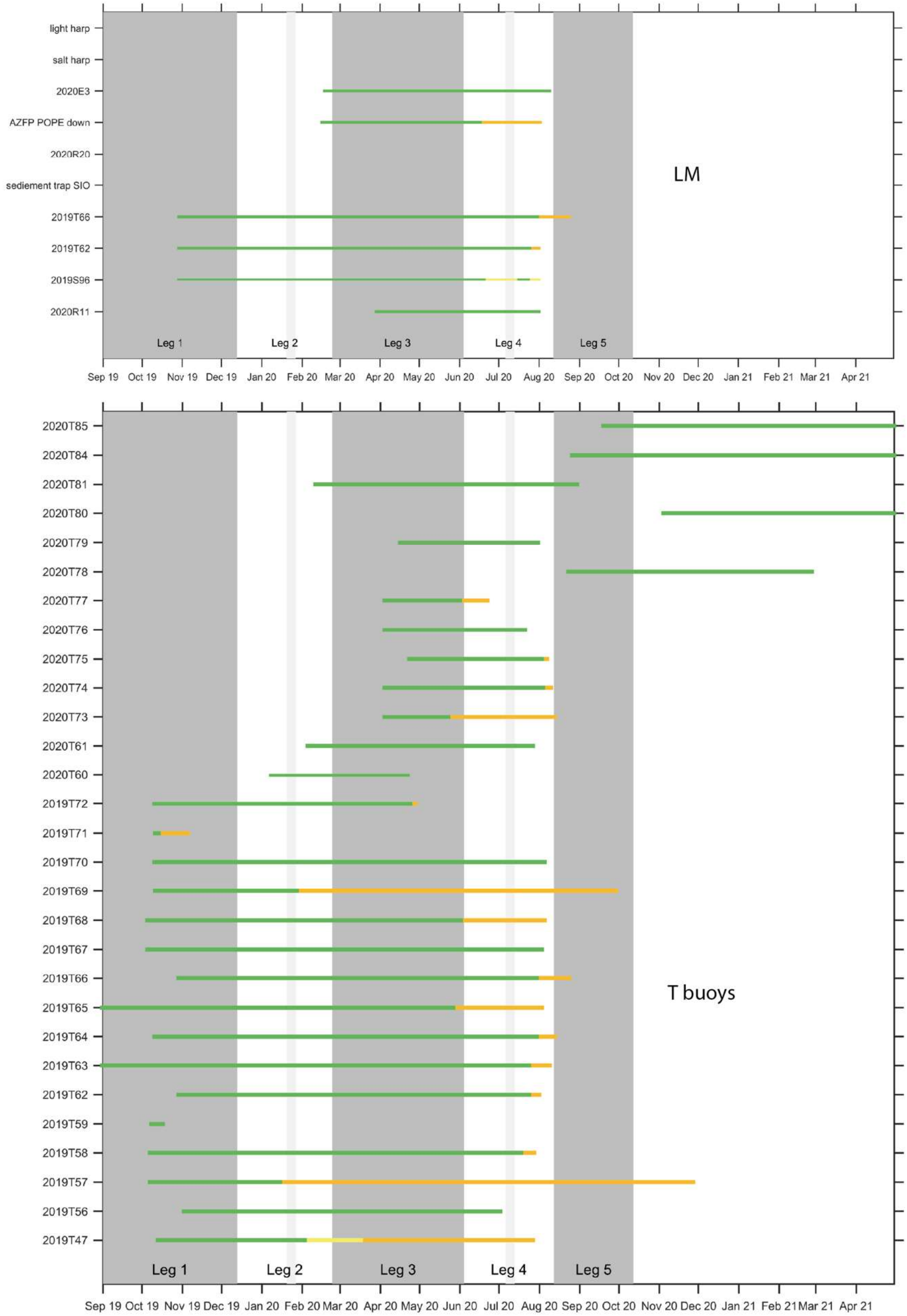

Figure S5 continued .

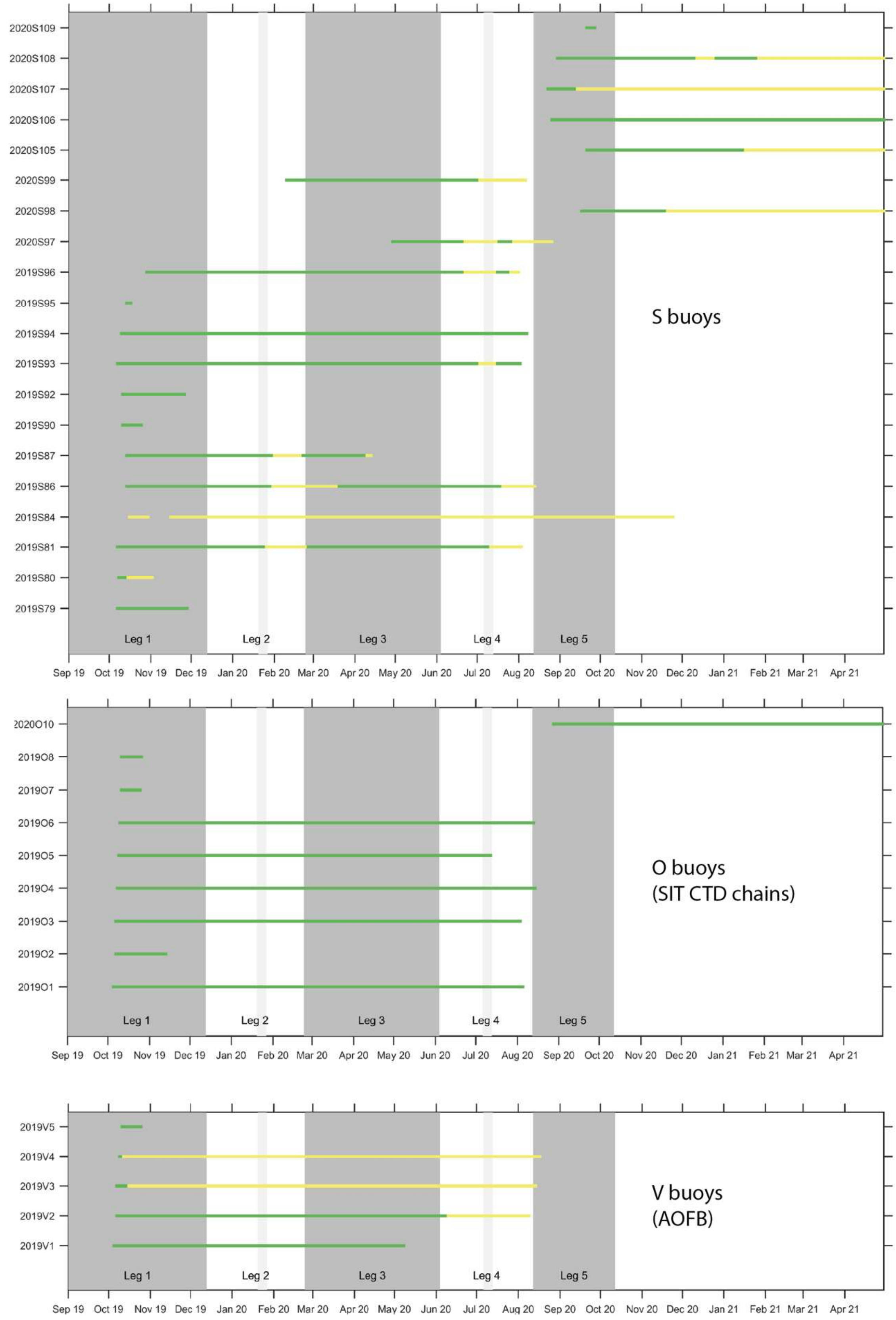

Figure S5 continued.

References

See main manuscript reference list.